

# Multi-functional cellulose microcapsules with tunable active motion and shape transitions

**Seyedeh Maryam Hosseini**

A thesis submitted in fulfilment  
of the requirements for the degree of  
Doctor of Philosophy



**UNSW**  
SYDNEY

**School of Chemical Engineering  
Faculty of Engineering  
University of New South Wales**

September 2022



## **Copyright Statement**

'I hereby grant the University of New South Wales or its agents a non-exclusive licence to archive and to make available (including to members of the public) my thesis or dissertation in whole or part in the University libraries in all forms of media, now or here after known. I acknowledge that I retain all intellectual property rights which subsist in my thesis or dissertation, such as copyright and patent rights, subject to applicable law. I also retain the right to use all or part of my thesis or dissertation in future works (such as articles or books).'

'For any substantial portions of copyright material used in this thesis, written permission for use has been obtained, or the copyright material is removed from the final public version of the thesis.'

Signed .....

Date .....

## **Authenticity Statement**

'I certify that the Library deposit digital copy is a direct equivalent of the final officially approved version of my thesis.'

Signed .....

Date .....



## **Originality Statement**

I hereby declare that this submission is my own work and to the best of my knowledge it contains no material previously published or written by another person, or substantial portions of material which have been accepted for the award of any other degree or diploma at UNSW or any other educational institute, except where due acknowledgment is made in the thesis. Any contribution made to the research by others, with whom I have worked at UNSW or elsewhere, is explicitly acknowledged in the thesis. I also declare that the intellectual content of this thesis is the product of my own work, except to the extent that assistance from others in the project's design and conception or in style, presentation and linguistic expression is acknowledged.

Signed .....

Date .....



## Abstract

Responsive and functional microcapsules have many envisioned applications, spanning uses as diverse as drug delivery, cell protection, pollution mitigation, and cosmetics. The vast majority of capsules are made from rigid cross-linked polymers or metals that are strong but inflexible, restricting their applications in some sectors. There is then a strong need to develop flexible but robust structures using sustainable materials as a basis for new multifunctional capsules. Bacterial cellulose microcapsules have been developed with a highly flexible but strong fiber mesh structure that will enable engineering of new multifunctional capsule forms. The strong but sparse capsule structures possess key length scales from nanometers to millimeters and can be used as substrate for various surface modifications while still acting as flexible enclosures for chemical cargo. This work demonstrates three new uses of the particles: First, the low-density cellulose capsules are functionalized with metal organic framework (MOF)-enzyme groups that convert them into active particle motors, propelled by reaction with dissolved hydrogen peroxide. Unlike solid micromotors, the capsules can compress in response to confinement, using their surface reaction to navigate through narrow passages without damage.

A second modification of the capsules by grafted poly-NIPAM makes the capsules temperature-responsive as well as tuning their permeability and elasticity. The highly elastic capsules can absorb and expel liquid during temperature-induced contraction and swelling, providing active uptake, release, and mixing of the liquid cargo. Finally, drying of the native bacterial cellulose microcapsules is studied to assess their ability to undergo extreme compression, store elastic energy, and mimic pollen's self-sealing capabilities. In the course of the drying process, capillary forces induce stress leading to cellulose fiber alignment and pore closure and permanent deformation of the cellulose microcapsule. However, adding a negligible amount of biodegradable polymer like carboxymethyl cellulose prevents permanent bundling of the cellulose fibers. As a result, the millimeter-scale capsule converts to a nano-scale thin disk during drying but then recovers to its initial dimension by re-hydration, experiencing 1000 times change in volume. The modified bacterial cellulose microcapsule is proposed as a new class of soft and flexible

multifunctional material capable of active motion, response, and deformation to supplement conventional microcapsules.

## Acknowledgments

To my family, Mum, Dad, Ryan, AmirReza, and Amin. Mum and Dad, you have grown me to be strong and tough me to work hard and build my future by myself. I will never forget when you both pushed me to believe in myself and go abroad alone. Thank you for believing in me and allowing me to build my own life so far from home. Thank you for your unconditional support and every night video call and text message for the past seven years ever since I left Iran to pursue my dreams; they kept me motivated and helped me to keep moving forward. Thank you for making me the person I am today, I could not ask for a better family.

To the best mentor and supervisor, Associate Professor Patrick T. Spicer who has been there for me in both my academic and personal life these past four years. Thank you so much for accepting me into your group and giving me an opportunity to be your student. Thank you for putting your trust in me. I am very fortunate to have had you as my supervisor and my academic Dad! I owe you who I am today, as a researcher and as a person. Thank you for sharing your knowledge and experience in science, critical thinking, and problem-solving. Your enthusiasm and passion for research made me enjoy each second of my Ph.D. This thesis would not have been possible without your guidance, advice, and support. Also, thank you for pushing me to learn swimming, I love swimming now! You are the most amazing person and mentor I have ever seen and I am truly grateful.

To my co-supervisor, Prof. Vicki Chen, Dr. Kang Liang, and Dr. Amir Razmjou, I thank you for your valuable advice on the projects. Thank you, Vicki, for selecting me as your Scientia Ph.D. scholar; thank you for allowing me to do my Ph.D. at UNSW, Sydney.

To the current and former members of the Complex fluid group, UNSW, Associate Professor. Stuart Prescott, Dr. Firoozeh Babayekhorasani, Dr. Isaac Gresham, Dr. Jie Song, Dr. Haiqiao Wang, Dr. Zhiwei Li, Dr. Haoda Zhou, Jonathan Mantzouridis, Arslan Siddique, Daniel Morris, and Roshanak Taheri – thank you all. Thank you, Jie, for making Jellyfish for the first time and passing your baby jellyfish to me for my Ph.D. project. Thank you Firoozeh, for teaching me Matlab and helping with my project. Isaac, thank you for your support and great help with NIPAM

Jellyfish and 3D printing projects; you are the best collaborator (you are the Jellyfish uncle for sure!). Many thanks to Adelaide Spicer for her professional schematic drawing for my 3MT competition. Thanks to Dr. Peter Judzewitsch for helping me in understanding cellulose structure.

Many thanks to the lab managers, Eh Hau Pan and Camillo Taraborrelli, for providing access to the labs and instrument training. Dr. Sandra Fok, Dr. Elvis Pandzic, Mrs. Florence Barlett, who delivered imaging suggestions and helped in BMIE, Dr. Yin Yao from EMU, who taught me how to use Pt/Cr coater and SEM, and to all the other chemical engineering staff at UNSW who helped and supported my work and campus life. Thanks to Amy Gullins and Dr. Isaac Gresham for proofreading a literature review chapter of my thesis. Many thanks to Dr. Ziyi Guo for contributing to my first project.

To my lovely friends at Wichlab - Rakib, Shazia, Vinod, Luca, Jonas, Amy, and baby Fatima. Thank you for all the cookie breaks, camping trips, sleepover nights, Friday dinners, birthday parties, and fun we had together. Thank you for each and every moment. Having you guys made my Ph.D. journey the sweetest and most memorable time of my life. Thank you for having me as your plus-one at Wichlab gatherings. I love you guys so much, I am so blessed to have met you and have you in my life. Thank you, Dr. Peter Wich, for giving me the honour of being a plus one of your group.

Many thanks to my family and friends Siavash, Desi, Elham, Tammie, Widiha, Asefe, Ecem, Aline, Munirah, Yazid, Milton, Ning, and Rad for their support.

Last but not least, special thanks to my lovely Ryan for his unlimited and unconditional support, for teaching me how to step out of my comfort zone and be brave. I am so lucky you have been in my life since the day I was born.

This PhD was made possible by a Scientia Ph.D. scholarship awarded by UNSW.

## List of Publications

### Publications included in this thesis

Propulsion, deformation, and confinement response of hollow nanocellulose millimotors. **Maryam Hosseini**, *Firoozeh Babayekhorasani, Ziyi Guo, Kang Liang, Vicki Chen, Patrick T. Spicer, Journal of Colloid and Interface Science, Volume 628, Part B, 2022, Pages 435-445, ISSN 0021-9797. DOI:https://doi.org/10.1016/j.jcis.2022.08.035.*

### Contributions:

MH performed the experiment, characterization, and data analysis and was the primary writer of the paper. FB performed the microscopy and data analysis, ZG performed XRD characterization. PS, VC, and KL guided the project and assisted in assembling the manuscript. All authors assisted in proofreading the final paper.

### Additional Publications

The following papers are the results of collaboration work during the PhD candidature but are not included in this thesis:

- Molecular and Colloidal Transport in Bacterial Cellulose Hydrogels. *Firoozeh Babayekhorasani, Maryam Hosseini, and Patrick T. Spicer, Biomacromolecules. 2022 May 11*
- Development of excipients free inhalable co spray dried tobramycin and diclofenac formulations for cystic fibrosis using two and three fluid nozzles. *Nirmal Marasini, Zara Sheikh, Chun YJ Wong, Maryam Hosseini, Patrick T. Spicer, Paul Young, Hui Xin Ong, and Daniela Traini, International Journal of Pharmaceutics. 2022 Aug 25;624:121989*
- Dynamic X-ray micotomography of microfibrous cellulose liquid foams using deep learning. *Syeda Rubaiya Muin, Patrick T. Spicer, Kunning Tang, Yufu Niu, Maryam Hosseini, Peyman Mostaghimi, and Ryan T. Armstrong, Chemical Engineering Science. 2022 Feb 2;248:117173*



# Contents

<b>Abstract</b>	<b>i</b>
<b>List of Publications</b>	<b>v</b>
<b>1 Introduction</b>	<b>1</b>
1.1 Material selection . . . . .	2
1.2 Microcapsule preparation methods . . . . .	8
1.2.1 Chemical method of microcapsule production . . . . .	8
1.2.2 Spray drying . . . . .	10
1.2.3 Microfluidics . . . . .	12
1.2.4 Biologically prepared microcapsule . . . . .	13
1.3 Microcapsule characterization . . . . .	15
1.3.1 Capsule permeability . . . . .	15
1.3.2 Microcapsule flexibility and deformation . . . . .	21
1.4 Functional and stimuli responsive microcapsule . . . . .	27
1.4.1 Release profile . . . . .	32
1.4.2 Responsive deformation . . . . .	34
1.5 Project aims and overview . . . . .	36
References . . . . .	39
<b>2 Propulsion, deformation, and confinement response of hollow nanocellulose millimotors</b>	<b>49</b>
2.1 Introduction . . . . .	49
2.2 Methods and Materials . . . . .	51
2.2.1 Sample imaging and analysis . . . . .	53
2.3 Results and discussion . . . . .	54
2.3.1 Capsule characterization . . . . .	54
2.3.2 Porosity of motors . . . . .	60
2.3.3 Millimotor capsule propulsion . . . . .	64
2.3.4 Motor deformation and confinement response . . . . .	68
2.4 Conclusions . . . . .	73

References . . . . .	74
<b>3 Multi-functional responsive nanocellulose-PNIPAM capsules</b>	<b>79</b>
3.1 Introduction . . . . .	79
3.2 Materials and methods . . . . .	82
3.2.1 Sample imaging and analysis . . . . .	85
3.3 Results and discussion . . . . .	87
3.3.1 Capsule characterization . . . . .	87
3.3.2 Permeability . . . . .	92
3.3.3 Deformation and shape memory . . . . .	94
3.3.4 Changes in capsule volume with temperature . . . . .	98
3.3.5 Particle tracking during multiple cycles of temperature change .	100
3.4 Conclusions . . . . .	101
References . . . . .	102
<b>4 Drying cellulose microcapsules for the fabrication of particles with tunable structures</b>	<b>107</b>
4.1 Introduction . . . . .	107
4.2 Methods and Materials . . . . .	109
4.2.1 Sample imaging and analysis . . . . .	110
4.3 Results and discussion . . . . .	110
4.4 Conclusions . . . . .	122
References . . . . .	123
<b>5 Conclusions and future work</b>	<b>127</b>
<b>A Appendix</b>	<b>131</b>
A.1 Supplementary information for chapter 2 . . . . .	131
References . . . . .	135

## List of Abbreviations

AFM	atomic force microscopy
BIBB	$\alpha$ -bromoisobutyryl bromide
CAT	catalase
CLSM	confocal laser scanning microscopy
CMC	carboxymethyl cellulose
DMSO	dimethyl sulphoxide
DNA	deoxyribonucleic acid
EDA	ethylenediamine
FRAP	fluorescence recovery after photobleaching
FTIR	fourier transform infrared
HCO	hydrogenated Castor Oil
HMTETA	1,1,4,7,10,10-hexamethyltriethylenetetramine
LBL	layer by layer
LCST	lower critical solution temperature
LSFM	light sheet fluorescence microscopy
MOF	metal–organic framework
MSD	mean squared displacement
NA	numerical aperture
PA	Polyamide
PF	pore flow
PMMA	(poly(methyl methacrylate))
PNIPAM	poly-N-isopropylacrylamide

RhB	rhodamine B isothiocyanate
SD	solution diffusion
SEM	scanning electron microscope
TDC	terephthaloyl dichloride
TEA	triethylamine
THF	tetrahydrofuran
XRD	X-ray Powder Diffraction
ZIF90	zinc imidazolate-2-carboxyaldehyde
ZIFL	zinc 2-methylimidazole

# Chapter 1

## Introduction

Microcapsules are microscale particles with the ability to contain and protect a payload, for instance, a pH sensitive oral drug. However, for a capsule to be effective it must not only protect its payload, but must also deploy it at the right time and location. Responsive microcapsules that can be triggered by specific stimuli to release their payload have the potential to enhance the efficacy of active ingredients in areas such as drug delivery, agriculture, cosmetics, detergent, and food additives<sup>1-3</sup>. The synthesis of microcapsules was introduced by Green, and Schleicher<sup>4</sup>, who encapsulated dyes by coacervation of gelatin and gum Arabic. Since then, diverse methods of synthesizing microcapsules have been developed for containment, protection, and controlled release of a diverse range of active materials<sup>1,5</sup>.

The development of microcapsules has often been inspired by natural systems, such as biological cells or pollen. Biological cells can deform and recover when they encounter confinement and have a high level of control over their motion and response to their external environment. This requires some level of softness (low elastic modulus) as well as a shape-memory. In addition, biological cells and organisms can use their deformation to move or secrete bioactive compounds<sup>6</sup>, providing complex and responsive motion, encapsulation, and delivery functions. Pollen grains are naturally responsive microcapsules that can encapsulate over 700 particles<sup>7</sup>, including proteins, lipids, starch, and cellulose components ranging in size from several nanometers to 3  $\mu\text{m}$ . Pollen grains can fold and shrink during

dehydration to protect plant DNA. Upon exposure to humidity and contact with targeted plant organs, they can swell and regain their hydrated state<sup>8-12</sup>, Figure 1.1 (f and g).

Red blood cells (RBCs) are another example of responsive biological cells that demonstrate an extraordinary ability to undergo reversible large deformation and exhibit fluidity. Figures 1.1 (a-e) show images of RBCs being squeezed through a microfluidics channel, deforming and recovering in a reversible manner. The ability of RBCs to undergo reversible deformation is a vital factor for human health, as their geometry and deformability are tested when passing through interendothelial slits in the human spleen<sup>13,14</sup>. The highly efficient encapsulation and response of biological cells (e.g., red blood cells) inspire researchers to design functional and responsive microcapsules that mimic the performance of their biological analogues (Figure 1.1).

Ideal capsules should have a well-defined membrane boundary to separate internal and external compartment volumes and tunable permeability, enabling an exchange of material and molecules with surrounding media<sup>15</sup>. Despite significant progress in synthesizing responsive microcapsules, developing a complex microcapsule similar to pollen or a cell is yet to be achieved. In this chapter, we review common microcapsule preparation methods as well as the performance of the resulting microcapsules to identify current shortfalls in microcapsule synthesis and performance.

### **1.1 Material selection**

Microcapsule properties are primarily determined by two factors: the material and the preparation method. Microcapsules can be synthesized from various materials including metals, polymers, or composites. Capsules can also be produced

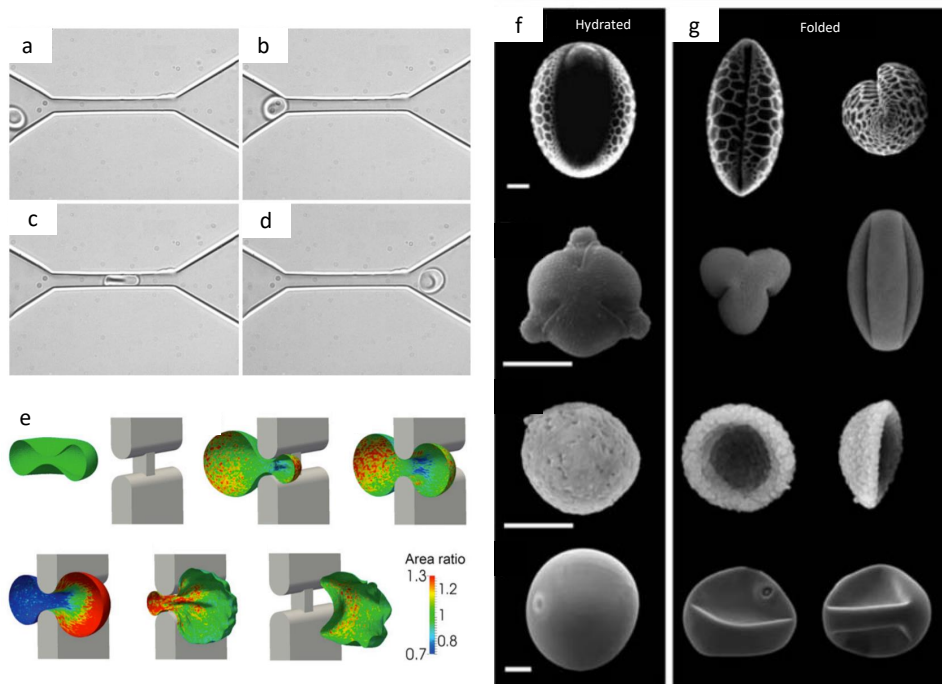


**Figure 1.1:** Natural capsules: red blood cell can squeeze and move through capillary with diameter of 10% of its diameter (a-e)<sup>13,14</sup> (copyright (2007) National Academy of Sciences and copyright (2016) National Academy of Sciences), pollen grain can fold in response to changing in humidity (f and g)<sup>10</sup> (copyright (2010) National Academy of Sciences.)

with different structures such as crystalline, amorphous, and fibrous. The material choice determines microcapsules' physical, chemical, and mechanical properties. For instance, microcapsules with metal shell structures can be used for making rigid capsules with high thermal and mechanical stability suitable for making self-lubricating polymers<sup>16</sup>, and self-healing composites<sup>17</sup>, anticorrosion coatings, smart concretes, and thermal energy storage systems<sup>18</sup>, Figure 1.2.

In Figure 1.2, we plot the elastic modulus and density of a number of microcapsules that have been reported in the literature. The resulting plot classifies the capsules based on their applications, indicating that the elasticity and density of the microcapsule determine its potential use. For instance, the bacterial cellulose microcapsule, which has an extremely low density and relatively low elasticity, has potential for drug delivery and cell encapsulation where high payload is needed and the encapsulated contents are sensitive<sup>19</sup>

Polymers are the most common materials used for microcapsule shell structures due to their diversity and functionality, which allow for the addition of responsiveness to the microcapsule and the tuning of its density and mechanical properties, ranging from a glassy and rigid shell to a soft and flexible one. The diversity in mechanical properties of polymer-based microcapsules offers a wide range of applications, from cell encapsulation, textile coating, and drug delivery to biosensors that require low elasticity and rapid deformation, to anti-corrosion coating in self-healing cement or heat storage, which need a more rigid capsule with a higher elastic modulus<sup>17,20–40</sup>.

Polymer-based microcapsules have semipermeable and permeable shells depending on the preparation method used<sup>41</sup>. Hydrophobic, hydrophilic, or a mixture of both materials can be used to make a microcapsule; however, they should meet the desired shell properties, including flexibility, permeability, stability, and

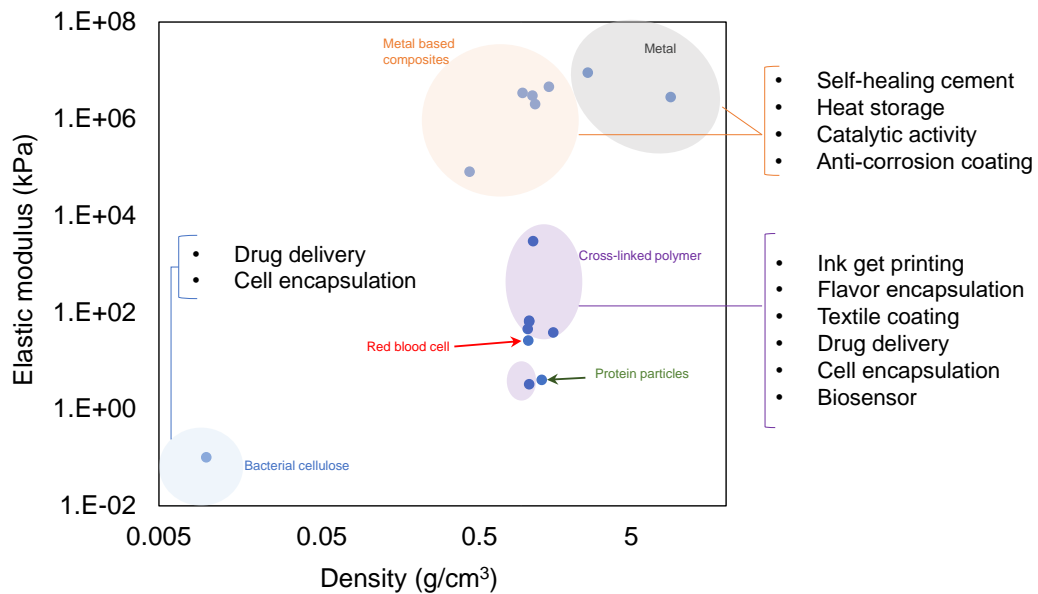


**Figure 1.2:** Microcapsules' density, elastic modulus, and their applications<sup>17,19-40</sup>

strength<sup>1</sup>. Shell strength is critical in determining shell reusability, as brittle and rigid shell materials might create cracks during long-term usage.

Recently Li et al.<sup>16</sup> developed a double-wall silica microcapsule with a diameter and shell thickness of 90 and 6  $\mu\text{m}$ , respectively. They reported high thermal stability of the microcapsules with a thermal degradation onset temperature of 300 °C. Metal-based microcapsules have impermeable or porous shell structures and can only rupture or deform under extreme stress, depending on their elastic modulus. They can also be used in high-temperature environments, whereas polymer-based microcapsules are brittle, easily broken, and can decompose under temperature ranges from 200 °C<sup>16</sup>.

Microcapsules with porous shells have drawn attention recently due to their high encapsulation capacity, surface area, and release rate. The microcapsules' porosity is essential in determining the release kinetics and capacity efficiency. The structure, diameter, and number of pores are critical factors in determining the

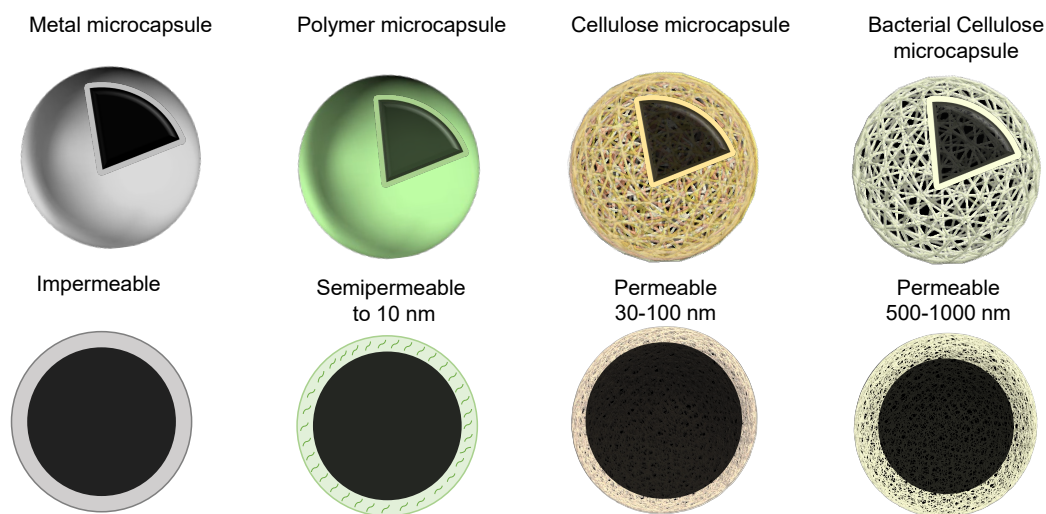


**Figure 1.3:** Microcapsules' shell structure

capsule porosity<sup>42</sup>. Microcapsule's shell structure is classified in four categories, in Figure 1.3 based on the material and shell permeability. Most polymers and metals used to make a rigid capsule can produce a capsule with a porous structure, including polylactic acid, chitosan, silica, and calcium carbonate<sup>42,43</sup>. They can be produced using different methods, such as solvent evaporation, polymerization, phase separation, and spray drying. Compared to the semipermeable or impermeable microcapsules produced from the same material, porous microcapsules have a lower density, higher surface area, and higher absorption capacity<sup>42</sup>. Some challenges limit their application in different sectors, such as preparation method and fixed pore size<sup>42</sup>. However, Ye et al.<sup>44</sup> developed the cellulose cage-like capsule with a porous shell, low density, and high surface area. They incorporated the cellulose nanocrystal with a polymer to achieve responsive porous microcapsules, in which the pore size changes in response to pH. Paulraj et al. also expanded the responsiveness of cellulose cage-like capsules to include permeability responses triggered by more specific molecules such as salt and glucose<sup>45,46</sup>.

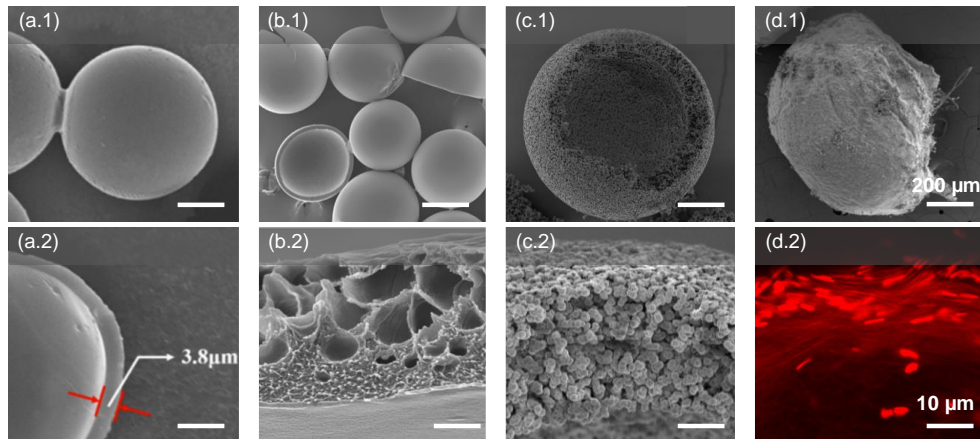


**Figure 1.4:** (a.1 and a.2) SEM image of polyurethane(PU) microcapsules with a rigid and nonporous shell structure<sup>47</sup>, Reproduced with permission Copyright 2019, Elsevier; (b.1 and b.2) PMMA microcapsules with macroporous shell, Adapted with permission from<sup>48</sup>. Copyright 2021 American Chemical Society, (c.1 and c.2) The porous shell is made from a network of interconnected polymer particles, Adapted with permission from<sup>49</sup>. Copyright 2017 American Chemical Society, and (d.1 and d.2) bacteria synthesized microcapsules with a fibrous shell structure<sup>19</sup>.

Figure 1.4 shows more example capsules with nonporous and porous shells. Ma et al.<sup>47</sup> synthesized the nonporous and smooth polyurethane microcapsules with a smooth shell structure, developing a microcapsule to generate self-lubricating polymer composites. Wu et al.<sup>48</sup> developed poly(methyl methacrylate) microcapsules featuring an asymmetric graded macroporous shell (pore size < 70 nm) to achieve highly selective permeation and fast uptake and release essential for dispersed microreactors, carriers, and sensors. A microcapsule with a more porous shell structure (pore size 100 nm) was synthesized by Loiseau et al.<sup>49</sup> for on-demand release of small molecules triggered by pH change. Figure 1.4 (d) shows the bacterial cellulose microcapsule with fibrous shell structure and the pore size of 500 nm<sup>19</sup>.

## 1.2 Microcapsule preparation methods

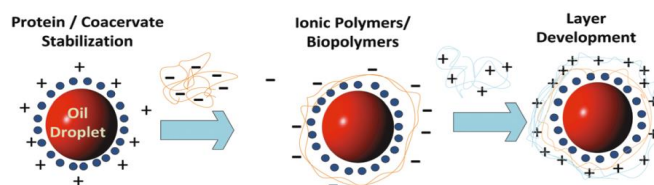
Microcapsule preparation methods determine the capsule's size, shell thickness, permeability, and flexibility<sup>1,50</sup>, which usually involves a chemical, physical, mechanical, or biological process. Here we review some of the most common methods of microcapsule preparation.

### 1.2.1 Chemical method of microcapsule production

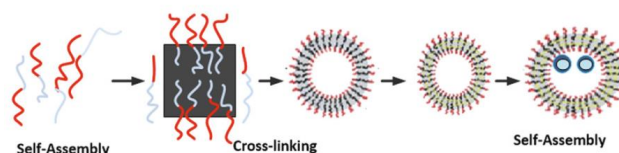
Microcapsules are typically produced by layer-by-layer assembly, polymer self assembly, *in situ* polymerization, and interfacial polymerization. Recently using microfluidics devices enabled the production of multi-emulsion droplets, which is now used as a template to design microcapsules. Also, the loading of microcapsules during droplet formation enhances encapsulation efficiency. Combining microfluidics techniques and conventional chemical methods of synthesizing microcapsules enhances microcapsule production efficiency.

Among different methods of synthesizing microcapsules, layer by layer (LBL) assembly is one of the simplest methods of shell and thin-film production. A polymeric component or polyelectrolyte is deposited onto the surface of colloidal particles and, when the internal droplet dissolves, a microcapsule is formed (Figure 1.5 (a)). This method builds a layer of polyelectrolytes onto colloidal droplets using electrostatic interactions. The charged particles or droplets are placed into an electrolyte with the opposite charge; therefore, the electrostatic force drives the polymer to coat the particles. In order to make a hollow microcapsule, the internal charged particle (core) needs to be dissolved. Although dissolving the internal core can be a complex procedure for some applications the LBL method is useful for controlling shell permeability, elasticity, and mechanical stability<sup>1,51</sup>.

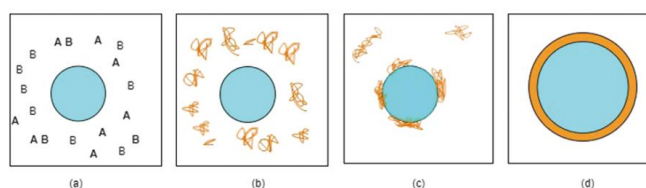
## (a) Layer-by-layer assembly



## (b) Self assembly



## (c) In situ polymerization



## (d) Interfacial polymerization methods

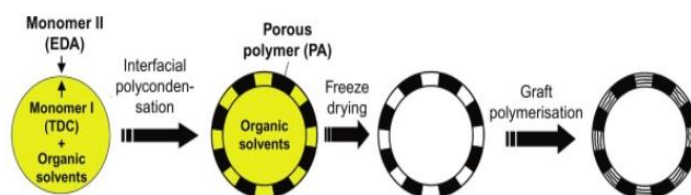


**Figure 1.5:** Different chemical methods of microcapsule production; (a) Layer-by-layer deposition method<sup>1,51</sup> Reproduced with permission.<sup>1</sup> Copyright 2020, The Royal Society of Chemistry, (b) Self-assembly method<sup>52</sup> Reproduced with permission.<sup>52</sup> Copyright 2013, The Royal Society of Chemistry, (c) Deposition and precipitation of the polymer at the interface<sup>53</sup> Reproduced with permission<sup>53</sup> Copyright 2018, Taylor and Francis, and (d) In situ polymerization<sup>54,55</sup>. Reproduced with permission.<sup>54</sup> Copyright 2019, Elsevier.

Self-assembly is the other common way of microcapsule production, especially for pharmaceutical and agricultural industries. Self-assembly is a force balance method when a different structure can generate spontaneously without the need of an external driving force, Figure 1.5 (b). The structure can be made of molecules or microparticles, which can rearrange to make a capsule structure using different interactions such as electrostatic interactions, hydrogen bonds,  $\pi$ - $\pi$  interaction, and van der Waals forces<sup>1,52</sup>.

*In situ* polymerization or interfacial polymerization is a chemical method of microcapsule production. In this method, a monomer is provided inside or outside the shell, and the shell is formed via polymerization. Microcapsules with an ammonium polyphosphate core and glycidyl methacrylate shell are one examples of *in situ* polymerization, Figure 1.5 (c and d). Generally, polymer deposition and precipitation occur at the core (droplet) interface due to changing pH or temperature. A wide range of polymers like formaldehyde constitution, melamine, or urea can be utilised however, cracks in the shell may develop overtime<sup>1,53</sup>.

### 1.2.2 Spray drying

Spray drying is a large-scale, rapid, low-cost, and reproducible method of production of spherical particles and microcapsules in food, pharmaceuticals, and detergents industries using a rapid drying of aerosols<sup>56-58</sup>. Spray drying is a phase transition process in which the fluid stream is sprayed and dried when exposed to high-pressure gas. The particles' shape, structure, size, and porosity can be tuned by changing the operational conditions<sup>56</sup>.

By tuning the solvent evaporation rate, surface charge, and chemical properties of the droplet, particles with different morphology can be achieved<sup>57</sup>. Synthesizing the particles with a spherical shape is the most common approach, however, by

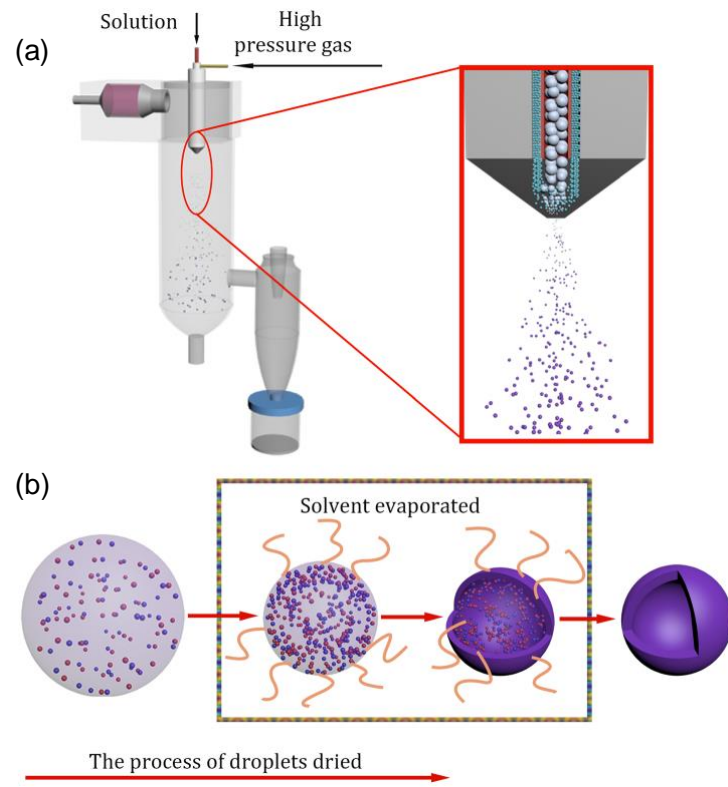


**Figure 1.6:** Schematic of the spray drying system. (a) The particle formation process. (b) The drying and solvent evaporation process<sup>59</sup>

adjusting heat and mass transfer from the surface to the deepest point inside a hollow droplet capsule can be synthesized<sup>56</sup>. Figure 1.6 shows the spray drying process, where the solution and high-pressure gas interact, which leads to the solution crashing into lots of small fog drops in the drying chamber. The tiny fog drops are dried into micro-scale particles. This technique can make particles with high homogeneity on a large scale<sup>59</sup>. Despite several advantages, such as large-scale production of microcapsules and particles, spray drying operation temperature, synthesizing microcapsules with uniform porous shell structure, and nozzle clogging during formation of large particles all limit the usage of this method<sup>60</sup>.

### 1.2.3 Microfluidics

As microcapsules are emerging as a functional material for a wide range of applications, developing efficient microcapsule production with tuneable size and structure on a large scale is needed<sup>61</sup>. All reported conventional methods of microcapsule production make the capsule with large polydispersity, poor reproducibility, and limited tunable morphology. In order to overcome these limitations, different methods have been developed, such as droplet microfluidics, photolithography, and micro-molding; however, droplet microfluidics is known as the most effective way of synthesizing microcapsules<sup>61</sup>. It allows precise tuning of the composite and well-defined shell structure of a capsule with diverse size, which is suitable for specific functions, especially in biomedical applications<sup>61</sup>. This method is based on the emulsion of a mixture of two immiscible liquids, where one of them is dispersed in another. Typically they require applied stress generated by agitation<sup>61-63</sup>. microfluidics device offers various ways of making the emulsions by fabrication one drop at a time. Precise microcapsules can be produced by force balancing flow during the droplet breakup, which can be applied to diverse channel geometries such

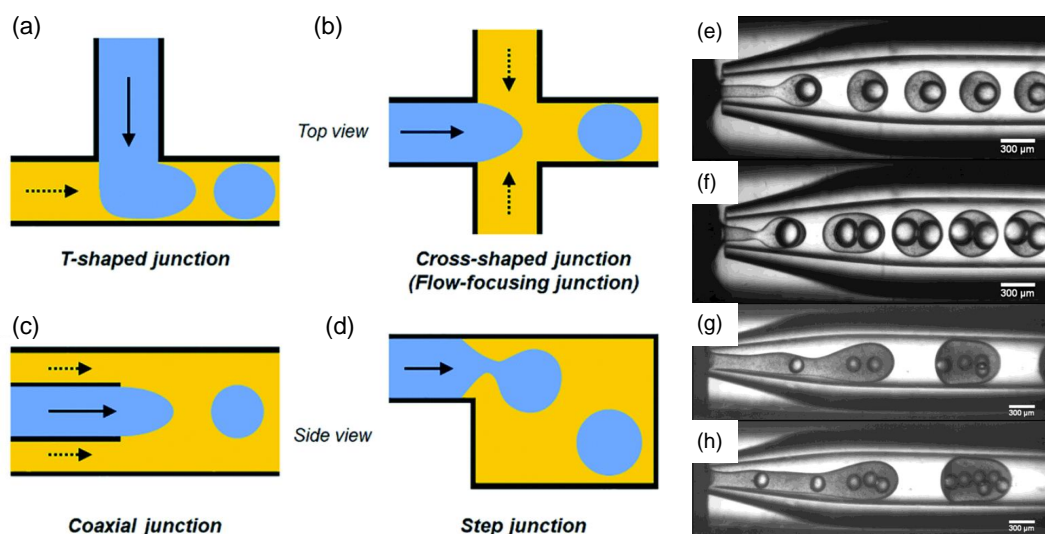


**Figure 1.7:** Four types of drop making microfluidic systems: (a) T-shaped, (b) cross-shaped, (c) coaxial, and (d) step geometries<sup>64</sup>. Reproduced with permission.<sup>64</sup> Copyright 2022, The Royal Society of Chemistry. (e-h) Generation of emulsions at different fluid flow rates<sup>65</sup>. Reprinted with permission from<sup>65</sup>. Copyright 2018 American Chemical Society.

as T-shaped, cross-shaped (flow-focusing), coaxial, and step junctions, as shown in Figure 1.7. When two or more interfaces are simultaneously broken, multiple-emulsion drops can be produced in one step. In a T-shaped junction, the emulsion drops are synthesized using the viscous shear force exerted on the dispersed phase by the continuous phase<sup>61,64</sup>.

#### 1.2.4 Biologically prepared microcapsule

Most research on developing microcapsules use chemical and physical methods, which restricts achieving the complex structure of natural capsules. Hence, reusing and modifying existing microcapsules has gained more attention and, by employing biological microcapsules, advanced drug delivery and controlled release systems can be created<sup>66–71</sup>. For instance, Prabhakar et al.<sup>72</sup> used pollen for encapsulating protein and, by using organic dyes and the vacuum and passive loading method, their research indicated the pollen's unique structure for cargo delivery applica-

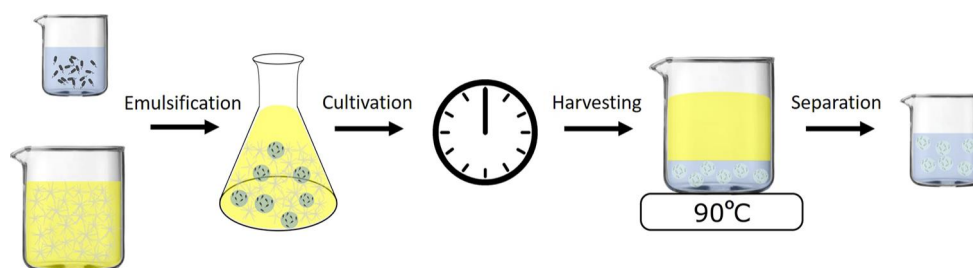


**Figure 1.8:** Schematic of bacterial cellulose microcapsule production; where encapsulated bacteria in gelled oil synthesis the cellulose microcapsule<sup>19</sup>. Reprinted with permission from<sup>19</sup>. Copyright 2019 American Chemical Society.

tions. However, reusing the biological sample requires multiple steps of cleaning and processing the microcapsule structure before modifying and loading the desired cargo<sup>70</sup>.

Recent advances in using biological cells, e.g., bacteria or microorganisms, for making complex 3D structures has motivated<sup>73</sup> recent work done by Song et al.<sup>19</sup> to engineer bacterial motion and make a microcapsule. The biointerfacial process is a new method of producing cellulose microcapsules using templated growth of *Acetobacter xylinum* onto emulsion droplets in gelled oil (the mixture of HCO and vegetable oil)<sup>19</sup>. Figure 1.8 shows the schematic of bacterial cellulose production. Bacteria polymerize glucose molecules to produce micron-length cellulose fibers, which entangle and form a core-shell structure at the water-oil interface within two weeks. This method can be used to synthesize microcapsules with a size range from 50  $\mu\text{m}$  to several millimeters. The capsule's microfiber structure creates a mesh-like shell with an average pore size of 500 nm, making a millimeter or micron size capsule with extremely low weight (200 ng) and high water-holding capacity in the hollow core and mesh structured shell due to cellulose hydroxyl groups. The bacterial cellulose's unique structure can be used to mimic pollen self-sealing during

dehydration, however, dehydration can permanently deform the cellulose microcapsule due to cellulose fiber interactions.

Microcapsules can be synthesized by various methods to create a complex and specific shell structure which aids in addressing various challenges encountered during the encapsulation process and controlled release systems. Therefore, selecting the right preparation process is as important as material selection, as it can lead to developing a capsule with a suitable structure. Creating a biocompatible microcapsule for biomedical and food applications is required, which further draws attention to using a biological method of polymerization such as using bacteria to polymerize glucose molecules and produce cellulose fibers<sup>19,74</sup>.

## **1.3 Microcapsule characterization**

As microcapsule applications increase in different sectors, understanding and evaluating their structure is needed. Here we investigate the general properties of microcapsules, the permeability and flexibility of microcapsules determines the microcapsule's performance in terms of encapsulation and controlled release. Additionally, different applications require unique properties; for example, self-healing cement applications, a rigid capsule with high stability and less permeability is desirable and, in the cell protection field, a permeable and flexible capsule is preferable.

### **1.3.1 Capsule permeability**

The permeability is one of the most critical factors used to determine efficiency for different applications. For instance, sectors like drug delivery require the capsule to release its content in order to adjust the permeability in response to change in pH or temperature and for cosmetics and fragrance applications, a fast release is

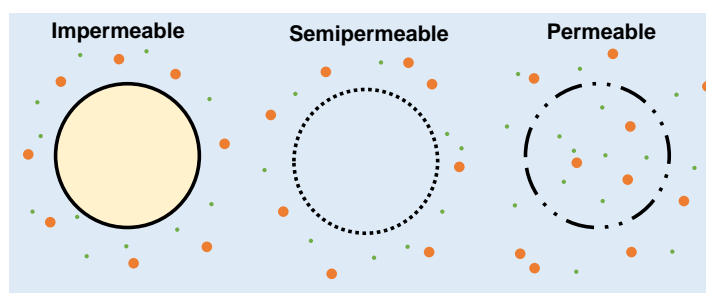


**Figure 1.9:** Different types of microcapsule permeability.

preferable, while for cell protection specific permeability is required to protect the cell and provide all nutrients required for cell survival. Therefore, understanding the factors affecting permeability is essential. Generally, shell thickness, porosity, surface chemistry, and pore structure affect the microcapsule permeability<sup>75</sup>.

Figure 1.9 illustrates that the microcapsules are classified into three categories: permeable (depending on the pore size, let solvent, solute, ions, and particles penetrate across the shell), semipermeable (only solvent can pass through the capsule), and impermeable (no substance can pass) capsule. Depending on the application different types of permeability are desirable.

Depending on the shell structure, transport of encapsulated ingredients across the microcapsule shell follows the same mechanism as a conventional membrane. Therefore, similar to the membrane, transport across the shell can be classified into two categories based on the shell structure. If the capsule has a porous shell with a fixed pore size the passage of certain species (smaller than the pore size) is permitted, and mass transfer occurs due to a pressure gradient. In the case of a nonporous polymer-based shell structures, the capsule permeability and selectivity are determined by the diffusivity and solubility of encapsulated ingredients within the shell, as seen in Figure 1.10.

Transport through the porous shell is described using the pore-flow model (PF), in which the pressure gradient drives the fluid through pores across the shell, visible

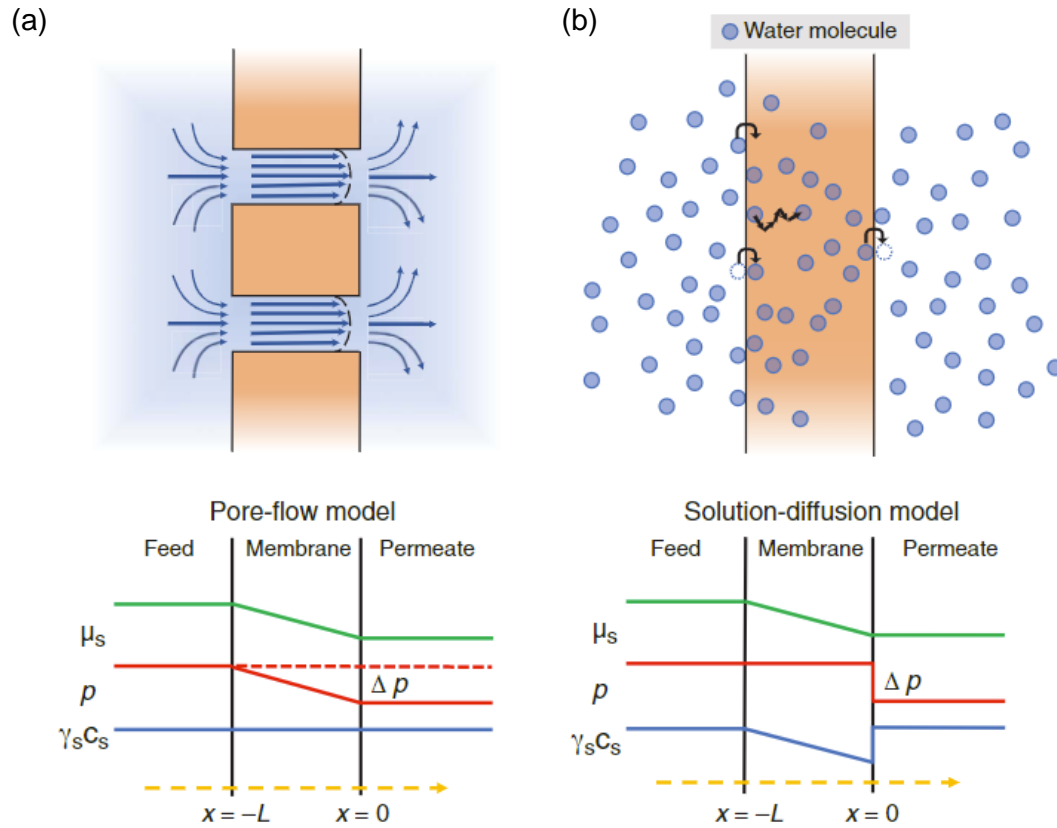


**Figure 1.10:** (a) Schematic illustration of particles and molecular transportation through porous shell or membrane (pore-flow membrane) and (b) Molecular diffusion across non-porous structure (solution-diffusion membrane)<sup>76</sup>. (Copyright (2022) National Academy of Sciences.)

in Figure 1.10. Solving the Navier-Stokes equations can relate the solvent flux to the pressure gradient however, if the pore size and structure are known, then a Darcy-flow can be used to relate the velocity of the solvent based on the pressure gradient<sup>76</sup>:

$$J_s = \frac{\phi_s \Delta P}{\xi L} \equiv \kappa_{PF} \frac{\Delta P}{L} \quad (1.1)$$

Where  $J_s$  ( $\text{m}^3/\text{s}$ ),  $\Delta P$  (Pa),  $\phi_s$  (mol),  $\xi$ ,  $\kappa_{PF}$  ( $\text{m}^2$ ), and  $L$  (m) are solvent flux, a local pressure gradient, a volume fraction within the membrane, a local solvent friction coefficient permeability, and a membrane or shell thickness<sup>76</sup>.

Microcapsule permeability is the passive diffusion rate of permeated solvent, molecules, or particles across the nonporous shell or membrane. The solution-diffusion model (SD) describes the transport through the membrane or shell due to a concentration gradient. The solution-diffusion is generally used for nonporous membranes whose shell or membrane pore structure is not clear or they have continuous pores and therefore the flux across the membrane or shell is calculated as follow:

$$J_s = \frac{D\phi_s}{1 - \phi_s L} \quad (1.2)$$

Here, D is the diffusivity between the solvent and polymer membrane or shell<sup>76</sup>.

However, the permeability of specific particles or molecules depends on their size and polarity or the viscosity of the surrounding fluid. Changing the microcapsule permeability in response to *stimuli* is one of the most common ways to control the release system.

The most direct way of on-demand release is to release content over time by diffusion through a permeable capsule. In this class of responsive release, microcapsule permeability changes after it is triggered by temperature, pH, or another signaling method. There are several methods of evaluating capsule permeation of a polymer or tracer with known size. One method relies on the capsule allowing diffusion in different conditions that correspond with a trigger, dependant on differing situations the molecules will be included or excluded. In another method, to track changing diffusion with time or varying conditions, a polymer is labeled with a fluorescent dye and tracked using fluorescent or confocal microscopy.

Fluorescein isothiocyanate (FITC)-dextran with different molecular weights is usually used to measure diffusion rates in different conditions in order to estimate

the microcapsule pore size and capsule permeability changes in response to stimuli. Different sizes of FITC-dextran can be used to evaluate the size excluded before and after a change in triggered conditions to estimate the capsule cutoff range. For a more detailed studies of the diffusion rate and permeability of low molecular weight fluorescent probe, fluorescent recovery after photobleaching (FRAP) can be used. FRAP is based on the fluorescence of molecules in which a small region of the sample is bleached by exposure to strong laser intensity. The dynamics of fluorescence recovery as a function of time due to the diffusion of unbleached fresh fluorescent-labeled probes (FITC-dextran) in the bleached region can then be used to infer the mobility of the fluorescent molecules<sup>77</sup>. Figure 1.11 shows the fluorescent recovery after photobleaching (FRAP) was conducted using confocal microscopy. Low laser intensity is used at the beginning to capture equal emissions of the dye inside and outside the capsule, which appear with the same intensity. By increasing laser intensity in a specific region (inside the capsule), the fluorescent dye is bleached and appears in a dark color however, once unbleached fluorescent molecules diffuse through the capsule, the fluorescence intensifies within<sup>78</sup>.

Fluorescence intensity in the interior,  $I(t)$ , increases as the molecule diffuses through the porous membrane and reaches the maximum,  $I$ . The permeability of each molecule is estimated with a diffusion equation:

$$I(t) = I_0 + (I_s - I_0)(1 - e^{-s/vpt}) = I_0 + (I_s - I_0)(1 - e^{-3Pt/r}) \quad (1.3)$$

$$I = I_{ini}(1 - e^{-At}) \quad (1.4)$$

$I(t)$  and  $I_{ini}$  represent the intensity of fluorescence probe within microcapsule at time  $t = \infty$  and  $t=0$ , respectively, assuming that complete photobleaching is achieved

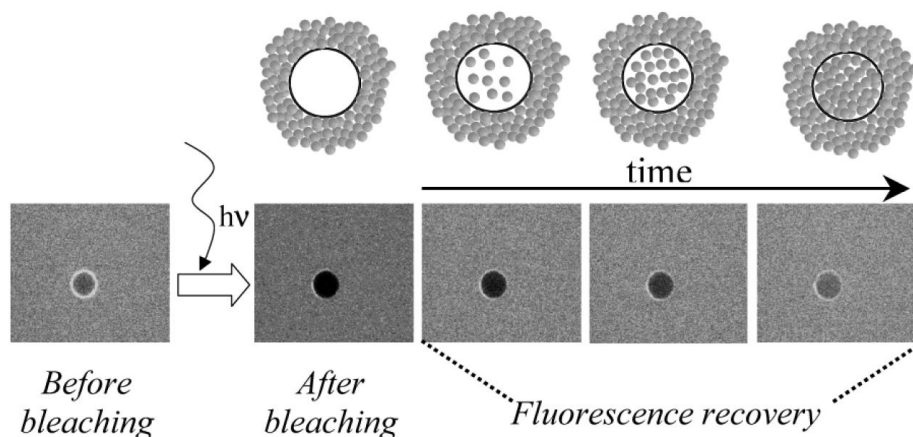


**Figure 1.11:** Typical confocal laser scanning microscopy (CLSM) measurement where the capsule permeability is quantified using fluorescence recovery after photo-bleaching (FRAP). The permeant molecule is the fluorescent dye fluorescein<sup>78</sup>. Reprinted with permission from<sup>78</sup>. Copyright 2002 American Chemical Society.

at  $t=0$ . The coefficient  $A$  is related to the diffusion coefficient according to

$$A = 3P/r = 3D/rh \quad (1.5)$$

For diffusion through a spherical wall with radius  $r$ ,  $P$  is permeability,  $t$  is diffusion time, and thickness  $h$ .

The structure of equation (1.4) follows as a solution to Fick's law

$$dc/dt = -A(C - C_0) \quad (1.6)$$

with  $C_0$  and  $C$  being the concentrations outside and inside the capsules, respectively<sup>78-80</sup>.

Ibarz et al.<sup>78</sup> employed FRAP to study the influence of thermal treatment on the permeability of polyelectrolyte multilayer capsules and the results showed that for capsules made of poly(styrene sulfonic acid) and poly(allylamine hydrochloride) the penetration of fluorescein reduces by three orders of magnitude when heated at

80°C. An et al.<sup>80</sup> produced lipid and protein microcapsules fabricated by alternating adsorption of human serum albumin (HSA) and 1- $\alpha$ -dimyristoylphosphatidic acid (DMPA) on a template and, subsequent removal of the core produced supplementary layers whose permeability as a function of pH were studied. The capsules were permeable for macromolecules (FITC-labeled dextran, Mw 40 kDa) at  $pH < 4.8$  and impermeable at  $pH > 7.4$ .

Chen et al.<sup>81</sup> synthesized hollow protein microcapsules simply by heating the microphase-separated soy glycinin microdomains. They used confocal laser scanning microscopy (CLSM) to study the permeability of soy glycinin microcapsules as influenced by ionic strength and pH using fluorescein isothiocyanate-dextran (FITC-dextran). They found the glycinin microcapsules kept their integrity between pH 1 and 11.5, swelled when pH was below 3 or above 11, dissociated at a pH above 11.5, and swelled slightly at pH 1. When the pH increased above 11, the permeability of the microcapsule significantly increased. Moreover, the permeability of microcapsules was also increased by adding salt but less significantly than by adjusting pH.

#### **1.3.2 Microcapsule flexibility and deformation**

Mechanical properties of capsules play an essential role in determining capsule deformability, stability, and durability when subjected to internal or external osmotic pressure or applied external forces. Thus, it is necessary to consider the mechanical characteristics of a microcapsule in designing them based on their future application. Progress in the development of advanced material science has allowed the production of microcapsules with a controlled nanoscale structure to achieve similar properties to biological capsules such as some degree of biomimetic control and response to the environment. This could allow the development of capsules, not

only in terms of stimuli-responsiveness, but also more targeted localized release. Designing microcapsules for specific tasks requires an understanding and control over physicochemical properties such as adhesion and mechanical properties of capsule membranes.

The material used in artificial capsule production is a key factor in determining capsule flexibility and elasticity. Biological capsules provide clear examples of a robust and flexible system to avoid membrane rupture in their complex deformation, however, based on their specific task, they could have different elasticity. An example of stable capsules that can undergo deformation without rupturing are red blood cells which are made from membranes with the lowest bending resistance seen in material science but are still highly resistant to stretching<sup>82</sup>. This allows them to squeeze through capillaries just 10% of their diameter without sustaining damage<sup>83</sup>, this deformation is visible in Figure 1.1. At the same time, pollen is an example of on-demand rupturing for the fast release of plant DNA in stigma. However, pollen has a high Young's modulus, around 9-15 GPa. Some biological capsule-like virus capsids are highly rigid, similar to glassy polymers, and can withstand pressures up to 10 MPa<sup>84</sup>. Besides their mechanical properties, capsule adhesion plays an important role as it is the property that allows microcapsules to adhere to surfaces, especially when they travel through channels or close to adhesive surfaces<sup>85-87</sup>. Wang et al.<sup>88</sup> developed a pollen-inspired capsule for drug delivery with strong adhesion properties. They were inspired by natural pollen polymer microparticles with surface textures and homogeneous size, which were fabricated through evaporation-induced interfacial instability of microfluidic droplet templates. The resultant particles exhibited controllable surface roughness and thus strong adhesion ability to the intestinal mucosa. Such particles were employed as novel drug

carriers, contributing to enhanced loading efficacy and controllable release kinetics.

Shell thickness plays an important role in capsule rigidity and mechanical stability<sup>83,89</sup>. Vian et al.<sup>89</sup> synthesized the mechanical responsive microcapsules with different shell diameters using water-oil-water double emulsions with sub-micron thick shells as a template. They used osmotic pressure to deform the synthesized capsule. They have found that, despite their thin shells, the capsules are mechanically robust such that they withstand at least 1.08 MPa without being deformed and pressures up to 2.75 MPa without losing their integrity.

Chen et al.<sup>90</sup> made microcapsules using double emulsion templates. They used polymers with selected glass transition temperatures as the shell material. They show through single capsule compression testing that hollow capsules can be prepared with tunable mechanical properties ranging from elastomeric to brittle. A quantitative statistical analysis of the load at rupture of brittle capsules is also provided to evaluate the variability of the microfluidic route and assist in the design of capsules in applications involving mechanically triggered release.

The remarkably distinct mechanical response of the capsules achieved by selecting polymers with tailored glass transition temperatures has important practical implications. Capsules that undergo brittle fracture are stiffer but can be ruptured at very low strains, making them suitable for situations where the release of encapsulants is desired under low external strain.

The human red blood cell circulates a million times in the body, squeezing through confined capillaries. The erythrocytes display outstanding mechanical properties and fluidity that allow them to undergo reversible recovery after deformation. Such shape recovery and flexibility come from the spectrin tetramer network tethered to

a phospholipid bilayer. The solid network's plastic deformation also manifests as high creep and yield regimes dependant on the strain rate<sup>13</sup>.

Stability and deformation are two critical factors of all-natural and artificial capsules, which can be incorporated to allow complex deformation. Holmes et al.<sup>91</sup> in their review paper explained how elastic instability can provide a multitude of ways to control shape based on bucking, folding, creasing, snapping, and wrinkling. Capsule deformation is either in-plane stretching and shear or out-of-plane bending. In most of the biological membranes, such as Venus flytrap<sup>92</sup>, pollen grains<sup>10</sup>, and red blood cells<sup>93</sup>, they have a low resistance to bending and shearing, and they deform via pure bending or shearing. However, the shape can be predicted based on the mean and Gaussian curvature of the local geometry of the membrane using the Helfrich-type Hamiltonian model. Shell elastic instability happens when the difference between the outer and inner pressure of the shell is enhanced above a critical value, which can cause shell deformation. Therefore, it is essential to define the critical buckling condition of the shell based on capsule or shell permeability, geometry, material properties, and elasticity<sup>94</sup>.

The theoretical prediction for the critical buckling pressure of a perfect spherical shell of radius  $R$  and thickness  $h$ , loaded under uniform pressure,  $p$ <sup>94</sup>:

$$P_c = (2E/\sqrt{3(1-\nu^2)})(R/h)^{-2} \quad (1.7)$$

where  $E$  and  $\nu$  are Young's modulus and Poisson's ratio of the material, respectively. The theoretical predictions for capsule buckling pressure help the neat design of the artificial capsule. Zoelley.<sup>95</sup> defines a knockdown factor,  $\kappa_d$ , as the ratio between the maximum experimental load sustained by the shell before buckling and the classic

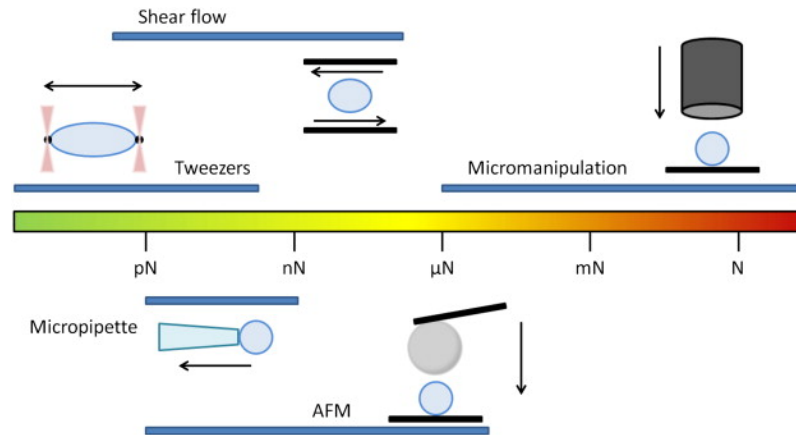


**Figure 1.12:** Schematic representation of single-capsule measurement techniques, each with typically available force range. Arrows indicate the directions in which forces are acting<sup>96</sup>, Reproduced with permission.<sup>96</sup> Copyright 2014, Elsevier.

theoretical prediction for thin shells. This number can be as low as  $0.2$ . However, most of the theoretical model is based on polymer-based capsules<sup>95</sup>.

$$\kappa_d = P_{max}/P_c \quad (1.8)$$

The microcapsule mechanical properties are accessible through a wide range of methods that can evaluate individual or multiple capsules. External osmotic pressure is a common method of multiple capsule deformation. Increasing the media osmotic pressure can deform and buckle the flexible microcapsules, depending on capsule shell thickness and elastic modulus. In order to obtain detailed information due to higher sensitivity regarding the capsule deformation, single-capsule measurement is used.

Several techniques have been reported to evaluate a single microcapsule's mechanical properties based on applied pressure, capsule response, and recovery after lifting applied force, such as parallel plate compression, atomic force microscopy (AFM)<sup>97</sup>, micropipette aspiration<sup>98</sup>, and shear flow<sup>99–102</sup>.

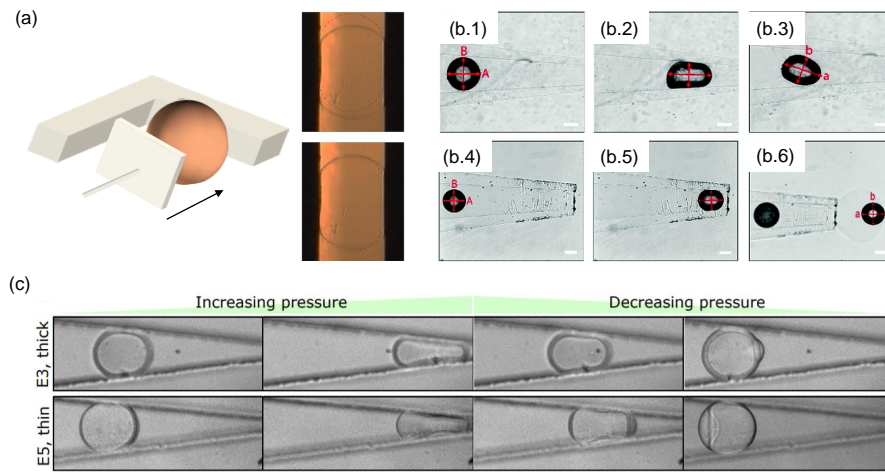


**Figure 1.13:** (a) Microcapsule deformation using the parallel plate<sup>103</sup>, Reproduced with permission<sup>103</sup> Copyright 2013, Springer Journal of Biorheology, (b) Pressure driven microcapsule deformation through a tapered capillary<sup>27</sup>. Reproduced with permission<sup>27</sup> Copyright 2015, The Royal Society of Chemistry, and (c) Microcapsule compression using the microfluidic channel<sup>104</sup>.

Atomic force microscopy (AFM) is an accurate method of microcapsule stress-strain measurement. In this method, a large spherical probe is glued to the AFM cantilever and pressed on individual objects or microcapsules. This allows simultaneous measurement of exerted stress and the capsule deformation<sup>105</sup>. In this method, a force in the range of  $pN$  and  $\mu N$  is applied to the microcapsule to measure the capsule mechanical properties during the small range deformation which is based on the capsule shell thickness. Instead of a large probe, the colloidal probe can be used to measure the sphere-sphere deformation geometry<sup>96</sup>. Often AFM can be combined with optics, reflection interference contrast, or confocal microscopy to observe the capsule's contact area during the deformation, seen in Figure 1.12.

Figure 1.12 shows the capsule deformation using various methods, including the shear stress which is typically used for forces ranging from  $mPa$  to  $kPa$ . However, for the capsule with average  $5 \mu m$  radius, the stress drops to  $0.1 pN$  and  $0.1 \mu N$ . In this method, the capsule is exposed to shear flow produced via concentric cylinder

rotation in opposite directions, and the capsule strain is captured using an optical or fluorescent microscope. The other method of evaluating microcapsule mechanical properties using a micropipette was initially developed to measure the elastic properties of living cells. In this technique, a glass micropipette with a movable reservoir uses suction pressure to deform the capsule which transfers partially into the pipette, and the amount of strain can be imaged using optical microscopy (e.g., Figure 1.13b and c).

Parallel plate compression is based on the capsule deformation between two approaching parallel plates equipped with a force transducer. This method is suitable for forces ranging from  $\mu N$  to  $N$  scale (Figure 1.12). The capsule is immobilized and deformed by the flat end of a cylindrical probe connected to the force transducer. The deformation is captured and measured using the optical microscopy<sup>96</sup>, measuring the burst forces of melamine formaldehyde microcapsule is an example of the use of parallel plates to deform microcapsules<sup>106</sup> (e.g., Figure 1.13 a).

Optical and magnetic tweezers are the other way of single microcapsule deformation. The magnitude of the applied stress is from several tens of  $N$  to several hundreds of  $pN$ , and this method is usually used for measuring the elastic modulus of the biological samples, and flexible microcapsule<sup>96</sup>.

## 1.4 Functional and stimuli responsive microcapsule

A biological cell has a complex chemical and mechanical structure to sense and respond to mechanical and chemical signals and perform a specific function at the same time<sup>107</sup>. For instance, cells undergo directed motion in response to mechanical variation in their environment, fibroblasts preferentially migrate from soft to hard surfaces<sup>108</sup>, and endothelial cells migrate towards applied fluidic shear stress<sup>13</sup>.

This inspires researchers to develop microcapsules with single or multiple functions.

The microcapsules' functionality is usually determined by the chemical and mechanical properties of the shell, which should be considered for targeted applications. Microcapsules are developed to safely store active ingredients and protect them from the surrounding environment. Therefore, in addition to efficient encapsulation, they are designed to release their contents or uptake from the surrounding environment. Hence, the shell should be made of a stimuli-responsive membrane, which means the pore size changes in response to external signals, or the shell degrades or ruptures under external driving forces (Figure 1.14).

Controlled release was defined in the early 1950s, based on the method reported by Pothakamury et al.<sup>109</sup> active and encapsulated ingredients are made available at the right time and rate. Since then, controlled release has been used to release active components including drugs, fragrance, flavor, and pesticides, to improve delivery efficiency and safety. The release rate varies based on many factors, including diffusion rate, the size and molecular weight of active ingredients, shell thickness, and pore size. Different release mechanisms occur based on the shell's structure and material properties. Therefore the controlled release mechanism is categorized as diffusion through porous shell, shell dissolution, and rupturing<sup>110</sup>, which can indicate different release profiles over time.

### **Microcapsule rupturing**

Usually, the most dramatic release is by a shell bursting in response to an internal or external applied shear force or pressure. Also, this type of release requires the impermeable or semipermeable shell with a brittle structure<sup>50</sup>. The magnitude of pressure varies depending on the shell elasticity. For instance, a metal-based

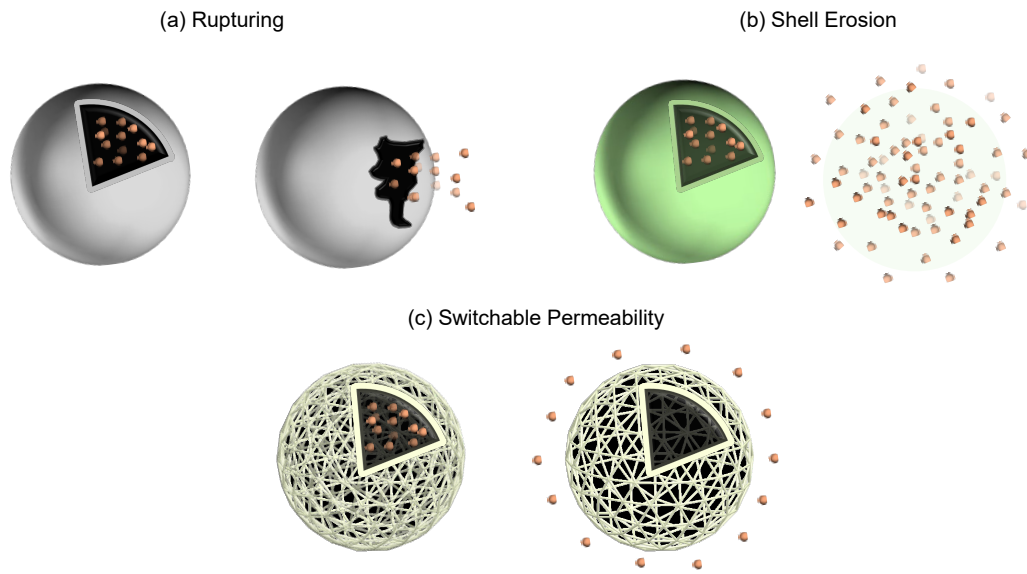


**Figure 1.14:** Different types of controlled release: (a) Microcapsule rupturing, (b) Shell erosion, and (c) Switchable permeability

microcapsule is in the order of several GPa, and a polymer-based microcapsule is in the order of several MPa<sup>111,112</sup>. For instance, 0.48 MPa and approximately 350 MPa stress are required to rupture melamine formaldehyde microcapsules with a radius ranging from 2.5 to 6  $\mu\text{m}$ <sup>113</sup>. For polymer composite nanospheres with a diameter ranging from 300 to 400 nm<sup>114</sup>, a stress greater than 0.8 GPa is needed. Additionally, for hydrogel-based microcapsules with a 400  $\mu\text{m}$  diameter, 42 kPa is required<sup>115</sup>.

The amount of release in the burst moment varies from 30 to 60%, and the rest of encapsulated content releases gradually with a constant rate due to diffusion<sup>116</sup>. The rupturing release profile has been shown in Figure 1.18<sup>110</sup>.

Microcapsule deformation and rupturing can be triggered by many factors such as osmotic pressure<sup>30</sup>, mechanical stress<sup>24</sup>, temperature<sup>117</sup>, specific solvent<sup>23</sup>, and pH<sup>21</sup>. Mechanical stress can also burst the shell structure above a certain threshold, which is determined by the material's elastic modulus. The failure of the shell

structure leads to cargo release. For instance, the polymeric shell can rupture under shear flow.

Microcapsule shell dissolution can also cause a dramatic release of the encapsulated content triggered by different stimuli like pH. When the polymer chains of the shell material become more highly charged and repel each other, the microcapsule shell dissolves at a constant rate. In this method, after several minutes, the shell becomes fully dissolved and the encapsulated content is released<sup>118</sup>.

It is worth mentioning that some capsules with porous shells, like bacterial cellulose microcapsules, will not rupture under internal or external pressure due to high porosity but can be buckled and deformed<sup>19</sup>. Figure 1.15 illustrates the effect of permeability on capsule rupturing, reported by Peyret et al.<sup>119</sup>, indicating that increasing the internal pressure in the impermeable capsule leads to the capsule rupturing. If the capsule is highly permeable, internal pressure reaches an equilibrium and the capsule will not rupturing.

Hence, microcapsule bursting and shell dissolution are suitable for rapid release of over 30% of encapsulated contents with the rate as high as 25  $\mu\text{L}/\text{min}$ <sup>24</sup>, which is not preferred in some applications such as drug delivery as sudden release may swing the drug concentration in the blood. In such applications, a more gradual sustained release is preferable, where the encapsulated ingredient diffuses through the shell over time.

### **Switchable permeability**

Capsules and membranes with switchable layer/wall permeability are particularly interesting for on-demand loading and release and microreactor applications. The permeability of capsules can be controlled by several factors, including the number of polymer layers, surface modification, and choice of polymer, which can deter-

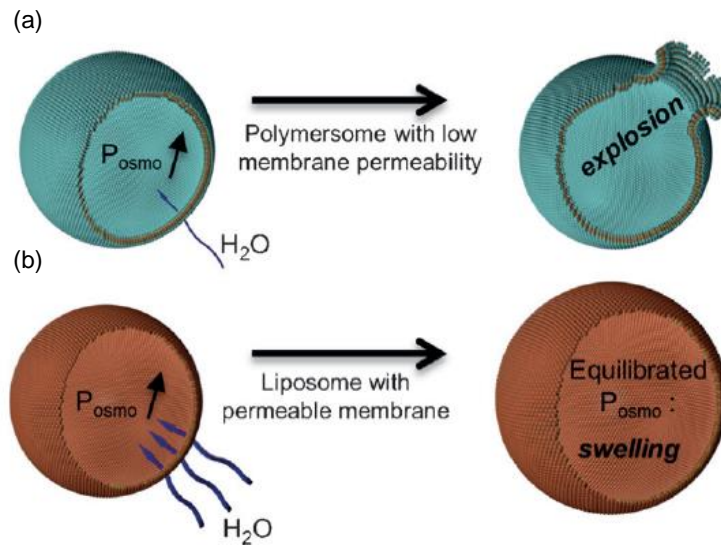


**Figure 1.15:** The effect of permeability of the release mechanism: a) The osmotic pressure enhances inside the capsule due to the impermeable membrane and prevents the internal solution leak out, leading the shell from bursting. b) The microcapsule internal pressure transiently increased when water diffused through the capsule and shell with high permeability; hence the capsule swelled without rupturing<sup>119</sup>. Reproduced with permission.<sup>119</sup>. Copyright 2017, Wiley-VCH.

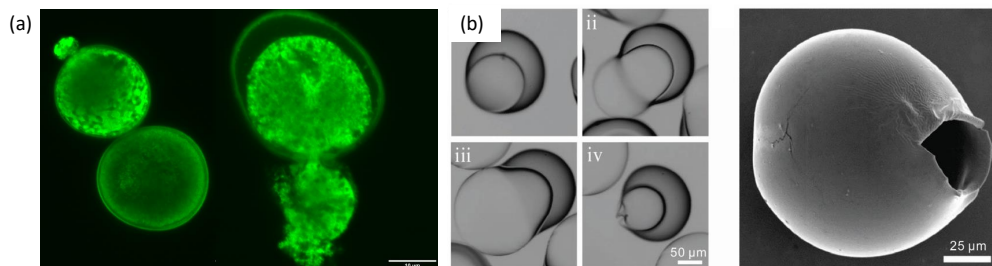


**Figure 1.16:** (a) Pollen grain rupturing under internal osmotic stress caused by pollen cytoplasm<sup>120</sup>, (b) Poly(ethylene glycol) divinyl ether microcapsules were swelled and ruptured internal osmotic pressure due to the mixture of sucrose and PVA<sup>30</sup>. Reproduced with permission.<sup>30</sup> Copyright 2019, Wiley-VCH.

mine the triggering stimuli factors such as pH<sup>81,121,122</sup>, light<sup>123</sup> temperature, salt, and redox reactions between capsules and external molecules.

The sensitivity of microcapsules to structural changes can be attributed to the transition (swelling or degradation) of shell copolymers caused by variations in the charge, redox potential, and mobility of functional groups in response to stimulus changes<sup>124,125</sup>. Other factors including chain architecture, solvent concentration, and ionic strength can affect the self-assembly of block copolymers and contribute to the stability and sensitivity of responsive microcapsules<sup>126</sup>. Kempe et al.<sup>127</sup> developed gated permeability using the reversible nature of the disulfide cross-linking. This feature can be achieved by introducing a photosensitive segment, whose activation leads to either rupture or modification of the diffusive properties of the capsule shell, allowing the delivery of the encapsulated material.

Figure 1.17 shows stimuli-responsive microcapsule with a polymer shell that has ON/OFF permeability which is triggered by adding salt to the media. In water, the microcapsule is permeable to 70 and 2000 kDa FITC-dextran with a hydrodynamic radius of 2 and 54 nm, respectively. However, 250 mM NaCl switched the permeability, and both FITC-dextran were trapped inside the capsule. Washing away the NaCl can change the permeability, resulting in the release of encapsulated FITC-dextran<sup>45</sup>.

### 1.4.1 Release profile

As mentioned in the above sections, controlled release can be achieved through various methods like switchable permeability or shell rupturing, which determines the concentrations of released content in the media. For example, pH-responsive capsules with a fibril scaffold shells have a capsule size 25  $\mu\text{m}$  and can encapsulate

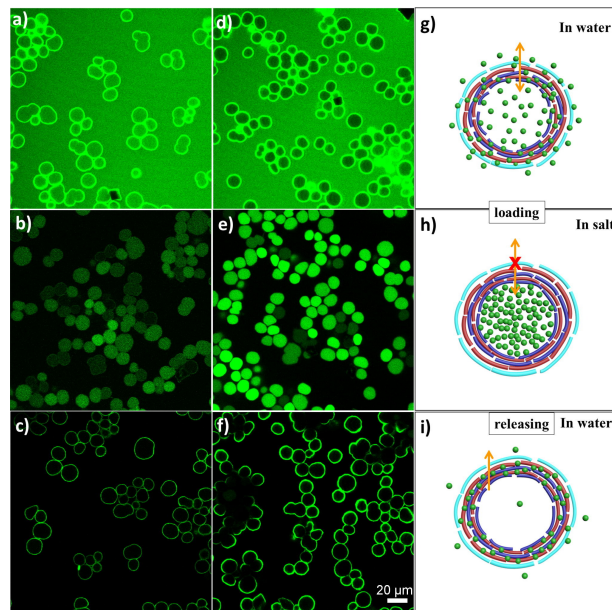


**Figure 1.17:** Switchable permeability triggered by salt. Microcapsules were soaked in 70 (a) and 2000 (d) kDa FITC-dextran aqueous solution. After adding the salt (250 mM NaCl), the FITC-dextran molecules are trapped in the microcapsule (b and e), and washing the capsule with water leads to the release of encapsulated FITC-dextran molecules (c and f).<sup>45</sup> Reprinted from<sup>45</sup>, Copyright (2018), with permission from Elsevier

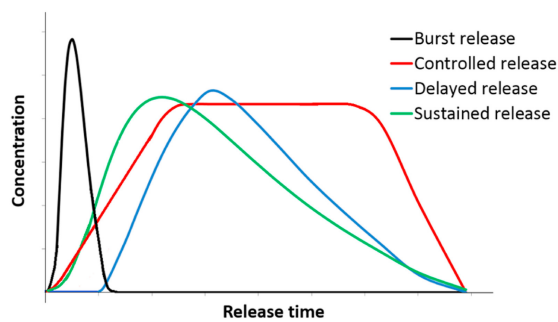


**Figure 1.18:** Various types of release profiles such as Burst or sudden release, controlled release, delayed release, and sustained release.<sup>110</sup> Reprinted from<sup>110</sup>, Copyright (2021), with permission from Elsevier

antibodies labeled with fluorescence which were used to report the diffusion rate of  $0.0001 \text{ cm}^2/\text{sec}$ <sup>128</sup>.

Long et al.<sup>24</sup> have reported the release rate of  $2.5 \mu\text{L}/\text{min}$  due to microcapsule rupturing, and Sun et al.<sup>129</sup> made microcapsules constructed through mussel-inspired chemistry for controlled release of insulin. They have reported time-dependent insulin release with a ratio of 73.1% at 3 h.

Hence, different releases can be seen and defined from different types of release mechanisms<sup>110</sup>, shown in Figure 1.18. As can be seen from Figure 1.18, burst release or uncontrolled leakage of the encapsulated cargo, more than 60% of the ingredient in the first stage, resulted in the rapid growth of cargo in the media followed by a plateau state due to diffusion of the rest of the cargo over time. The sustained and delayed release is defined as a long-acting release profile when at least twofold cargo release at the beginning and the rest occurs over time. The delayed release is commonly designed to release some food contents at later times and allows for more control over the release site. Controlled release refers to the condition when a change in various surrounding stimuli triggers the release<sup>110</sup>.

### 1.4.2 Responsive deformation

To date, there has been a significant research on developing responsive microcapsules with switchable permeability or release due to shell rupturing. Surprisingly, few studies developed the compression relaxation microcapsule, which is taken up and released through a shape transition mechanism. Figure 1.19 shows several attempts of synthesising controlled release microcapsules through compression and relaxation mechanism triggered by various stimuli such as hydration<sup>130</sup>, pH<sup>131</sup>, temperature<sup>132</sup>,  $\text{CO}_2$  gas<sup>134</sup>, and magnetic field<sup>24</sup>. They all highlighted the usage of the shape memory polymer as a key method of synthesizing a microcapsule

## 1.4. Functional and stimuli responsive microcapsule

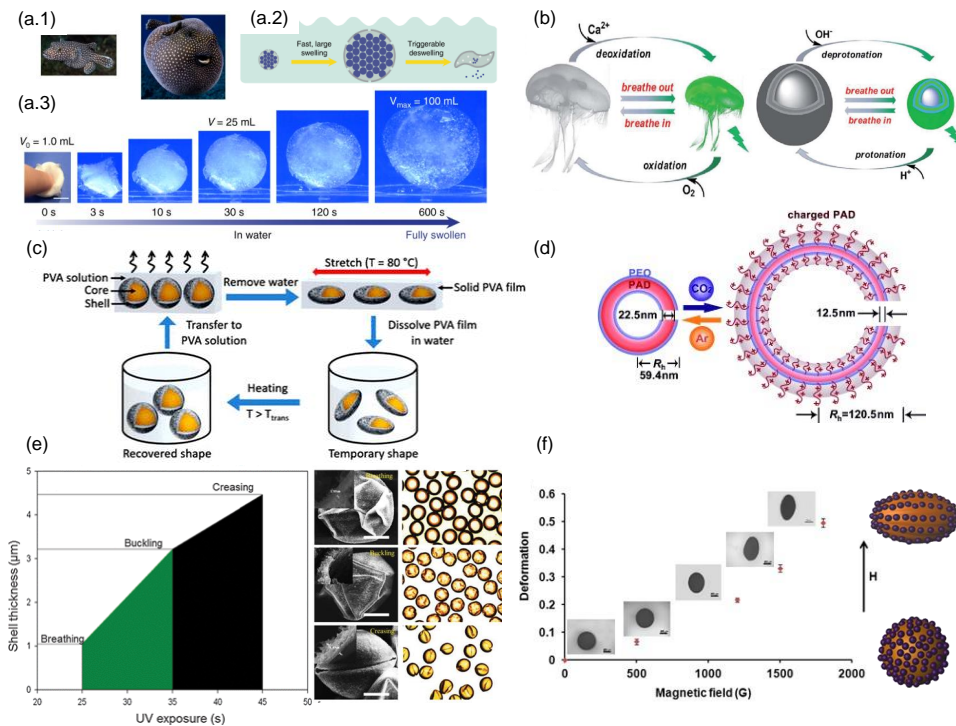


**Figure 1.19:** (a) Fast and high-ratio swelling spherical hydrogel with over 100 times shape transition within 600s<sup>130</sup> used for gastric retention device, (b) pH-responsive polymeric vesicles with switchable fluorescence<sup>131</sup>, Reproduced with permission.<sup>131</sup> Copyright 2012, Wiley-VCH. (c) Polyurethane microcapsules with active shape transition and deformation in response to temperature change<sup>132</sup> Reprinted (adapted) with permission from<sup>132</sup>. Copyright 2020 American Chemical Society, (d) Carbon dioxide ( $\text{CO}_2$ ) responsive polymeric vesicle used for drug delivery applications<sup>133</sup> Reproduced with permission.<sup>133</sup> Copyright 2011, Wiley-VCH, (e) Thermal responsive poly(NIPAAm)-AuNP microcapsule<sup>134</sup> Reproduced with permission.<sup>134</sup> Copyright 2013, The Royal Society of Chemistry, and (f) Magnetic responsive microcapsule<sup>24</sup>.

with active shape deformation and also pointed out the reusability of their capsule as the main advantage compared to conventional responsive microcapsules. For instance, Long et al.<sup>24</sup> synthesized a microcapsule with magnetic triggered controlled release. They have embedded the  $\text{Fe}_3\text{O}_4$  particles within the polymer shell and, by aligning the particles in the magnetic field to contract or stretch the shell, they have mentioned that this microcapsule has the potential for controllable and rapid release.

Among different signaling methods to trigger shape transition, hydration enables applications as diverse as oral uptake for food industries and drug delivery without the difficulties of having an external driving force like a magnetic field. However, making porous microcapsules with a flexible, robust structure for multiple cycles of active deformation is challenging and yet to be achieved. Also, it is worth noting the main goal of microcapsule preparation is optimizing the encapsulation of active ingredients to protect and release them at the appropriate time and rate with minimal dependency on external driving forces like an electrical or magnetic field.

### **1.5 Project aims and overview**

The previous studies show various synthetic microcapsules used for applications, including controlled release, cell protection, heat storage, self-healing cement, and environmental remediation. Synthesizing polymeric or metal microcapsule provides the opportunity to create responsive, controlled release systems via switchable permeability or triggered rupturing. However, most synthetic microcapsules suffer from low flexibility, permeability, and biodegradability, resulting in permanent deformation under internal or external stress, limiting their application in diverse sectors. Bacterially synthesized cellulose microcapsules were recently devel-

oped<sup>19</sup> with high permeability, low elasticity, and high purity, which is ideal for making functional, controlled release microcapsules. Bacterial cellulose microcapsules made from micron-size cellulose fibers are produced and woven together by *Acetobacter xylinum*, creating a textile-like shell structure with a high surface area. The main aim of this project is to engineer these bacterial cellulose microcapsules to develop applications with active shape deformation and motion. This enables creating advanced microcapsule functions with novel properties and higher performance for diverse applications. Three types of bacterial cellulose microcapsule modifications have been investigated, and the content of each chapter is briefly summarized below.

In Chapter 2, millimotor particles are designed and created from permeable bacterial cellulose capsules that have been partially coated with a metal-organic framework (MOF) and catalase enzymes. Two different propulsion mechanisms are dominant depending on the motor surface chemistry: oxygen bubbles are expelled from hydrophilic millimotors, driving motion via reaction force and buoyancy. Hydrophobic microcapsules remain attached to growing bubbles and move by buoyancy alone. Despite their large size, the low-density capsules compress to pass through contractions that would impede and be blocked by solid motor particles. The capsules' sparse structure and relatively large size enables them to transport significant volumes of liquid or other cargo using minimal solid particle mass as a motor support structure.

The development of a thermally responsive microcapsule with a permeable shell is studied in Chapter 3. Permeable microcapsules made from bacterial cellulose are functionalized with thermoresponsive poly(*N*-isopropyl acrylamide) to control permeability, shape response, and mechanical properties. These properties can be modulated by varying the amount of grafted polymer through changing reaction

conditions. Time-lapse microscopy demonstrates that the capsule exhibits a reversible mechanical response to temperature changes, driving exchange of solvent and capsule contents and the thorough mixing of the surrounding fluid. These results demonstrate the capability of the synthesized capsules for coupled release and convective mixing, building on Chapter 2 work for capsule mobility and response.

Soft and responsive microcapsules have been widely applied for diverse applications requiring stimulus-response, uptake, and release; Chapter 4 focuses on the cellulose microcapsule's ability to undergo extreme shape transition. A natural pollen grain capsule exhibits these properties as they can swell, encapsulate, and perform osmotically-triggered release of their contents. However, mimicking pollen grains' reversible folding and self-sealing during dehydration is complex due to material limitations. A recently synthesized bacterial cellulose microcapsule with a pore size larger than 500 nm has been physically coated with carboxymethyl cellulose to offset van der Waals interaction during drying. Dehydration conditions determine cellulose particles' final shape and size, so the millimeter-scale cellulose microcapsule can be dried to convert into an ultra-thin two-dimensional disk or other shape templated by the substrate used. The low density of the capsule means drying converts a millimeter-scale sphere into a nano- or micro-scale form. Single-particle drying experiments show that reversible drying and self-sealing allow for converting nanometer-thin structures into millimeter-scale spheres. This method can offer a simple and biodegradable procedure for developing responsive capsule creation.

In the last part of the thesis, Chapter 5, the conclusions of the thesis are integrated, and future research work is proposed. Some directions for multifunctional applications are proposed to enable applications in the area of functional particles and separation processes.

---

## References

- [1] M. G. Bah, H. M. Bilal, J. Wang, *Soft Matter* **2020**, *16*, 570–590.
- [2] M. Cavallaro, L. Botto, E. P. Lewandowski, M. Wang, K. J. Stebe, *Proceedings of the National Academy of Sciences* **2011**, *108*, 20923–20928.
- [3] A. M. Bakry, S. Abbas, B. Ali, H. Majeed, M. Y. Abouelwafa, A. Mousa, L. Liang, *Comprehensive Reviews in Food Science and Food Safety* **2016**, *15*, 143–182.
- [4] B. K. Green, S. Lowell, *Oil-containing microscopic capsules and method of making them*, **1957**, US Patent 2,800,457.
- [5] R. Dubey, *Defence Science Journal* **2009**, *59*, 82.
- [6] N. Inase, R. E. Schreck, S. C. Lazarus, *American Journal of Physiology-Lung Cellular and Molecular Physiology* **1993**, *264*, L387–L390.
- [7] H. Behrendt, W.-M. Becker, *Current Opinion In Immunology* **2001**, *13*, 709–715.
- [8] Y. Zheng, X. Deng, A. Qu, M. Zhang, Y. Tao, L. Yang, Y. Liu, J. Xu, S. Zhang, *PLoS Genetics* **2018**, *14*, e1007880.
- [9] Y. Xu, J. Yang, Y. Wang, J. Wang, Y. Yu, Y. Long, Y. Wang, H. Zhang, Y. Ren, J. Chen *et al.*, *PLoS Genetics* **2017**, *13*, e1006906.
- [10] E. Katifori, S. Alben, E. Cerda, D. R. Nelson, J. Dumais, *Proceedings of the National Academy of Sciences* **2010**, *107*, 7635–7639.
- [11] A. V. Pogorelov, *Bendings of surfaces and stability of shells*, Vol. 72, American Mathematical Soc., **1988**.
- [12] C. Quilliet, C. Zoldesi, C. Riera, A. Van Blaaderen, A. Imhof, *The European Physical Journal E* **2008**, *27*, 13–20.
- [13] J. Li, G. Lykotrafitis, M. Dao, S. Suresh, *Proceedings of the National Academy of Sciences* **2007**, *104*, 4937–4942.

## References

---

- [14] I. V. Pivkin, Z. Peng, G. E. Karniadakis, P. A. Buffet, M. Dao, S. Suresh, *Proceedings of the National Academy of Sciences* **2016**, *113*, 7804–7809.
- [15] C. Contini, W. Hu, Y. Elani, *Chemical Communications* **2022**, *58*, 4409–4419.
- [16] H. Li, Y. Ma, Z. Li, J. Ji, Y. Zhu, H. Wang, *RSC Advances* **2017**, *7*, 50328–50335.
- [17] D. Sun, H. Zhang, X. Zhang, J. Yang, *ACS Applied Materials & Interfaces* **2019**, *11*, 9621–9628.
- [18] S. Wang, K. Lei, Z. Wang, H. Wang, D. Zou, *Chemical Engineering Journal* **2022**, 135559.
- [19] J. Song, F. Babayekhorasani, P. T. Spicer, *Biomacromolecules* **2019**, *20*, 4437–4446.
- [20] N. Pircher, S. Veigel, N. Aigner, J.-M. Nedelec, T. Rosenau, F. Liebner, *Carbohydrate Polymers* **2014**, *111*, 505–513.
- [21] S. S. Datta, A. Abbaspourrad, D. A. Weitz, *Materials Horizons* **2014**, *1*, 92–95.
- [22] A. Kanellopoulos, P. Giannaros, D. Palmer, A. Kerr, A. Al-Tabbaa, *Smart Materials and Structures* **2017**, *26*, 045025.
- [23] A. Abbaspourrad, N. J. Carroll, S.-H. Kim, D. A. Weitz, *Journal of the American Chemical Society* **2013**, *135*, 7744–7750.
- [24] Y. Long, C. Liu, B. Zhao, K. Song, G. Yang, C.-H. Tung, *NPG Asia Materials* **2015**, *7*, e148–e148.
- [25] W. Wang, L. Liu, X.-J. Ju, D. Zerrouki, R. Xie, L. Yang, L.-Y. Chu, *ChemPhysChem* **2009**, *10*, 2405–2409.
- [26] L. Lv, Z. Yang, G. Chen, G. Zhu, N. Han, E. Schlangen, F. Xing, *Construction and Building Materials* **2016**, *105*, 487–495.
- [27] G. Kaufman, S. Nejati, R. Sarfati, R. Boltyanskiy, M. Loewenberg, E. R. Dufresne, C. O. Osuji, *Soft Matter* **2015**, *11*, 7478–7482.

- 
- [28] G. Peng, G. Dou, Y. Hu, Y. Sun, Z. Chen, *Advances in Polymer Technology* **2020**, 2020, year.
- [29] M. W. Patchan, L. M. Baird, Y.-R. Rhim, E. D. LaBarre, A. J. Maisano, R. M. Deacon, Z. Xia, J. J. Benkoski, *ACS Applied Materials & Interfaces* **2012**, 4, 2406–2412.
- [30] W. Zhang, L. Qu, H. Pei, Z. Qin, J. Didier, Z. Wu, F. Bobe, D. E. Ingber, D. A. Weitz, *Small* **2019**, 15, 1903087.
- [31] X. Xie, W. Zhang, A. Abbaspourrad, J. Ahn, A. Bader, S. Bose, A. Vegas, J. Lin, J. Tao, T. Hang *et al.*, *Nano Letters* **2017**, 17, 2015–2020.
- [32] F. Ahangaran, A. H. Navarchian, F. Picchioni, *Journal of Applied Polymer Science* **2019**, 136, 48039.
- [33] Y.-T. Huang, H. Zhang, X.-J. Wan, D.-Z. Chen, X.-F. Chen, X. Ye, X. Ouyang, S.-Y. Qin, H.-X. Wen, J.-N. Tang, *Journal of Materials Chemistry A* **2017**, 5, 7482–7493.
- [34] Y. Tian, X. Huang, Y. Cheng, Y. Niu, Q. Meng, J. Ma, Y. Zhao, X. Kou, Q. Ke, *Journal of Applied Polymer Science* **2022**, 139, e52650.
- [35] R. Urbas, R. Milošević, N. Kašiković, Ž. Pavlović, U. S. Elesini, *Iranian Polymer Journal* **2017**, 26, 541–561.
- [36] X. Wang, R. Han, T. Han, N. Han, F. Xing, *Materials Chemistry and Physics* **2018**, 215, 346–354.
- [37] Y. Zhang, Y. Wang, Y. Li, Z. Zhang, *Polymers* **2019**, 11, 1447.
- [38] J. Cui, M. Björnalm, K. Liang, C. Xu, J. P. Best, X. Zhang, F. Caruso, *Advanced Materials* **2014**, 26, 7295–7299.
- [39] R. Haghgoie, M. Toner, P. S. Doyle, *Macromolecular Rapid Communications* **2010**, 31, 128–134.

## References

---

- [40] A. Ashimova, S. Yegorov, B. Negmetzhanov, G. Hortelano, *Frontiers in Bioengineering and Biotechnology* **2019**, 7, 380.
- [41] Y. Ma, W.-F. Dong, M. A. Hempenius, H. Möhwald, G. Julius Vancso, *Nature Materials* **2006**, 5, 724–729.
- [42] Y. Cai, Y. Chen, X. Hong, Z. Liu, W. Yuan, *International Journal of Nanomedicine* **2013**, 8, 1111.
- [43] C. Peng, Q. Zhao, C. Gao, *Colloids and Surfaces A: Physicochemical and Engineering aspects* **2010**, 353, 132–139.
- [44] C. Ye, S. T. Malak, K. Hu, W. Wu, V. V. Tsukruk, *Acs Nano* **2015**, 9, 10887–10895.
- [45] T. Paulraj, A. Riazanova, A. Svagan, *Acta Biomaterialia* **2018**, 69, 196–205.
- [46] T. Paulraj, S. Wennmalm, A. V. Riazanova, Q. Wu, G. A. Crespo, A. J. Svagan, *ACS Applied Materials & Interfaces* **2018**, 10, 41146–41154.
- [47] Y. Ma, Z. Li, H. Wang, H. Li, *Journal of Colloid and Interface Science* **2019**, 534, 469–479.
- [48] Z. Wu, J. G. Werner, D. A. Weitz, *ACS Macro Letters* **2020**, 10, 116–121.
- [49] E. Loiseau, F. Niedermair, G. Albrecht, M. Frey, A. Hauser, P. A. Rühs, A. R. Studart, *Langmuir* **2017**, 33, 2402–2410.
- [50] H. N. Yow, A. F. Routh, *Soft Matter* **2006**, 2, 940–949.
- [51] K. Manjanna, B. Shivakumar, T. P. Kumar, *Critical Reviews™ in Therapeutic Drug Carrier Systems* **2010**, 27, year.
- [52] X. Huang, B. Voit, *Polymer Chemistry* **2013**, 4, 435–443.
- [53] O. Nguon, F. Lagugné-Labarthet, F. A. Brandys, J. Li, E. R. Gillies, *Polymer Reviews* **2018**, 58, 326–375.
- [54] G. T. Vladislavljević in *Current Trends and Future Developments on (Bio-) Membranes*, Elsevier, **2019**, pp. 167–222.

- 
- [55] L.-Y. Chu, S.-H. Park, T. Yamaguchi, S.-i. Nakao, *Langmuir* **2002**, *18*, 1856–1864.
- [56] A. B. D. Nandiyanto, K. Okuyama, *Advanced Powder Technology* **2011**, *22*, 1–19.
- [57] N. Alhajj, N. J. O'Reilly, H. Cathcart, *Powder Technology* **2021**, *384*, 313–331.
- [58] E. Both, R. Boom, M. Schutyser, *Powder Technology* **2020**, *363*, 519–524.
- [59] P. Zhao, W. Yi, Q. Cao, B. Zhang, K. Chen, R. Dang, J. Chen, *Nanoscale Research Letters* **2019**, *14*, 1–9.
- [60] S. V. Jangam, *Drying Technology* **2011**, *29*, 1343–1357.
- [61] W. Li, L. Zhang, X. Ge, B. Xu, W. Zhang, L. Qu, C.-H. Choi, J. Xu, A. Zhang, H. Lee *et al.*, *Chemical Society Reviews* **2018**, *47*, 5646–5683.
- [62] L. Shang, Y. Cheng, J. Wang, H. Ding, F. Rong, Y. Zhao, Z. Gu, *Lab on a Chip* **2014**, *14*, 3489–3493.
- [63] Y. Liu, L. Sun, H. Zhang, L. Shang, Y. Zhao, *Chemical Reviews* **2021**, *121*, 7468–7529.
- [64] J.-W. Kim, S. H. Han, Y. H. Choi, W. M. Hamonangan, Y. Oh, S.-H. Kim, *Lab on a Chip* **2022**.
- [65] R. Al Nuamani, G. Bolognesi, G. T. Vladislavljevic, *Langmuir* **2018**, *34*, 11822–11831.
- [66] A. K. Prabhakar, M. G. Potroz, S. Park, E. Miyako, N.-J. Cho, *Particle & Particle Systems Characterization* **2018**, *35*, 1800151.
- [67] A.-S. Y. Mohammed, A. K. Dyab, F. Taha, A. I. Abd El-Mageed, *RSC Advances* **2022**, *12*, 22139–22149.
- [68] A. Diego-Taboada, S. T. Beckett, S. L. Atkin, G. Mackenzie, *Pharmaceutics* **2014**, *6*, 80–96.

## References

---

- [69] M. G. Potroz, R. C. Mundargi, J. H. Park, E.-L. Tan, N.-j. Cho, *JoVE (Journal of Visualized Experiments)* **2016**, e54768.
- [70] J. H. Park, J. Seo, J. A. Jackman, N.-J. Cho, *Scientific Reports* **2016**, *6*, 1–10.
- [71] T. Maric, M. Z. M. Nasir, N. F. Rosli, M. Budanović, R. D. Webster, N.-J. Cho, M. Pumera, *Advanced Functional Materials* **2020**, *30*, 2000112.
- [72] A. K. Prabhakar, M. G. Potroz, E.-L. Tan, H. Jung, J. H. Park, N.-J. Cho, *ACS Applied Materials & Interfaces* **2018**, *10*, 28428–28439.
- [73] P. A. Rühls, F. Storz, Y. A. López Gómez, M. Haug, P. Fischer, *npj Biofilms and Microbiomes* **2018**, *4*, 1–6.
- [74] A. P. Dhand, R. Poling-Skutvik, C. O. Osuji, *Soft Matter* **2021**, *17*, 4517–4524.
- [75] A. A. Antipov, G. B. Sukhorukov, *Advances in Colloid and Interface Science* **2004**, *111*, 49–61.
- [76] V. H. Hegde, M. F. Doherty, T. M. Squires, *Science* **2022**, *377*, 186–191.
- [77] A. Bläßle, G. Soh, T. Braun, D. Mörsdorf, H. Preiß, B. M. Jordan, P. Müller, *Nature Communications* **2018**, *9*, 1–14.
- [78] G. Ibarz, L. Dähne, E. Donath, H. Möhwald, *Chemistry of Materials* **2002**, *14*, 4059–4062.
- [79] D. Lee, D. A. Weitz, *Advanced Materials* **2008**, *20*, 3498–3503.
- [80] Z. An, H. Möhwald, J. Li, *Biomacromolecules* **2006**, *7*, 580–585.
- [81] N. Chen, J. Zhang, L. Mei, Q. Wang, *Langmuir* **2018**, *34*, 9711–9718.
- [82] R. Lipowsky, E. Sackmann, *Structure and dynamics of membranes: I. from cells to vesicles/II. generic and specific interactions*, Elsevier, **1995**.
- [83] A. Fery, R. Weinkamer, *Polymer* **2007**, *48*, 7221–7235.
- [84] R. Zandi, D. Reguera, *Physical Review E* **2005**, *72*, 021917.
- [85] C. Pozrikidis, *Modeling and simulation of capsules and biological cells*, CRC Press, **2003**.

- 
- [86] A. Alexeev, R. Verberg, A. C. Balazs, *Physical Review Letters* **2006**, 96, 148103.
- [87] D. Boal, D. H. Boal, *Mechanics of the Cell*, Cambridge University Press, **2012**.
- [88] Y. Wang, L. Shang, G. Chen, C. Shao, Y. Liu, P. Lu, F. Rong, Y. Zhao, *Applied Materials Today* **2018**, 13, 303–309.
- [89] A. Vian, E. Amstad, *Soft Matter* **2019**, 15, 1290–1296.
- [90] P. W. Chen, R. M. Erb, A. R. Studart, *Langmuir* **2012**, 28, 144–152.
- [91] D. P. Holmes, *Current Opinion in Colloid & Interface Science* **2019**, 40, 118–137.
- [92] Y. Forterre, J. M. Skotheim, J. Dumais, L. Mahadevan, *Nature* **2005**, 433, 421–425.
- [93] G. L. HW, M. Wortis, R. Mukhopadhyay, *Proceedings of the National Academy of Sciences* **2002**, 99, 16766–16769.
- [94] A. Lee, D. Yan, M. Pezulla, D. P. Holmes, P. M. Reis, *Soft Matter* **2019**, 15, 6134–6144.
- [95] R. Zoelly, *Über ein Knickungsproblem an der Kugelschale [PhD thesis]*, **1915**.
- [96] M. P. Neubauer, M. Poehlmann, A. Fery, *Advances in Colloid and Interface Science* **2014**, 207, 65–80.
- [97] V. Lulevich, I. Radtchenko, G. Sukhorukov, O. I. Vinogradova, *The Journal of Physical Chemistry B* **2003**, 107, 2735–2740.
- [98] R. M. Hochmuth, *Journal of Biomechanics* **2000**, 33, 15–22.
- [99] D. Barthes-Biesel, *Annual Review of fluid mechanics* **2016**, 48, 25–52.
- [100] Y. Hiramoto, *Experimental Cell Research* **1963**, 32, 59–75.
- [101] M. Carin, D. Barthès-Biesel, F. Edwards-Lévy, C. Postel, D. C. Andrei, *Biotechnology and Bioengineering* **2003**, 82, 207–212.
- [102] F. Risso, M. Carin, *Physical Review E* **2004**, 69, 061601.
- [103] K. Bando, K. Ohba, Y. Oiso, *Journal of Biorheology* **2013**, 27, 18–25.

## References

---

- [104] Y. Xu, Y. Shen, T. C. Michaels, K. N. Baumann, D. Vigolo, Q. Peter, Y. Lu, K. L. Saar, D. Vella, H. Zhu *et al.*, *arXiv preprint arXiv:2009.13413* **2020**.
- [105] P. A. Fernandes, M. Delcea, A. G. Skirtach, H. Möhwald, A. Fery, *Soft Matter* **2010**, *6*, 1879–1883.
- [106] Z. Zhang, *Journal of Microencapsulation* **1999**, *16*, 117–124.
- [107] G. V. Kolmakov, A. Schaefer, I. Aranson, A. C. Balazs, *Soft Matter* **2012**, *8*, 180–190.
- [108] C.-M. Lo, H.-B. Wang, M. Dembo, Y.-I. Wang, *Biophysical Journal* **2000**, *79*, 144–152.
- [109] R. Usha, U. Pothakamury, *Food Sci and Technol* **1995**, *6*, 397–406.
- [110] S. Boostani, S. M. Jafari, *Trends in Food Science & Technology* **2021**, *109*, 303–321.
- [111] A. Gray, S. Egan, S. Bakalis, Z. Zhang, *Particuology* **2016**, *24*, 32–43.
- [112] L. Guadagno, M. Raimondo, U. Vietri, C. Naddeo, A. Stojanovic, A. Sorrentino, W. H. Binder, *International Journal of Aerospace Engineering* **2016**, *2016*, year.
- [113] R. Mercadé-Prieto, R. Allen, Z. Zhang, D. York, J. A. Preece, T. E. Goodwin, *AIChE journal* **2012**, *58*, 2674–2681.
- [114] D. Guo, J. Li, G. Xie, Y. Wang, J. Luo, *Langmuir* **2014**, *30*, 7206–7212.
- [115] S. R. Bhattarai, S. Saudi, S. Khanal, S. Aravamudhan, C. J. Rorie, N. Bhattarai, *RSC advances* **2021**, *11*, 4921–4934.
- [116] F. P. Flores, F. Kong, *Annual Review of Food Science and Technology* **2017**, *8*, 237–259.
- [117] M. Windbergs, Y. Zhao, J. Heyman, D. A. Weitz, *Journal of the American Chemical Society* **2013**, *135*, 7933–7937.
- [118] A. Abbaspourrad, S. S. Datta, D. A. Weitz, *Langmuir* **2013**, *29*, 12697–12702.

- 
- [119] A. Peyret, E. Ibarboure, A. Tron, L. Beauté, R. Rust, O. Sandre, N. D. McClenaghan, S. Lecommandoux, *Angewandte Chemie International Edition* **2017**, *56*, 1566–1570.
- [120] G. Mackenzie, S. Beckett, S. Atkin, A. Diego-Taboada in *Microencapsulation in the food industry*, Elsevier, **2014**, pp. 283–297.
- [121] J. G. Werner, B. T. Deveney, S. Nawar, D. A. Weitz, *Advanced Functional Materials* **2018**, *28*, 1803385.
- [122] Z. Wang, J. Gao, V. Ustach, C. Li, S. Sun, S. Hu, R. Faller, *Langmuir* **2017**, *33*, 7288–7297.
- [123] V. Marturano, P. Cerruti, M. Giamberini, B. Tylkowski, V. Ambrogi, *Polymers* **2017**, *9*, 8.
- [124] M. A. C. Stuart, W. T. Huck, J. Genzer, M. Müller, C. Ober, M. Stamm, G. B. Sukhorukov, I. Szleifer, V. V. Tsukruk, M. Urban *et al.*, *Nature Materials* **2010**, *9*, 101–113.
- [125] J. Gaitzsch, X. Huang, B. Voit, *Chemical Reviews* **2016**, *116*, 1053–1093.
- [126] S. Piogé, A. Nesterenko, G. Brotons, S. Pascual, L. Fontaine, C. Gaillard, E. Nicol, *Macromolecules* **2011**, *44*, 594–603.
- [127] K. Kempe, K. F. Noi, S. L. Ng, M. Müllner, F. Caruso, *Polymer* **2014**, *55*, 6451–6459.
- [128] U. Shimanovich, A. Levin, D. Eliaz, T. Michaels, Z. Toprakcioglu, B. Frohm, E. De Genst, S. Linse, K. S. Åkerfeldt, T. P. Knowles, *Small* **2021**, 2007188.
- [129] Y. Sun, J. Shi, Z. Cai, Y. Wu, W. Li, Q. Huo, Z. Jiang, *Materials Chemistry Frontiers* **2021**, *5*, 792–798.
- [130] X. Liu, C. Steiger, S. Lin, G. A. Parada, J. Liu, H. F. Chan, H. Yuk, N. V. Phan, J. Collins, S. Tamang *et al.*, *Nature Communications* **2019**, *10*, 1–10.

## References

---

- [131] R. Dong, B. Zhu, Y. Zhou, D. Yan, X. Zhu, *Angewandte Chemie International Edition* **2012**, *51*, 11633–11637.
- [132] F. Zhang, T. Zhao, D. Ruiz-Molina, Y. Liu, C. Roscini, J. Leng, S. K. Smoukov, *ACS Applied Materials & Interfaces* **2020**, *12*, 47059–47064.
- [133] Q. Yan, R. Zhou, C. Fu, H. Zhang, Y. Yin, J. Yuan, *Angewandte Chemie International Edition* **2011**, *50*, 4923–4927.
- [134] S. Lone, G. S. Ghodake, D. S. Lee, I. W. Cheong, *New Journal of Chemistry* **2013**, *37*, 877–881.

## Chapter 2

# Propulsion, deformation, and confinement response of hollow nanocellulose millimotors

## 2.1 Introduction

Microorganisms can propel themselves through liquid by different swimming mechanisms, and synthetic particle motors, termed “active matter”, have been created that mimic microbial motion by chemical, rather than mechanical, means<sup>1-3</sup>. Particulate nanomotors and micromotors move by converting chemical fuel from their environment into kinetic energy, and can achieve remarkable speeds relative to their body length<sup>4,5</sup>. Propulsion can be driven by self-generated solute gradients or electric fields<sup>1</sup> or by formation of gas bubbles that cause buoyancy or ejection-induced recoil effects<sup>6</sup>. Applications for the small motors are imagined in drug delivery<sup>2,7-9</sup>, environmental remediation<sup>10-14</sup>, and self-assembly<sup>15,16</sup> while the particles’ unique motion is widely studied as well<sup>17</sup>. Larger, millimeter-scale motors have recently been developed from clay/DNA membranes to act as synthetic protocells that move and carry out internal biochemical reactions<sup>18</sup>. These larger-scale motors can broaden the possible applications of active matter, motivating us to develop a millimotor capsule that is easily functionalized but can also overcome difficulties most motors face with confined space navigation and sedimentation potential<sup>19</sup>.

Our approach to develop these new millimotors takes inspiration from the biological cells that active matter seeks to mimic. Cells are partially permeable to water, minimizing density differences, while their softness enables them to deform and pass through narrow spaces and navigate confined environments. By contrast, most synthetic active particles are made using dense solid materials, like platinum or silica, whose large density differences with water promote sedimentation. Such particles are also too rigid to deform and escape environmental confinement<sup>19</sup>. A recent review<sup>20</sup> identified low density and robust deformability as important goals for future motor particles, and this work focuses on a new approach to meeting these challenges using unconventionally large motor capsules made from a mesh of bacterial cellulose fibers.

Hollow capsules are a promising way to minimise mass use and density issues in motor particles<sup>21–25</sup> and their low density makes them behave like much smaller particles in fluid<sup>26</sup>. A recently developed bacterial cellulose capsule<sup>27</sup> provides a unique minimalist scaffolding for millimotor particle development, and we explore their motion and response after coating them with two different metal-organic framework (MOF) nanoparticles<sup>28</sup>. The MOFs attach onto the capsule's cellulose nanofibers<sup>29–31</sup> and trap catalase enzyme in their structure<sup>2,31</sup>, enabling conversion of aqueous hydrogen peroxide fuel into oxygen bubbles to drive motion<sup>18,32</sup>. The MOF surface polarity determines the mode of millimotor propulsion by altering oxygen bubble affinity for the capsule surface. The velocity and motion of the driven capsules are measured by optical microscopy and shown to be quite efficient compared to solid micro- and nanomotors, despite being much larger and full of liquid. The low-density shells are efficient motor bases because of their structural integrity and minimal mass, but also provide unique benefits for bubble-driven flow. The flexible nanocellulose fiber struts allow significant deformation when passing through con-

strictions and the permeable capsules form a low-friction gas layer on the capsules that further enhances escape from confined spaces.

## 2.2 Methods and Materials

**Cellulose capsule preparation:** Cellulose capsules were synthesized by a biointerfacial polymerization process we previously developed<sup>27</sup>. Bacterial cellulose capsules were grown using a water-in-oil emulsion of bacterial culture droplets as templates. No surfactants are used as they would harm the cellulose-producing bacteria. Instead, the aqueous drops of bacterial culture are suspended in oil with a yield stress of  $\sim 10$  Pa as a result of crystallized hydrogenated castor oil wax. The yield stress keeps the droplets suspended and stable against coalescence<sup>27</sup>. The bacteria partition at droplet interfaces to access nutrients and oxygen, producing cellulose there that gradually becomes strongly entangled and can't move away from the interface once growth is complete.

The bacterial culture contains purified *Acetobacter xylinum* concentrated from Kombucha culture (Nourishme Organics, Australia) by gradient centrifugation, coconut water (Cocobella, Indonesia), and 10% w/v table sugar. Within 10 days, the encapsulated bacteria polymerize glucose molecules into cellulose nanofibers, with a diameter of 60 – 70 nm, that entangle to form a fiber mesh shell with a total thickness of 20 – 50  $\mu\text{m}$  and a pore size of 0.5  $\mu\text{m}$ <sup>27</sup> at the oil-water interface. Subsequently, catalase-zinc 2-methylimidazole (ZIFL) and catalase-zinc imidazolate-2-carboxyaldehyde (ZIF90) MOF crystals were grown *in situ* on the nanofibers, producing hydrophobic and hydrophilic millimotors, respectively. Capsules ranged between 0.2-0.8 mm in diameter for both hydrophilic and hydrophobic particles.

**Hydrophobic ZIFL coating:** 5 g of catalase from bovine liver, (Sigma Aldrich), 200  $\mu\text{L}$  of 14.8 mM zinc nitrate ( $ZnNO_3$ , Sigma Aldrich) aqueous solution and 2 mL

of 714 mM 2-methylimidazole (Sigma Aldrich) aqueous solution were added to 1 mL of cellulose capsule dispersion. The mixture was mixed for 1 hr and then rinsed several times with deionized water.

**Hydrophilic ZIF90 coating:** 5 g of catalase, 2 mL of 40 mM zinc nitrate ( $ZnNO_3$ , Sigma Aldrich) aqueous solution and 2 mL of 160 mM imidazole-2-carboxyaldehyde (Sigma Aldrich) aqueous solution were added to 1 mL of cellulose capsule dispersion. The mixture was mixed for 1 h and rinsed with deionized water several times, Figure 2.1.

**Enzyme labelling:** 8.5 mg of Rhodamine B isothiocyanate (RhB, Sigma Aldrich Australia) was dissolved in 0.5 mL dimethyl sulphoxide (DMSO, Sigma Aldrich). In a glass vial, 40 mg of catalase was placed in 2 mL of sodium carbonate bicarbonate buffer (0.5 M, pH 9.5). Then, the RhB solution was added slowly into catalase solution. The CAT-RhB was then mixed for 2 h at room temperature in darkness. The unreacted enzymes were separated from the labelled enzymes in an Illustra NAP-25 column (GE Healthcare). The first band eluted with Milli-Q water, which contains labeled enzymes, was collected for sample preparation.

**MOF and cellulose labelling:** Congo Red and fluorescein isothiocyanate (FITC) were used to stain cellulose fibers and MOF crystals, respectively for visualization by addition of 34 mg of 0.5 wt% aqueous Congo Red solution to 1 mL of a cellulose capsule dispersion. The MOF is labeled with FITC using an existing procedure to covalently conjugate FITC to the organic ligands of the MOF<sup>33,34</sup>. Here 8 mg of FITC is dissolved in 2.5 mL of DMSO then added to the MOF solution. Sequentially the cellulose is first labeled with Congo Red, then MOFs with FITC. All samples incubated with FITC were kept dark and covered with aluminum foil to avoid photobleaching prior to confocal imaging.

### 2.2.1 Sample imaging and analysis

**Microscopy:** Confocal and light sheet microscopy imaging experiments were carried out on a Zeiss LSM 880 with Airy scan<sup>35</sup>, and Zeiss Lightsheet Z.1 (Germany) microscope. A 63× oil immersion objective, with numerical aperture NA = 1.4, 5× objective with NA = 0.16, and 20× water immersion objective with NA = 1 were used depending on the scale of observation desired. Low-magnification optical microscopy images were acquired via stereoscope (WILD M3C, Leica, Germany) with 6.4× objective to enable individual particle tracking in capsule dispersions at room temperature. ImageJ software was utilized to quantify the fluorescence intensity inside and outside of the capsule<sup>36</sup>. Scanning electron microscope (SEM) images of the samples were taken on an FEI Nova Nano SEM 230 FE-SEM at an accelerating voltage of 5.0 kV.

**Fourier transform infrared spectroscopy (FTIR):** FTIR patterns were collected on Bruker IFS66/S High End FT-NIR/IR Spectrometer from 400 cm<sup>-1</sup> to 4000 cm<sup>-1</sup>.

**Capsule deformation:** Micropipette manipulation was used to apply controlled deformation to individual capsules. A microcapillary with a right-angle bend held the capsule in place while a second blunt microcapillary with an outer diameter of 1 mm was moved toward the capsule at a constant speed using a syringe pump stepper motor (Aladdin, WPI). The process was imaged at 200 frames per second using an Opticam CMOS camera (Qimaging).

**Dissolved oxygen:** Dissolved oxygen measurements were performed using a dissolved oxygen meter (Oakton DO 6+) to quantify propulsion reaction kinetics for both hydrophobic (ZIFL) and hydrophilic (ZIF90) motors in the presence of 1% v/v H<sub>2</sub>O<sub>2</sub>.

## 2.3 Results and discussion

### 2.3.1 Capsule characterization

Cellulose capsules are created using aqueous emulsion droplets of *Acetobacter* bacteria culture as templates. The bacteria produce an entangled shell of cellulose fibers with micron-scale length and nanometer-scale thickness, Figure 2.1. The overall capsule diameter is millimeter-sized like the emulsion droplet templates used to grow them<sup>27</sup>. While large capsules are easy to make, the lower size limit is set by the size of a small droplet of bacterial culture. Since bacteria are on the order of 3  $\mu\text{m}$  long, the smallest capsules we can make tend to be several times larger  $\sim 20 \mu\text{m}$ <sup>27</sup>.

The use of the cellulose scaffolding provides a balance of structural integrity and flexibility with a significant cargo volume. For example, a 0.5 mm diameter capsule with a 20  $\mu\text{m}$  shell thickness has a mass of only 200 ng because of its high porosity, but its internal volume holds 400,000 times more water mass. The capsules are modified to enable fuel-driven motion by attaching to the fibers a large number of active MOF nanoparticles that contain catalase enzyme in their pores<sup>28</sup>. The MOF particles created here are a crystalline matrix of zinc ions connected by two different organic ligands that allow us to produce motors coated with hydrophilic ZIF90 MOFs, using imidazolate-2-carboxyaldehyde ligand, and a version coated with hydrophobic ZIFL MOFs, using 2-methylimidazole ligands, Figure 2.1. The 60 kDa catalase we used has a hydrodynamic diameter of  $\sim 7.4 \text{ nm}$  and is encapsulated within the porous structure of the larger polycrystalline MOF nanoparticles that precipitate on the cellulose. The process of coating cellulose nanofibers with MOF particles is shown schematically in Figure 2.1. First, positively charged zinc ions are adsorbed on the cellulose hydroxyl surface group. After adding organic ligands,

micron-scale MOF particles crystallize on the 60 nm cellulose fibers, altering the capsule porosity and mechanical properties. The two MOF structures used have the same zinc metal ion basis but are connected by two different hydrophilic and hydrophobic ligands to vary the particles' surface chemistry and swimming behavior.

FTIR was used to assess the success of MOF and enzyme coating on the capsules by measuring the presence of the ligand and enzyme chemical groups, Figure 2.2. For ZIFL, the characteristic peaks at 1585, 1147, ~750 (double bonds) and 423  $\text{cm}^{-1}$  correspond to the stretching vibration of C=N, bending vibration of CH, bending vibration of the imidazole ring and vibration peak of Zn-N, respectively. The presence of these peaks indicates the significant presence of the 2-methylimidazole ligands in the ZIFL. The absorbance spectrum of ZIF90, shown in Figure 2.2a), has a prominent mode centred at 1671  $\text{cm}^{-1}$ , extending from 1751 to 1551  $\text{cm}^{-1}$ , that is attributed to a C=O stretch<sup>37</sup> in the imidazolate-2-carboxyaldehyde ligand structure. The position and intensity of this carbonyl band obscures the amide I and, partially, the amide II spectral features of the catalase. Figure 2.2(a) shows the amide II spectral region with two peaks centered at about 1540 and 1515  $\text{cm}^{-1}$ . The position of these bands is consistent with the amide II components of free catalase, showing its successful encapsulation in the MOF particles on the cellulose fibers<sup>24</sup>. Despite the lower sensitivity of amide II to protein secondary structure versus amide I, we conclude that the secondary structure of catalase-ZIF90 is comparable to catalase-ZIFL<sup>24</sup>. Structural studies of the crystalline MOFs formed on the capsules using XRD measurement showed identical diffraction patterns for both ZIFL and ZIF90 after enzyme encapsulation and attachment to the cellulose capsule, Figure A1.

Figure 2.2(b) shows an SEM image of native cellulose nanofibers in a capsule. The original cellulose fibers in the pristine capsules are quite strong and thin, but

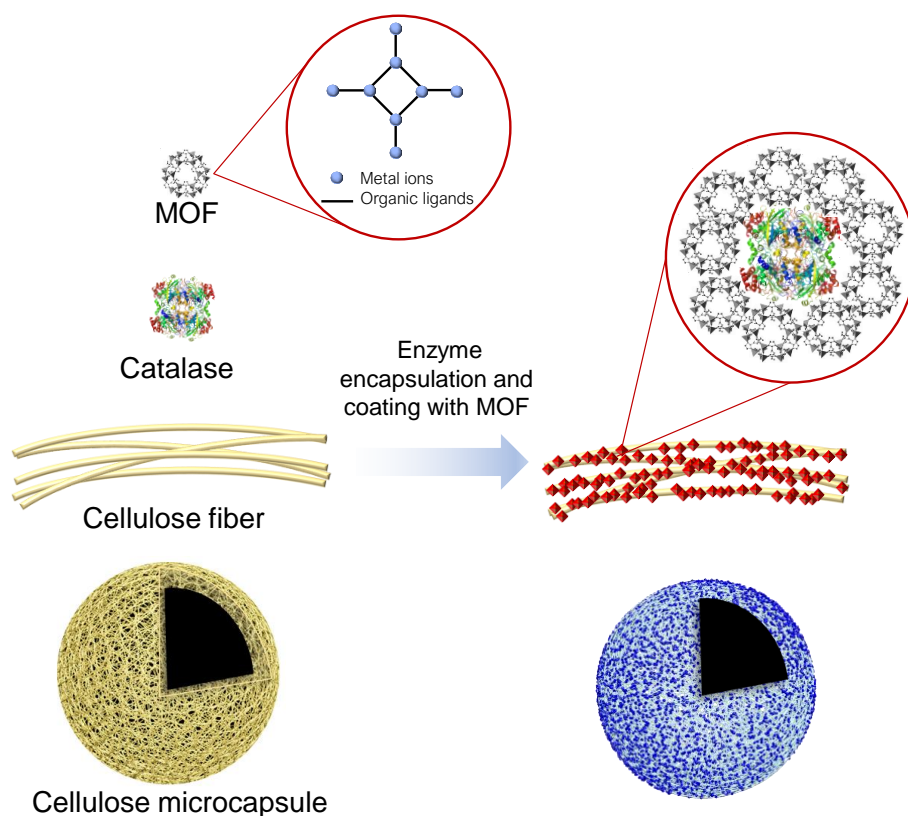


**Figure 2.1:** Schematic illustration of the components of the millimotors and the process for coating the bacterial cellulose capsule with MOFs that contain catalase. The MOFs exist in the form of crystalline nanoparticles with a cage-like structure made of metal ions connected via organic ligands. Each crystal can encapsulate one or multiple biomolecules by physical adsorption<sup>38–40</sup>. The *in situ* growth of MOF crystals on cellulose fibers occurs by adsorption of the positively charged metal ions onto the cellulose hydroxyl group through electrostatic interaction. Subsequent addition of organic ligands enables co-precipitation with the metal ions to form MOF crystals on the fibers<sup>31</sup>

the deposition of metallic MOF nanoparticle networks onto these fibers will modify them in a number of ways, including their mechanical properties and the overall capsule permeability to the fluid environment. The patterns of deposition will also affect the mode of propulsion by catalysis, so we characterize their state by imaging. Figures 2.2(c-f) show crystals of ZIFL and ZIF90 deposits on the capsule fibers. The capsules were freeze-dried at  $-65^{\circ}\text{C}$  to avoid any collapse that might occur by capillary pressure during air drying. As shown in Figure 2.2, the fiber diameter is between 20-70 nm with a length of several microns for the unmodified cellulose capsule<sup>27</sup>. After crystallization of MOF on the capsules, particles with an average size of 100 – 150 nm for ZIFL and 150 nm for ZIF90 attached to the surface of the cellulose fibers, Figure 2.2(c-d). The addition of the MOF particles to the capsule is expected to alter the mass and inertia of the system during subsequent propulsion studies. If we assume the MOF coating is a 99% dense single layer of 100 nm particles with a density of  $2\text{ g/cm}^3$ , the particles add 150 ng mass to a 0.5 mm diameter cellulose capsule, at most doubling its weight while still being dominated by the mass of the liquid cargo in its capsule.

Differences can be seen in the coating morphology at higher magnifications, Figure 2.2(e-f), based on the polarity of the MOF particles produced. For example, the hydrophobic ZIFL particles form structures that partially span the gaps between fibers Figure 2.2(e), likely because the particles have less affinity for the hydrophilic cellulose. The hydrophilic ZIF90 coatings seem to follow the fiber structures more closely due to more intimate contact, Figure 2.2(f). Although different morphologies form on the capsules, MOF film growth on individual fibers increases the effective fiber size and reduce the pore size of the overall capsule. Previous measurements<sup>27</sup> indicated the pristine capsules have pore sizes on the order of 500 nm so the MOF crystals will rapidly reduce the overall capsule permeability as they grow.

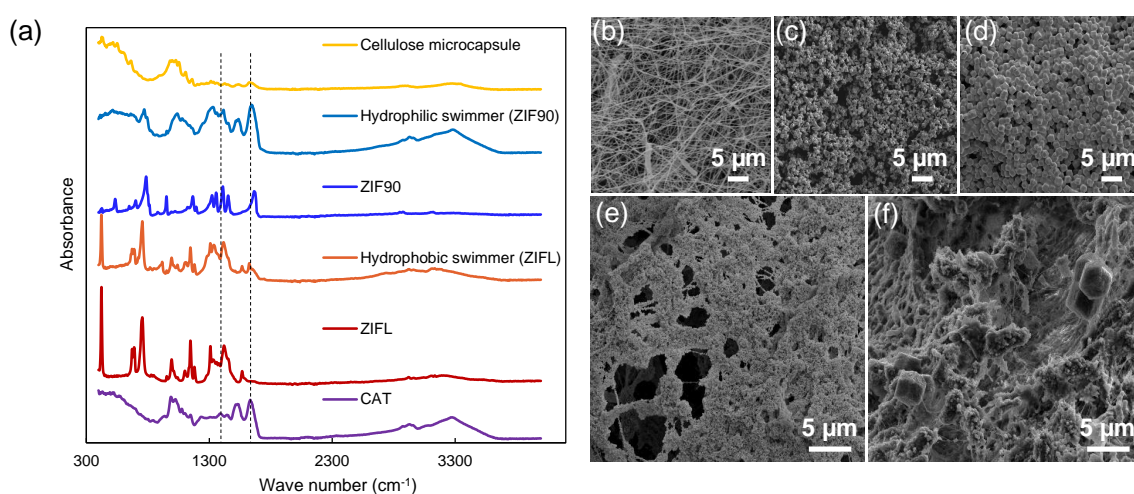


**Figure 2.2:** (a) FTIR spectra of pure catalase (CAT), both MOF types, pristine cellulose capsules, and cellulose capsules after MOF coating. IR peaks show successful combination of enzyme, MOF, and cellulose fibers. (b) SEM of pristine cellulose capsule surfaces, (c) hydrophilic ZIF90 MOF particles, (d) hydrophobic ZIFL MOF particles. (e and f) Higher magnification views of cellulose fibers coated with MOF particles, highlighting the reinforcement of the cellulose capsule fibers by the dense deposits as well as some reduction in pore size. The MOF particle coatings on cellulose fibers tend to form pore-spanning bridges for (e) hydrophobic ZIFL MOF while deposits tend to follow the fiber structure more for (f) hydrophilic ZIF90 MOF. All scale bars 5 μm.

Different microscopy techniques were used to visualize the pristine and modified cellulose capsule at larger length scales for a more holistic characterization. Light sheet fluorescence microscopy (LSFM) allows us to visualize the full 3D structure of the millimotors. Cellulose, MOFs, and catalase were stained with Congo Red, FITC, and Rhodamine B, respectively, before fluorescent imaging. Figures 2.3(a-c) show 3D reconstructions of pristine and modified cellulose capsules coated by both MOF types, with the cellulose fibers shown in red. At this magnification, the pristine capsule in Figure 2.3(a) looks spherical and almost solid as the capsule pores are micron-scale<sup>27</sup>. A capsule with the hydrophilic ZIF90 MOF coating is shown in Figure 2.3(b) and the impact of the MOF coating is clearest in the dark regions of the spherical capsule where larger MOF regions obscure the cellulose fibers. The coating is heterogeneous due to random variations in the solution during precipitation. More detail can be resolved at higher magnifications.

Higher resolution imaging is performed using confocal microscopy to visualize the hollow and fibrous structure of the capsules, with and without a MOF coating, Figures 2.3(d-i). Figures 2.3(d-f) show a single mid-plane slice through the capsule, demonstrating that the capsules are largely hollow, and have a shell on the order of 20  $\mu\text{m}$  in agreement with past work<sup>27</sup>. The capsules with hydrophilic ZIF90 and hydrophobic ZIFL MOF coatings in Figures 2.3(e-f) have similar shell thicknesses to the pristine capsule in Figure 2.3(d), as the nanoscale MOF coatings coat individual fibers and don't significantly change the overall wall thickness. An even higher magnification view of the capsule shells highlights the degree of penetration of the fiber structures by the MOF particles being deposited, Figures 2.3(g-i). Here the MOF nanoparticles are shown as yellow and the cellulose fibers as red. The optical resolution of the confocal system used here is on the order of 200 nm so these images will not resolve the smallest deposits formed and only indicate the degree of

individual fiber coating by the MOFs. As the MOF particles are the framework we use to encapsulate the catalase enzyme for propulsion, the distribution of both is of interest to particle design and motor performance.

Enzyme distribution is a key parameter determining millimotor motion and orientation<sup>41</sup>. The distribution of enzyme on the MOF-coated capsules is demonstrated in Figures 2.3(j-k) using a 3D reconstruction of the millimotor capsules with a color map indicating the intensity of the Rhodamine B dye labeling the catalase. We observe a heterogeneous but thorough distribution of the enzyme on the surface of the hydrophobic motor, Figure 2.3(j), but an asymmetric distribution along the top half of the surface of the hydrophilic millimotor, possibly because of a higher affinity of the enzyme for the hydrophobic MOFs, causing some segregation on the hydrophilic system<sup>42</sup>. A bulk-scale measurement of enzyme availability, a Bradford assay<sup>43</sup>, was also used to calculate the encapsulation efficiency of catalase as 98.2% for hydrophobic ZIFL and 85.9% in hydrophilic ZIF90 motors. The difference in spatial distribution of the enzyme on the capsules could potentially affect self-propulsion of the motors by inhomogeneous oxygen bubble production<sup>41,44</sup> but for buoyancy-dominated motion such an effect should be negligible. The MOF coatings on the capsules can also affect porosity of the capsules, so we now assess modified capsule exchange with the fluid environment.

### 2.3.2 Porosity of motors

Song et al.<sup>27</sup> studied the permeability of pristine cellulose capsules and found a pore size on the order of 500 nm. After surface modification of the capsules by MOF deposition, Figure 2.3, we expect the pore size to change significantly so we study this by molecular tracer diffusion experiments. FITC-labeled dextran chains ranging from 4-40 kDa were used as tracers to determine the permeability of MOF-coated

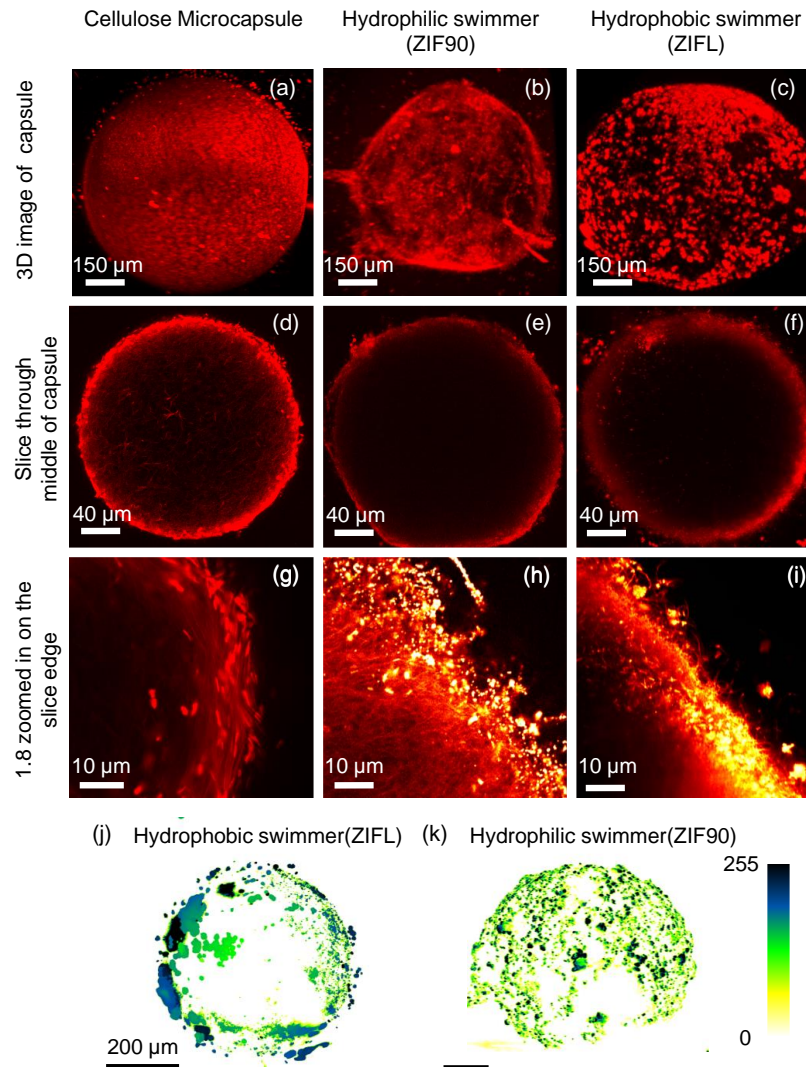


**Figure 2.3:** Lightsheet fluorescence microscopy shows 3D reconstructions of the (a) pristine cellulose capsule, (b) a capsule coated with hydrophilic ZIF90, and (c) hydrophobic ZIFL MOFs. A single mid-plane slice through the capsule (d) before and after coating with (e) hydrophilic and (f) hydrophobic MOF (g-i) Higher magnification confocal images of native cellulose fiber (g) and after coating with hydrophilic (h) and hydrophobic (i) MOF, show MOF particles in yellow and cellulose fibers in red. 3D images of enzyme distribution on the (j) hydrophobic and (k) hydrophilic millimotor surface. Color bar represents the fluorescent intensity of labeled enzyme.

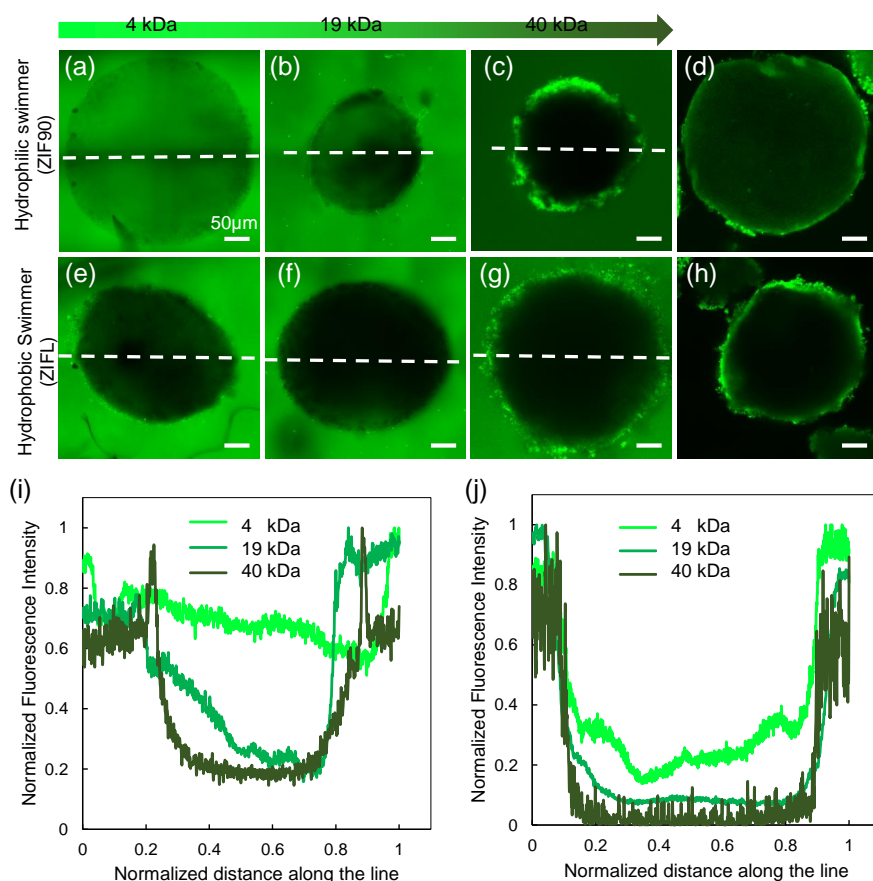


**Figure 2.4:** Measurement of permeability of (a-c) hydrophilic and (e-g) hydrophobic millimotors based on transport of three different FITC-dextran tracers with molecular weight ranging from 4-40 kDa. Figures (d) and (h) show capsules that contained 40 kDa dextran before being coated with MOFs to demonstrate their encapsulation ability. The FITC-dextran concentration varies from green regions of high concentrations to black where no FITC-dextran is resolved. Scale bars are 50  $\mu\text{m}$ . The fluorescence intensity in (a-g) is summarized by plotting integrated normalized intensity of the images for the (i) hydrophilic ZIF90 and (j) hydrophobic millimotors.

cellulose capsules based on size exclusion. After mixing capsules with 1 mg/mL of FITC-dextran and 24 hr incubation, confocal microscopy images of capsules were obtained to determine the ability of different sizes to penetrate the coated capsules. Figures 2.4(a-c) show capsules that have been exposed to different size FITC-dextran and the intensity of green tracer that was able to diffuse inside of the capsules coated with hydrophilic ZIF90 provides a measure of the new capsule pore size. The 4 and 19 kDa tracers penetrate the hydrophilic ZIF90 capsules in Figures 2.4(a-b), indicating a pore size larger than 1.9 nm, while the 40 kDa remains outside of the capsule, Figure 2.4(c), blocked by the new pore size and indicating the hydrophilic capsule is impermeable to 4.3 nm species<sup>45</sup>. Ten different sets of capsules were tested for reproducibility and the same results were obtained as above.

For hydrophobic ZIFL coated capsules, 4 kDa FITC-dextran shows a small amount of diffusion inside the capsule after 24 h. However, 19 and 40 kDa molecular weight FITC-dextran chains are totally excluded. These capsule pores must then have an average diameter less than 1.9 nm<sup>45</sup>. A second experiment was performed to confirm the upper limit of pore size of both capsule types: we immersed capsules in 40 kDa FITC-dextran and *then* coated them with hydrophilic and hydrophobic MOFs. After washing the capsules with deionized water multiple times, and holding for 24 h, we saw no release of FITC-dextran from either hydrophilic or hydrophobic capsules, Figures 2.4(d) and (h), respectively. Different reaction times and conditions could alter these effects, but the results in Figure 2.4 indicate a more than 100X variation in pore size (from 500 nm to 4 nm), is possible for MOF-coated cellulose capsules. For comparison, plant cells have a cellulose structure that is permeable to molecules with a diameter ranging from 3.5 – 5.2 nm<sup>46</sup>. MOF coating of capsule fibers enables us to create motors with chemical propulsion as well as tunable permeability and solute exchange.

Because the dextran is shown to be uniformly blocked by the coating, it indicates a fairly uniform coating, on average, by the crystals given the deposition occurs throughout the thickness of the capsule walls. So the capsules remain permeable after coating, though much less so than their more permeable pristine form, meaning they can fill with fluid and carry that cargo during movement. It also means the coated capsule millimotors can still exchange contents with the environment via molecular diffusion, for example to perform delivery of a chemical cargo<sup>18</sup>. The length scale of the pores can then be used to control the subsequent selectivity of the capsule in these applications.

### 2.3.3 Millimotor capsule propulsion

Oxygen gas production and bubble formation play an essential role in propulsion of both hydrophobic and hydrophilic millimotors. When exposed to an aqueous hydrogen peroxide solution, catalase enzyme immobilized in the MOFs catalyzes hydrogen peroxide decomposition into oxygen and water molecules, with the excess oxygen gas forming bubbles and driving motion. We first assess the rate of reactive oxygen generation<sup>28,42,47</sup> in a bulk solution of 1% v/v H<sub>2</sub>O<sub>2</sub> containing hydrophobic ZIFL and hydrophilic ZIF90 motors, Figure 2.5(a). Both systems rapidly produce oxygen, but the rate of O<sub>2</sub> production by hydrophilic ZIF90 motors was more than six times that by hydrophobic ZIFL motors, Figure 2.5(a), as a result of differences in enzyme activity. The catalase enzyme has a higher affinity for a hydrophobic surface, which can cause conformation changes that denature the protein, reducing its activity<sup>42</sup>. Oxygen production rate is important to motor performance, as sufficiently high rates can lead to bubble ejection and propulsion by recoil forces, whereas slower growth tends to favor bubbles remaining attached to a motor so that motion is dominated by buoyancy. The mode of bubble-motor interaction,

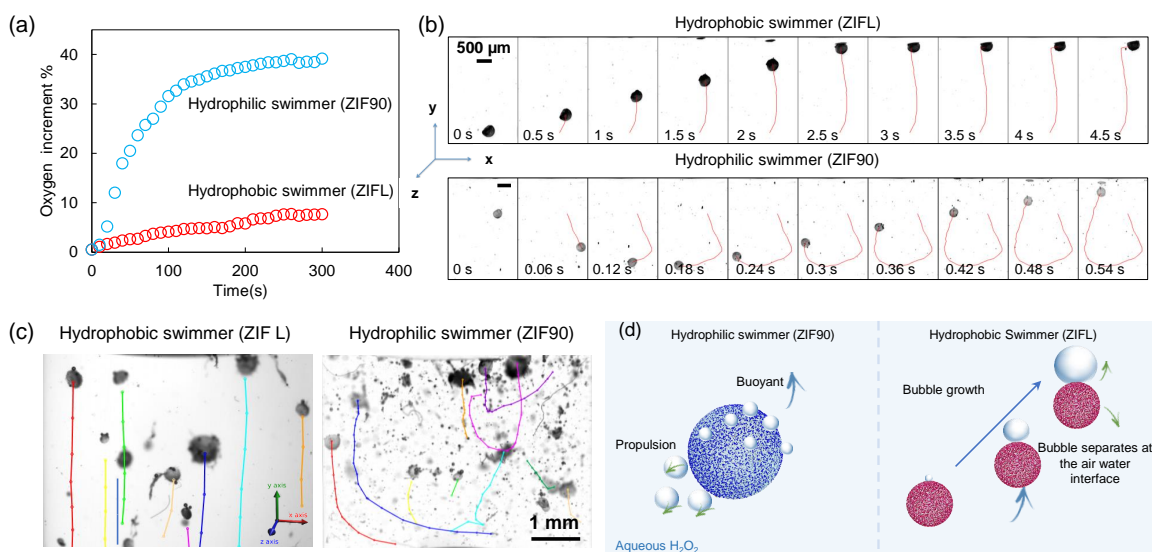


**Figure 2.5:** (a) Oxygen gas increment measurements in an aqueous 1% hydrogen peroxide solution containing dispersed hydrophilic or hydrophobic millimotors. (b) Time-lapse images of hydrophobic ZIFL (first row) and hydrophilic ZIF90 (second row) motor trajectories in aqueous 0.25 wt%  $H_2O_2$ . For hydrophobic motors, higher MOF deposition makes the motors denser so they sediment to the bottom. Bubble formation and growth then lifts motors vertically via buoyancy. For hydrophilic motors, both bubble propulsion and buoyancy contribute to motion, initially driving motors in erratic directions then mostly vertically. (c) Multiple hydrophilic and hydrophobic motors have similar traits, moving vertically when buoyancy dominates and in multiple directions when both buoyancy and propulsive recoil contribute. (d) Schematic of the proposed mechanism for millimotor bubble formation and movement: hydrophobic motors remain attached to  $O_2$  bubbles and their motion is dominated by buoyancy, while hydrophilic motors have elements of horizontal motion due to propulsion by bubble ejection as well as buoyancy.

however, is also affected by the motor surface chemistry and the resultant affinity of hydrophobic bubbles for a motor.

We studied the performance of these motors by observation of an aqueous dispersion of individual or multiple enzyme-powered millimotors. The motors were placed in a transparent cuvette and allowed to sediment, then different concentrations of aqueous hydrogen peroxide solution ranging from 0.065 - 1% were added and allowed to diffuse to the motors at the bottom to initiate propulsion. Once peroxide decomposition began, cellulose millimotors became buoyant and migrated from a resting position at the bottom of the cuvette to the rest of the fluid volume. A high-speed camera was utilized to observe growth of single and multiple oxygen bubbles inside or outside of the motors in less than a minute after addition of hydrogen peroxide.

In all motion studies, we see a clear difference between the hydrophilic ZIF90 motors, that initially move in various directions as a result of rapid bubble production and ejection, and the hydrophobic ZIFL motors that only move vertically, Figure 2.5(b). For example, the hydrophobic ZIFL motor in the top row of Figure 2.5(b) follows a completely vertical trajectory over several seconds until it reaches the top of the water volume and drifts slightly to the side. This is consistent with extensive work on mineral flotation, where hydrophobic particles are separated from suspensions using air bubbles that flow through the system<sup>48,49</sup>. The hydrophilic ZIF90 motor in the bottom row of Figure 2.5(b), however, initially moves down as a result of ejecting a bubble upward, then makes a hard turn to our left and moves across the bottom of the cuvette. After these two major direction changes, the motor then moves up as buoyancy becomes dominant. Multiple millimotors in dispersion behave similarly, as shown in Figure 2.5(c) for a 0.05 wt% solution of hydrogen peroxide. The hydrophobic ZIFL motors all follow remarkably consistent vertical

trajectories as their motion is dominated by buoyancy due to growth of strongly attached bubbles, Figure A2. The hydrophilic ZIF90 motors, however, show more complex motion that can lead to correlated trajectories, like the two motors in the bottom left corner of the image, but opposing directions are also possible as seen in the upper right region of the image. The enzymatic activity is maintained until the exhaustion of the chemical fuel, so adjusting the concentration increases the initial rates of movement and extends the length of time that movement can be observed. The two motor surface chemistries thus enable different directions of movement. Bubbles can be generated wherever enzymes are located on the surface of the motors, so if the bubble is initially ejected the motor will move in the opposite direction by recoil. If bubbles remain attached, however, the motor will move up by buoyancy and its initial orientation is less significant to the subsequent motion. We summarize the mechanisms of motion by schematic in Figure 2.5(d).

The cellulose capsules used here vary in size from 200 – 600  $\mu\text{m}$ , all much larger than commonly studied micro- and nanomotors, but consistent with recently developed protocell millimotors<sup>18</sup>. We are curious about the performance of these motors versus their smaller counterparts, however, as their large size but low solid mass could provide additional benefits. As noted earlier, the capsules are low-density and permeable, with the majority of their inertia due to water that permeates the interior. A useful benchmark is the motor velocity relative to its diameter, where impressive values of 4-200 diameters/second are known<sup>4</sup>. Here we see hydrophobic ZIFL millimotors regularly moving at average velocities of up to 4 mm/s, with a standard error of 0.6 mm/s. This represents a relative velocity of more than 8 diameters/second. Hydrophilic ZIF90 millimotors can reach average velocities of 40 mm/s, with a standard error of 14 mm/s, Figure A3. This represents a relative velocity of more than 80 diameters/second. The difference is the result of the recoil

force exhibited by only the hydrophilic ZIF90 motors, as buoyancy is the only other mechanism possible for both systems. Given that these motors are orders of magnitude larger than micro- or nanomotors, it is encouraging to note their propulsion, even while containing a massive liquid cargo, is competitive with the much smaller solid motors.

### 2.3.4 Motor deformation and confinement response

The cellulose motors have a unique porosity and response to mechanical stress because of their combined strength and flexibility<sup>27</sup>. As a result, we are interested in how these particles affect capsule response to extensional stress. First, we need to evaluate the extent to which the modification of the motors by the formation of MOF crystals affects their mechanical properties. Song et al.<sup>27</sup> found unmodified capsules deformed elastically under compression, recovering after deformations as large as 20% but remaining indented or buckled at higher strains. Adding crystalline MOF particles, however, is expected to stiffen the fibers and change the capsule response to deformation. Stress-strain curves for up to five individual millimotors, Figure A4, were measured using an extensional flow in a microfluidic channel<sup>27</sup>. We found that the elastic modulus,  $E = 100$  Pa, of pristine cellulose capsules increased  $\sim 30X$  after coating with hydrophilic ZIF90 MOFs and  $\sim 140X$  after coating with hydrophobic ZIFL MOFs. The difference is likely a result of variations in coating uniformity and distribution, Figure 2.2. Because of the small sample size we have available for testing, the mechanical measurements can not be taken to be fully representative of all our particles and are indicative only of the likely magnitude of the capsule moduli.

Along with an increased elastic modulus, the capsules preserve significant ability to recover from deformation, as we demonstrate in Figure 2.6. Figure 2.6(a)

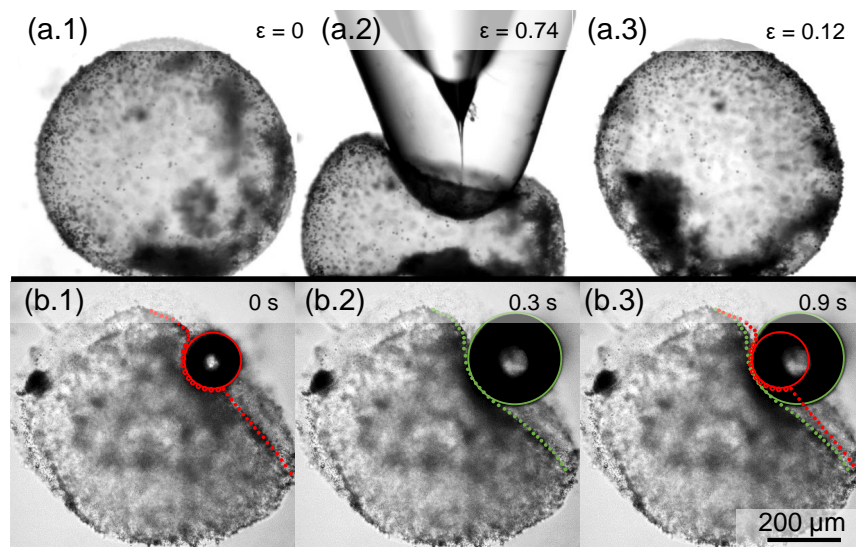


**Figure 2.6:** Deformation and recovery of hydrophobic (a1-a3) motors using microcapillary manipulation. The capsule was deformed by a capillary tip, and each column indicates the stage of initial, deformation, and recovery. The spherical shape of the hydrophobic motor is recovered after 75% strain. (b1-b3) Successive images show the growth of an oxygen bubble on the surface of a hydrophobic ZIFL capsule over 5 millisecond intervals. The capsule deforms under the stress exerted by the bubble, indicating an ability to change shape during movement as the drawn lines document.

shows the microscopic response of a hydrophobic ZIFL millimotor to deformation by a blunt microcapillary end. Both hydrophobic ZIFL and hydrophilic ZIF90 motors largely recover their original profile after being indented by external stress to a strain of  $\varepsilon = 74\%$  and higher, while pristine capsules do not fully recover from strains higher than  $\varepsilon = 20\%$ <sup>27</sup>. The addition of MOFs clearly increases the elasticity of the capsules while adding propulsive capability. This is consistent with above estimates of a significantly increased capsule modulus after MOF coating.

Figure 2.6(b) suggests an even more interesting dimension to the flexibility of these motors. A series of successive close-up images of a bubble evolving on a hydrophobic ZIFL motor surface in Figure 2.6(b) indicates that the motor structure actually flexes in response to the pressure of the bubble expansion itself. Here the bubble is likely generated inside of the capsule and then squeezes out of a pore to exert the pressure seen here. Such an effect could also occur if the bubble formed on a capsule that was confined in some way. The result indicates the motors could actually be changing shape during motion, increasing their flexibility and responsiveness, and offering a mechanism for more complex movements in future work. As pointed out earlier, there is a need for motors to navigate confined environments while adapting and recovering to the different conditions they encounter. We now evaluate whether such deformation and response can occur when the millimotors encounter confinement during their propelled movement. We do this by studying the performance of the motors during propulsion in a constricted channel and note whether the combination of propulsion and flexibility enhance their mobility. The force exerted by the bubble on the microcapsule as it emerges will be a function of its curvature and the surface tension in the liquid. Because there is not a significant amount of surface-active material present, we expect the surface tension to be on the order of 70 mN/m, with the capillary pressure scaling inversely with bubble

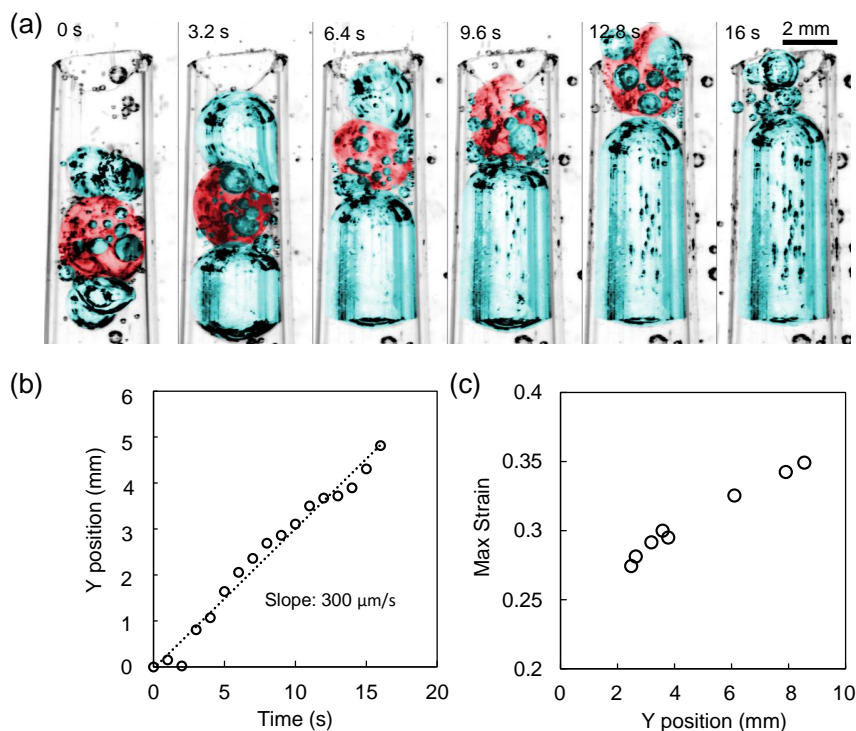


**Figure 2.7:** (a) Composite images of the hydrophilic motor passing through a constriction in an aqueous solution of 3% H<sub>2</sub>O<sub>2</sub>. False color is used to highlight the motor in red, oxygen bubble in blue, and glass capillary in grey. (b) The slope of the vertical position and time plot shows the velocity of the hydrophilic motor, around 300 μm/s, during its motion through the confined channel. (c) Changing hydrophilic motor strain at different vertical positions in the constriction.

radius. Presumably at lower surface tensions the bubble will still merge but may deform the capsule less when doing so.

Figure 2.7(a) shows a series of images of a hydrophilic ZIF90 motor as it moves vertically through a gradually constricting capillary. Here, to enhance visibility of the position of the motor in the image frames, we have false colored the motor red, water blue, and the glass capillary grey. The spherical millimotor initially has a diameter of 2.9 mm so can enter the capillary but must compress in order to exit, as the capillary internal diameter reduces from 3.5 mm to 2.2 mm at its outlet. The motor is initially driven by buoyancy but slows in the second frame in response to

the narrowed passage. The narrowing of the channel causes compression of the motor, increasing its strain to more than 25%, Figure 2.7(c). However, the motor continues to produce bubbles behind itself that grow as the reaction proceeds. A solid particle at this point would be unable to proceed and simply block the channel, but the flexible motor is able to deform much more in response to stress, Figure 2.6(a), and continues to move, albeit in a more cyclical way as seen in the plot of vertical position in Figure 2.7(b). Despite the small variations in velocity, the overall progress of the motor is relatively constant as a result of its flexibility and reactive propulsion. The growth of surface bubbles likely aids movement by reducing drag on the capsule. Figure 2.7(a) also shows the formation of a large bubble behind the motor that aids in pushing it through the constriction. Interestingly, the bubble driving the capsules through the capillary is pinned to the capillary wall, allowing it to push against the capsule. Such behavior is beneficial for this additional propulsion mechanism to act, as a non-wetting capillary surface would reduce the ability of the bubble to push the motor. The results in Figure 2.7 show that the production of deformable responsive motors with the low-density cellulose capsules developed here enable use in confined environments that solid particle counterparts can not handle. A high level of deformation might be expected to cause erosion of the MOFs from the capsules surface; however, no detectable fragments or associated turbidity were observed following the deformation experiments in Figure 2.6(a). In addition, the results in Figure 2.7 indicate propulsion is maintained even during quite robust deformation in confinement, further confirming the motors largely remain attached.

## 2.4 Conclusions

In this study, enzyme-powered millimotors have been made by crystallization of MOF particles encapsulating catalase enzymes onto soft cellulose capsules. The large size, but low mass of the motors makes them a unique addition to the range of existing particle motors as they are able to carry significant volumes of liquid cargo because of their permeability. The large capsules are able to move using chemical fuel thanks to the numerous nanomotors attached to their surfaces, analogous to a large tanker ship driven by multiple tugboats.

Two mechanisms of propulsion result from enzyme-mediated production of oxygen gas bubbles in the presence of hydrogen peroxide. Bubbles grow on and remain attached to hydrophobic motors, driving vertical motion as buoyancy rapidly grows. For hydrophilic motors, bubbles are initially expelled from the structures, driving randomly-directed motion by recoil force, but as more bubbles grow motion becomes dominated by buoyancy and the motors rise similarly to the hydrophobic motors. Despite their large size, the millimotors move with surprising speeds, reaching levels of 80 motor diameters per second for the hydrophilic motors, when recoil force dominates movement, and 8 motor diameters per second when buoyancy dominates. The low density of the millimotors makes them highly efficient at movement, exhibiting similar or faster relative velocities than much smaller solid particle motors. The flexible response to mechanical stress of the millimotors enables them to squeeze through significant constrictions, making their mobility viable even in confined spaces and environments where solid motor particles would clog and jam. The millimotors can compress their diameter by as much as 30% in a constriction and their continuous generation of gas bubbles creates a low-slip surface layer and a back-pressure that enhances movement through tight spots.

Such flexibility also offers a possible way to rapidly release the liquid cargo of the capsules and we plan to study this, and the movement of capsules through more complex porous media, in future work.

## References

- [1] J. L. Moran, J. D. Posner, *Annual Review of Fluid Mechanics* **2017**, *49*, 511–540.
- [2] E. Ma, K. Wang, Z. Hu, H. Wang, *Journal of Colloid and Interface Science* **2021**, *603*, 685–694.
- [3] Y. Tao, X. Li, Z. Wu, C. Chen, K. Tan, M. Wan, M. Zhou, C. Mao, *Journal of Colloid and Interface Science* **2022**, *611*, 61–70.
- [4] W. Gao, S. Sattayasamitsathit, J. Wang, *The Chemical Record* **2012**, *12*, 224–231.
- [5] M. Yan, L. Xie, J. Tang, K. Liang, Y. Mei, B. Kong, *Chemistry of Materials* **2021**, *33*, 3022–3046.
- [6] H. Wang, J. G. S. Moo, M. Pumera, *ACS Nano* **2016**, *10*, 5041–5050.
- [7] S. Tang, F. Zhang, H. Gong, F. Wei, J. Zhuang, E. Karshalev, B. E.-F. de Ávila, C. Huang, Z. Zhou, Z. Li *et al.*, *Science Robotics* **2020**, *5*, year.
- [8] B. Esteban-Fernández de Ávila, M. A. Lopez-Ramirez, R. Mundaca-Uribe, X. Wei, D. E. Ramírez-Herrera, E. Karshalev, B. Nguyen, R. H. Fang, L. Zhang, J. Wang, *Advanced Materials* **2020**, *32*, 2000091.
- [9] S. Gao, J. Hou, J. Zeng, J. J. Richardson, Z. Gu, X. Gao, D. Li, M. Gao, D.-W. Wang, P. Chen *et al.*, *Advanced Functional Materials* **2019**, *29*, 1808900.
- [10] M. Zarei, M. Zarei, *Small* **2018**, *14*, 1800912.
- [11] B. Qiu, L. Xie, J. Zeng, T. Liu, M. Yan, S. Zhou, Q. Liang, J. Tang, K. Liang, B. Kong, *Advanced Functional Materials* **2021**, *31*, 2010694.
- [12] C. Li, Y. Yu, L. Wang, S. Zhang, J. Liu, J. Zhang, A.-B. Xu, Z. Wu, J. Tong, S. Wang *et al.*, *Chemistry of Materials* **2019**, *31*, 9513–9521.

- 
- [13] J. Liu, J. Li, G. Wang, W. Yang, J. Yang, Y. Liu, *Journal of Colloid and Interface Science* **2019**, 555, 234–244.
- [14] H. Ye, Y. Wang, X. Liu, D. Xu, H. Yuan, H. Sun, S. Wang, X. Ma, *Journal of Colloid and Interface Science* **2021**, 588, 510–521.
- [15] H. R. Vutukuri, M. Lisicki, E. Lauga, J. Vermant, *Nature Communications* **2020**, 11, 1–9.
- [16] S. Yuan, X. Lin, Q. He, *Journal of Colloid and Interface Science* **2022**, 612, 43–56.
- [17] M. C. Marchetti, J. F. Joanny, S. Ramaswamy, T. B. Liverpool, J. Prost, M. Rao, R. A. Simha, *Reviews of Modern Physics* **2013**, 85, 1143–1189.
- [18] B. P. Kumar, A. J. Patil, S. Mann, *Nature Chemistry* **2018**, 10, 1154–1163.
- [19] F. Peng, Y. Men, Y. Tu, Y. Chen, D. A. Wilson, *Advanced Functional Materials* **2018**, 28, 1706117.
- [20] Z. Xiao, M. Wei, W. Wang, *ACS Applied Materials & Interfaces* **2018**, 11, 6667–6684.
- [21] Y. Yang, X. Arqué, T. Patiño, V. Guillerm, P.-R. Blersch, J. Pérez-Carvajal, I. Imaz, D. Maspoch, S. Sánchez, *Journal of the American Chemical Society* **2020**.
- [22] A. Terzopoulou, J. D. Nicholas, X.-Z. Chen, B. J. Nelson, S. Pané, J. Puigmartí-Luis, *Chemical Reviews* **2020**, 120, 11175–11193.
- [23] S. Sanchez, A. A. Solovev, Y. Mei, O. G. Schmidt, *Journal of the American Chemical Society* **2010**, 132, 13144–13145.
- [24] L. Zhu, L. Zong, X. Wu, M. Li, H. Wang, J. You, C. Li, *ACS Nano* **2018**, 12, 4462–4468.
- [25] H. Ning, Y. Zhang, H. Zhu, A. Ingham, G. Huang, Y. Mei, A. A. Solovev, *Micromachines* **2018**, 9, 75.
- [26] D. A. Edwards, J. Hanes, G. Caponetti, J. Hrkach, A. Ben-Jebria, M. L. Eskew, J. Mintzes, D. Deaver, N. Lotan, R. Langer, *Science* **1997**, 276, 1868–1872.

## References

---

- [27] J. Song, F. Babayekhorasani, P. T. Spicer, *Biomacromolecules* **2019**, *20*, 4437–4446.
- [28] Z. Guo, T. Wang, A. Rawal, J. Hou, Z. Cao, H. Zhang, J. Xu, Z. Gu, V. Chen, K. Liang, *Materials Today* **2019**, *28*, 10–16.
- [29] D. Saidane, E. Perrin, F. Cherhal, F. Guellec, I. Capron, *Philosophical Transactions of the Royal Society A: Mathematical Physical and Engineering Sciences* **2016**, *374*, 20150139.
- [30] D. Lahiri, M. Nag, B. Dutta, A. Dey, T. Sarkar, S. Pati, H. A. Edinur, Z. Abdul Kari, N. H. Mohd Noor, R. R. Ray, *International Journal of Molecular Sciences* **2021**, *22*, 12984.
- [31] X. Ma, Y. Lou, X.-B. Chen, Z. Shi, Y. Xu, *Chemical Engineering Journal* **2019**, *356*, 227–235.
- [32] J. Sun, M. Mathesh, W. Li, D. A. Wilson, *ACS Nano* **2019**, *13*, 10191–10200.
- [33] C. He, K. Lu, W. Lin, *Journal of the American Chemical Society* **2014**, *136*, 12253–12256.
- [34] M. Mohammad, A. Razmjou, K. Liang, M. Asadnia, V. Chen, *ACS Applied Materials & Interfaces* **2018**, *11*, 1807–1820.
- [35] R. M. Macnab, D. E. Koshland, *Proceedings of the National Academy of Sciences* **1972**, *69*, 2509–2512.
- [36] J. Schindelin, I. Arganda-Carreras, E. Frise, V. Kaynig, M. Longair, T. Pietzsch, S. Preibisch, C. Rueden, S. Saalfeld, B. Schmid, J. Y. Tinevez, D. J. White, V. Hartenstein, K. Eliceiri, P. Tomancak, A. Cardona, *Nature Methods* **2012**, *9*, 676–682.
- [37] K.-Y. Lee, J. J. Blaker, A. Bismarck, *Composites Science and Technology* **2009**, *69*, 2724–2733.

- 
- [38] K. Liang, R. Ricco, C. M. Doherty, M. J. Styles, S. Bell, N. Kirby, S. Mudie, D. Haylock, A. J. Hill, C. J. Doonan *et al.*, *Nature Communications* **2015**, *6*, 1–8.
- [39] Y. Chen, V. Lykourinou, C. Vetromile, T. Hoang, L.-J. Ming, R. W. Larsen, S. Ma, *Journal of the American Chemical Society* **2012**, *134*, 13188–13191.
- [40] J. Liang, K. Liang, *Advanced Functional Materials* **2020**, *30*, 2001648.
- [41] T. Patiño, X. Arqué, R. Mestre, L. Palacios, S. Sánchez, *Accounts of Chemical Research* **2018**, *51*, 2662–2671.
- [42] W. Liang, H. Xu, F. Carraro, N. K. Maddigan, Q. Li, S. G. Bell, D. M. Huang, A. Tarzia, M. B. Solomon, H. Amenitsch *et al.*, *Journal of the American Chemical Society* **2019**, *141*, 2348–2355.
- [43] M. M. Bradford, *Analytical Biochemistry* **1976**, *72*, 248–254.
- [44] T. Patiño, N. Feiner-Gracia, X. Arqué, A. Miguel-López, A. Jannasch, T. Stumpp, E. Schäffer, L. Albertazzi, S. Sánchez, *Journal of the American Chemical Society* **2018**, *140*, 7896–7903.
- [45] J. K. Armstrong, R. B. Wenby, H. J. Meiselman, T. C. Fisher, *Biophysical Journal* **2004**, *87*, 4259–4270.
- [46] N. Carpita, D. Sabularse, D. Montezinos, D. P. Delmer, *Science* **1979**, *205*, 1144–1147.
- [47] M. Rabe, D. Verdes, S. Seeger, *Advances in Colloid and Interface Science* **2011**, *162*, 87–106.
- [48] M. Van der Zon, P. Hamersma, E. Poels, A. Bliet, *Catalysis Today* **1999**, *48*, 131–138.
- [49] H. Vinke, P. Hamersma, J. Fortuin, *AIChE Journal* **1991**, *37*, 1801–1809.



## Chapter 3

# Multi-functional responsive nanocellulose-PNIPAM capsules

### 3.1 Introduction

Encapsulation and controlled release from hollow microcapsule particles are widely studied for applications in pharmaceuticals<sup>1</sup>, food<sup>2</sup>, and cosmetics, often drawing inspiration from natural microcapsules like pollen<sup>3-6</sup> and other biological materials. Significant progress has been achieved in developing controlled release based on two main strategies. One, diffusive release, occurs as solute diffuses through the capsule wall and is controlled by capsule permeability and solute diffusivity. The second release mechanism, rupture, is faster and occurs when capsule rupture is triggered by osmotic pressure, shear stresses, or other external stimuli.

Diffusive release has an upper limit of release rate, and adding responsiveness to capsules can only tune the capsule permeability and thus diffusion rate in response to the stimuli<sup>7,8</sup>. Werner et al.<sup>8</sup> developed a responsive microcapsule with rapid and reversible permeability, releasing 4 kDa molecules in 200 s and 10 kDa 10x slower with a rapid response time.

Capsule rupture provides a higher release rate than by passive diffusion but limits capsule reusability<sup>2,9-17</sup>. The release time scale can vary from seconds to minutes depending on microcapsule stiffness and shell thickness<sup>18,19</sup>. Recently, heart-inspired microcapsules have been developed to control the capsule release rate

using compression and relaxation cycles triggered by external field manipulation of embedded magnetic particles to release at a rate of  $2.5 \mu\text{L}/\text{min}^5$ . Manual control over compression and relaxation cycles allows release from capsules without permanent deformation<sup>20-22</sup>. Once released, solutes diffuse through surrounding liquid<sup>7</sup> at rates dependent on solute diffusivity and fluid viscosity<sup>2</sup> for instance free diffusion rate of 4 kDa dextran in water is  $135 \mu\text{m}^2/\text{s}$  and 40 kDa is  $44 \mu\text{m}^2/\text{s}^{23}$ . The addition of convection speeds up release and mixing by orders of magnitude to up to  $10 \text{mL}/\text{min}^{24}$ .

We develop here a capsule that can adjust its permeability to enclose or rapidly release its contents while also swelling and contracting to pump and mix the contents once released. A highly porous bacterial cellulose microcapsule<sup>25</sup> is used as a low-mass scaffold,  $\sim 100 \text{ng}$ , that is coated with poly(*N*-isopropylacrylamide), PNIPAM, a polymer coating that can be reversibly swelled using temperature changes<sup>26,27</sup>, due to change in PNIPAM solubility in aqueous solution. This is due to the competition between enthalpic and entropic contributions to the overall free energy. The manifestation of this, for a PNIPAM brush, is movement of waters of solvation out of the brush as temperature is increased, which results in brush collapse.

The thermal response enables us to control the hybrid capsule pore size and overall volume as rapidly swelling or shrinking the overlapping nano-fibers alters fiber spacing as well as fiber volume. The increased elasticity of the polymer-coated fibers enables the hybrid capsules to easily recover from mechanical deformation. Repeated cycling of the volume transition is found to produce bulk flow around the capsule, driving significant cycles of inward and outward flow of the capsule contents. The response can be tuned by variation of the amount of grafted PNIPAM. We synthesize and characterize five versions of these hybrid capsules by varying reaction time and extent to control polymer molecular weight and volume.

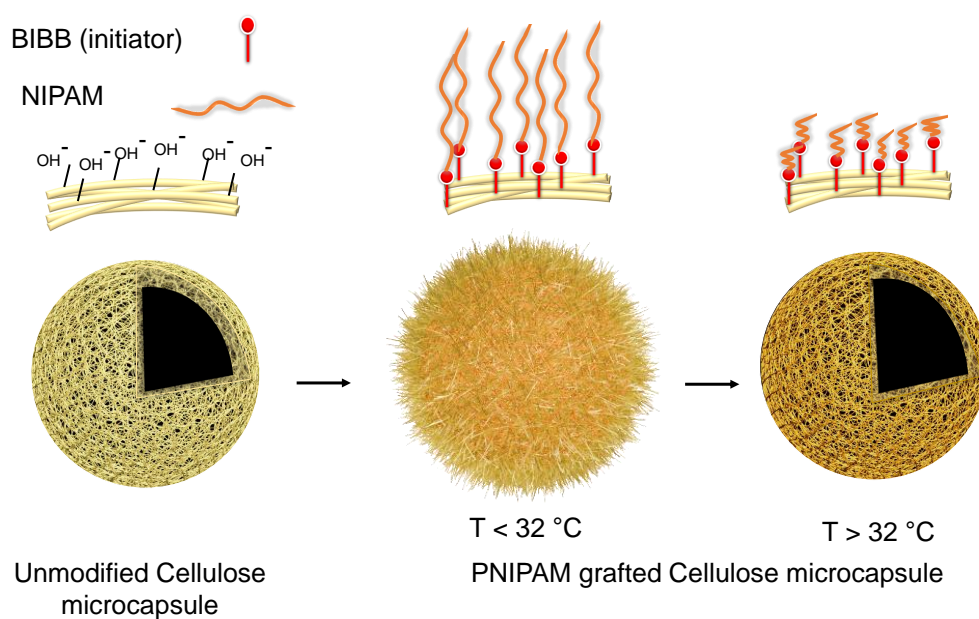


**Figure 3.1:** Schematic of the functionalization of a cellulose microcapsule with surface-grafted PNIPAM. As shown in the zoomed-in schematics at the top, the microcapsule was functionalized with PNIPAM in a two-step process: covalent attachment of BIBB as a polymerization initiator, followed by grafting of PNIPAM from attached BIBB via ARGET ATRP as per the method of Humphreys et al.<sup>27</sup>. The fiber coatings can then be swelled and shrunk using changes in temperature to induce thermoreversible swelling of the PNIPAM.

## 3.2 Materials and methods

**Cellulose microcapsule preparation:** Cellulose microcapsules with diameters in the range of 50 to 1000  $\mu\text{m}$  were synthesized by a bio-interfacial process previously developed by our group<sup>25</sup>. In brief, bacterial cellulose microcapsules were grown using a monodisperse emulsion of bacterial culture droplets as templates. The bacterial culture contains purified xylinum; *Acetobacter xylinum* was purified and concentrated from Kombucha culture (Nourishme Organics, Australia) by gradient centrifugation. Coconut water (Cocoa, Indonesia), and 10% w/v table sugar was added as nutrients to create water in oil emulsion drops. Within 10 days, the encapsulated bacteria polymerize the glucose molecules into cellulose nanofibers with a diameter of 60 to 70 nm, that then entangled to form an interconnected random fiber shell with a total thickness of 20 to 50  $\mu\text{m}$  and a pore size of 0.5  $\mu\text{m}$ <sup>25</sup>.

**Dehydration of cellulose microcapsules:** The washed cellulose microcapsules were placed into a 15 mL Falcon centrifuge tube and allowed to settle before the supernatant was drawn off with a syringe, leaving  $\sim 0.5$  mL remaining. The Falcon tube was then filled with THF (Tetrahydrofuran, 99% , Sigma Aldrich) and gently mixed. After the microcapsules settled the supernatant fluid was drawn off and more THF added. The solution was exchanged in this manner five times; leaving  $\sim 0.000123$  %vol water remaining in the solution. After this, the microcapsules were transferred to a 5 mL glass vial which was filled with anhydrous THF (dried over 4 Å molecular sieves) and the top stoppered with cotton wool. The stoppered 5 mL vial was then placed into a 50 mL vial containing 4 Å molecular sieves that was then filled with more anhydrous THF. The 50 mL vial was stoppered with a suba-seal and left overnight, allowing residual water from the solution to be adsorbed by the molecular sieves.

**Attachment of polymerization initiator:** The microcapsules were transferred to a 5 mL vial that had been dried at 50 °C, which was subsequently filled with 3 mL of anhydrous THF and sealed with a suba-seal. Then 0.5 mL of TEA (triethylamine,  $\geq 99\%$ , Sigma Aldrich) was added to the vial, followed by 0.4 mL of BIBB ( $\alpha$ -bromoisobutyryl bromide,  $\geq 98\%$ , Sigma Aldrich). Upon addition of the BIBB, a white precipitate formed and remained for the entire reaction time. The reaction was allowed to proceed for one hour, during which the BIBB reacted with the hydroxyl groups on the cellulose fibers, leaving them decorated with organobromine ATRP initiators. The reaction was halted by pouring the solution into a 50 mL vial containing 30 mL of ethanol then, microcapsules remaining in the 5 mL vial were removed by rinsing the vial with ethanol. The white precipitate dissolved in the ethanol solution, and the microcapsules were allowed to settle. The solution was then exchanged to methanol via the same method used for water-THF solution exchange in the previous step.

**Polymerization:** In this work the activators regenerated by electron transfer atom transfer radical polymerization (ARGET ATRP) method was used to graft PNIPAM from the cellulose framework of the microcapsules; our method is based off that of Humphreys et al.<sup>27</sup>. The molecular weight of the grafted polymers is a function of both the polymerization time and the polymerization rate ( $K_{\text{ATRP}}$ );  $K_{\text{ATRP}}$  is accelerated as the solvent polarity is increased<sup>28</sup>, which is dictated in our system by the ratio of water to methanol in the solvent. In this work we used two solvent compositions (water/methanol of 1:2 and 2:1, reactions A and B, respectively) and a number of reaction times to prepare polymer coatings with a range of polymer thickness. The polymerization solution was prepared such that there was 0.05 mg/mL of NIPAM in solution, and the molar ratio of NIPAM to HMTETA (1,1,4,7,10, 10-hexamethyltri-ethylenetetramine,  $\geq 97\%$ , Sigma Aldrich) to  $\text{CuBr}_2$

(copper (II) bromide,  $\geq 99\%$ , Sigma Aldrich) to ascorbic acid ( $\geq 99\%$ , Sigma Aldrich) was 900:10:1:6.6.

Before the polymerization the brominated cellulose microcapsules were placed in a methanol solution. These microcapsules were then placed into a 5 mL vial with a measured amount of methanol (here we assume that the microcapsule weight is negligible). The methanol solution was deoxygenated by purging with nitrogen for at least 15 minutes. Concurrently, a polymerization solution was prepared by dissolving NIPAM in MilliQ water in a round-bottomed flask. To this solution, HMTETA and  $\text{CuBr}_2$  were added according to the above molar ratios. A stirrer bar was then added and the flask sealed with a suba-seal. The polymerization solution was deoxygenated by purging with nitrogen for 15 min, after which ascorbic acid was added to the solution, causing the color of the solution to change from pale blue to colorless. After a further fifteen minutes of deoxygenation, a calculated amount of the polymerization solution was syringed from the round-bottomed flask into the 5 mL vial containing the microcapsules in methanol. Water, methanol, and polymerization solution quantities were calculated such that this final solution possessed the solvent ratio, NIPAM concentration, and reagent ratios outlined in the above paragraph. Functionalized microcapsules can be prepared in many vials simultaneously using this method, allowing the polymerization time to be varied for study of PNIPAM molecular weight effects.

After the allotted polymerization time, the microcapsules were transferred from the 5 mL vial to a 50 mL Falcon tube containing 30 mL of ethanol. The reduction of solvent polarity, exposure to oxygen, and rapid dilution effectively halted the polymerization. The capsules were allowed to settle before the supernatant liquid was removed. The capsules were washed in this manner twice more in ethanol before being transferred to MilliQ water via the solvent exchange method used above. The

polymerization conditions corresponding to the microcapsules discussed in this work are summarized in Table 3.1.

### 3.2.1 Sample imaging and analysis

**Optical microscopy** Confocal light-sheet microscopy (CLSM) was used to image fiber networks and conduct fluorescence measurements. A Zeiss LSM 880 microscope with Airyscan module was used for all CLSM measurements. A 63× oil immersion objective (numerical aperture of 1.4) was used for confocal imaging of coated fiber with PNIPAM at room temperature and a 20× dry objective (numerical aperture of 0.16) was used for FITC-dextran permeability experiment.

Rhodamine B (RhB) staining was used to visualize the tethered PNIPAM, and was carried out using the following established labeling protocol of Silverberg et al.<sup>29</sup>. First 2 mg of Rhodamine B isothiocyanate (RhB) were dissolved in 2.5 mL of sodium carbonate-bicarbonate buffer (0.5 M, pH 9.5). Then, the RhB solution was added into 1 mL solution (water) containing the PNIPAM functionalized capsules (~85 capsules). The mixture was agitated overnight at room temperature in darkness. The capsule was rinsed with Milli-Q-water several times to remove any unattached dye.

FITC labeled dextran, with molar masses of 4 kDa, with hydrodynamic diameter of approximately 1.8 nm, was used as fluorescent probe to quantify capsule permeability<sup>30,31</sup>.

Optical microscopy was used to observe the microcapsule response to temperature and mechanical deformation. Images were acquired using a stereoscope (WILD M3C, Leica, Germany) with a 6.4× objective, and an inverted optical microscope with a 10 and 40× objective along with a digital camera (Moticam 10 MP, Taiwan). The inverted optical microscope was equipped with a temperature-controlled stage

(T96-P, Linkam) with a maximum heating and cooling rate of 20 °C/min. Polymerized capsules were immersed into 2 mL of 1 mg/mL FITC-dextran solution and incubated for 24 h at 25 °C. These microcapsules were then imaged with confocal fluorescence microscopy at room temperature, with fluorescence intensity quantified using ImageJ<sup>32</sup> to determine the degree of permeation of the capsules by the dextran tracer molecule.

**Particle tracking:** Polystyrene tracer particles with a 3 μm diameter were used to track and map the flow around functionalized capsules during their volume transition. Capsules were soaked in the tracer water dispersion for 1 hour. The suspension of tracers and polymerized capsules was placed (RT 75 min) into a closed-end square capillary (VitroCom) with a side-length of 1 mm

A mixture of tracer and polymerized capsule (sample 5) was placed into a closed end square capillary (VitroCom) with a side-length of 1 mm and tracked particle displacement tracked over time, using image analysis both at room temperature and while cycling between 23;40 °C. The velocity of tracers was measured at 2 fps acquisition rate. ImageJ software was used for particle tracking. The TrackPy module<sup>33</sup> was used to calculate mean-squared displacement (MSD),  $\Delta r^2(\Delta t) = (r(t + \Delta t) - r(t))^2$ , as a function of the lag time,  $\Delta t$  at 23;40 °C<sup>34</sup>.

**Fourier-transform infrared spectroscopy:** FTIR absorption spectra were collected using a Bruker IFS66/S High End FT-NIR/IR Spectrometer, with a wavenumber range from 400 – 4000 cm<sup>-1</sup>.

Measurements were performed on air-dried microcapsules, which were carefully placed on the crystal and secured with the pressure arm. The crystal was washed with isopropyl alcohol before use.

**Scanning electron microscopy:** Scanning electron microscopy (SEM) was used to confirm the grafting of polymer to the microcapsules and examine the nanos-

structures formed. A FEI Nova Nano SEM 450 FE-SEM with an accelerating voltage of 5.0 kV was used for all SEM imaging. Before SEM imaging, samples were snap-frozen in liquid nitrogen, dehydrated overnight in a freeze drier, and coated with a 30 nm thick platinum layer using a Leica ACE600 sputter coater.

### 3.3 Results and discussion

Bacterial cellulose microcapsules are synthesized by encapsulating drops of aqueous *Acetobacter* bacteria culture in gelled oil<sup>25</sup>. The bacteria produce hollow, porous capsules from entangled micron-scale cellulose fibers, Figure 3.1. The bacterial cellulose microcapsule is robust enough to enable encapsulation and its flexible mesh shell can be functionalized to increase its applications. Adding PNIPAM to the surface of the capsule's cellulose fibers enables a temperature-controlled change in the effective size of the fiber<sup>26,27</sup> that can be used to change capsule permeability and shape and drive secondary effects like fluid flow. The process of coating cellulose fibers with PNIPAM is shown schematically in Figure 3.1. The individual cellulose fiber of the capsule was coated with PNIPAM using a two-step process; covalent attachment of polymerization initiator (BIBB) and grafting of PNIPAM from the attached BIBB, Figure 3.1.

#### 3.3.1 Capsule characterization

We establish the presence of tethered PNIPAM layers through Fourier-transform infrared, FTIR, spectroscopy with results shown in Figure 3.2. The peaks at  $1450\text{ cm}^{-1}$ ,  $1525\text{ cm}^{-1}$  and  $1650\text{ cm}^{-1}$ , which can be attributed to the stretching of C-N, amide (II) band and amide (I) band, respectively, are characteristic absorption bands of PNIPAM. The peaks in the  $2800 - 2980\text{ cm}^{-1}$  region correspond to the asymmetric and symmetric stretching of methylene ( $\text{CH}_2\text{H}_2$ ) groups in long alkyl chains. A

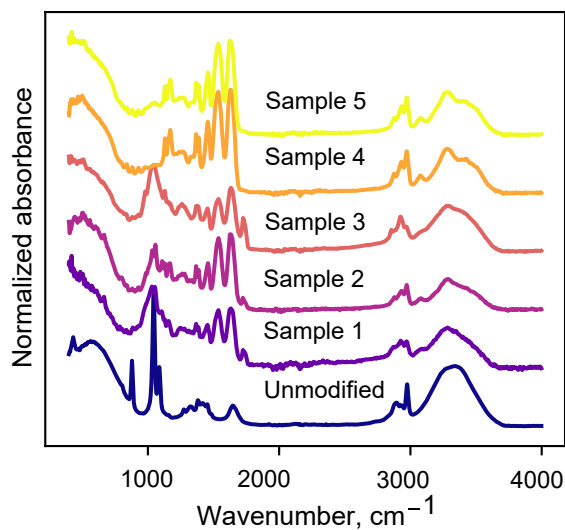


**Figure 3.2:** FTIR spectra of cellulose microcapsules corresponding to the samples presented in Figure 3.3. Absorbance peaks at  $1450\text{ cm}^{-1}$ ,  $1525\text{ cm}^{-1}$  and  $1650\text{ cm}^{-1}$  indicate the presence of PNIPAM and generally intensify with increasing sample number, agreeing with the trend presented in Table 3.1

sharper peak was observed at  $1054\text{ cm}^{-1}$  that can be ascribed to the oxygen-containing groups of CO stretch. The absorption peak in the range of  $1605$  to  $1657\text{ cm}^{-1}$  represents the CO stretch. The appearance of these characteristic peaks in the spectra of the modified cellulose microcapsules verifies successful grafting of PNIPAM<sup>35</sup>.

Polymer thickness can be tuned by varying the reaction time and reaction rate. Scanning electron microscopy (SEM) was used to examine the change in fiber diameter upon grafting PNIPAM to the capsules, with representative images shown in Figure 3.3a-l. After polymerization, the average fiber diameter increased between 130; 1300%, from 60 nm to over 800 nm based on SEM data of freeze-dried samples. The polymer layer thickness was calculated based on pristine cellulose fibers possessing a diameter of approximately 60 nm<sup>25</sup>. At low polymer layer thicknesses, ‘webbing’ is observed at intersection points between the fibers and there appears to be a greater tendency for small fibers to stick together. As the polymer thickness increases further, individual fibers are no longer observed. A transition between

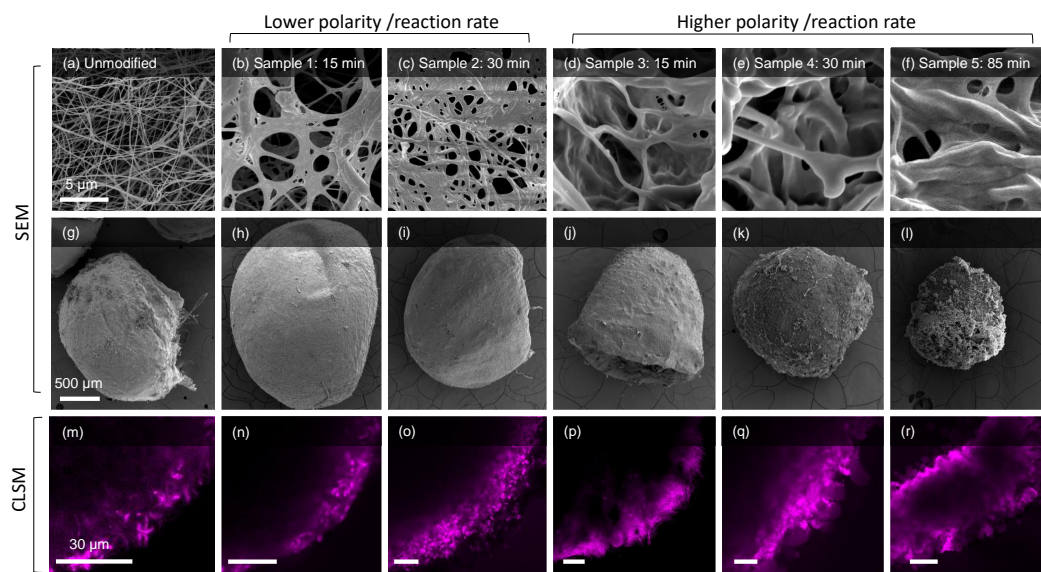


**Figure 3.3:** SEM images of pristine and polymer-modified cellulose microcapsules. The target polymer thickness increases with increasing sample number; further details can be found in Table 3.1. (a-l) SEM images of freeze-dried microcapsules, illustrating that polymerisation significantly increases the fiber thickness and modified the capsule nanostructure. (m-r) Confocal microscopy of Cellulose microcapsules (m) stained with Congo red and (n-r) functionalized cellulose capsule, with PNIPAM stained with Rhodamine B.

coated fibers and a continuous polymer-fiber mat occurs between samples 2 and 4 for polymer thicknesses of 160-450 nm.

We note that it is extremely difficult to calculate the precise amount of grafted PNIPAM in our system, as our chemistry does not allow for the polymer chains to be degrafted and measured, and thermal decomposition methods are not viable due to the organic nature of the cellulose substrate. As the bromination step was consistent across all capsules studied, we anticipate that the grafting density is relatively uniform across all samples and the differences in measured polymer thickness are proportional to differences in polymer molecular weight. However, as we cannot be certain of this, and are similarly uncertain regarding the polydispersity of the chains, we subsequently refer to the difference in PNIPAM coatings as a difference

in polymer amount (mass per unit area). One factor that must be considered when calculating the amount of grafted polymer from the SEM images is the density of freeze-dried PNIPAM, which is unknown. Variations in density are a likely cause of the significant, yet consistent, discrepancy between the target polymer thickness based on syntheses from silica wafers<sup>27</sup> and the thickness measured via SEM (Table 3.1). It is also possible that the polymerization process binds small cellulose fibers together, resulting in the larger fiber thicknesses observed in the polymerized samples, for example Figure 3.3 b,c versus Figure 3.3a. One additional factor to consider is the tendency for confined environments to accelerate ATRP<sup>36</sup>. The SEM images in Figure 3.3 show that the amount of grafted PNIPAM consistently increases, but cannot reveal the absolute amount of grafted PNIPAM. It is worth stressing that the capsules are washed rigorously after functionalization, and stored in room-temperature water, a good solvent for ungrafted PNIPAM, for many days before the images in Figure 3.3 were captured. The PNIPAM-functionalized cellulose surfaces observed by SEM are similar to those seen by Wu et al.<sup>37</sup>, who grafted PNIPAM onto the larger fiber cellulose structure of filter paper, producing fiber surfaces covered with a layer of polymer. Wu et al. also found a smoother surface structure after increasing the percentage of polymer grafted, likely due to similar increases in connectivity of the PNIPAM regions as we see<sup>37-39</sup>. Taking the FTIR measurements together with SEM images and past observations, we are confident of successful covalent functionalization of the cellulose microcapsule substrate with PNIPAM.

Confocal laser scanning microscopy, CLSM, images demonstrate the effect of the polymer coating level on the thickness of the microcapsule shell in water, Figure 3.3(m-r). In these measurements, a Rhodamine B stain, colored purple in the images, labels the fibers within the microcapsule. The confocal images are of a single plane in the middle of the capsule, indicating a hollow capsule with a wall

**Table 3.1:** Polymerization conditions that produced the variety of functionalized micro-capsules used in this work.

<b>Reaction</b>	A		B		
<b>Sample number</b>	1	2	3	4	5
Water/Methanol ratio	1:2	1:2	2:1	2:1	2:1
Reaction time (min)	15	30	15	30	75
Target dry thickness (nm)*	10	20	35	60	95
Fiber thickness (SEM) (nm)†	140 ± 30	160 ± 30	300 ± 100	450 ± 150	850 ± 150
Polymer thickness (SEM) (nm)‡	40	50	120	195	395
Swollen polymer to cellulose ratio (SEM) ‡	0.67	0.83	2	3.25	6.58
Shell thickness (CLSM) (µm)‡	30	45 – 50	80	112	140

\* Based on equivalent synthesis on planar silicon substrates via the method of Humphreys et al.<sup>27</sup>.

† Fiber thickness from SEM images taken post polymerisation. Samples are freeze-dried before imaging to depict porous structure of capsule and the thickness of PNIPAM layer.

‡ Assuming an average unmodified fiber thickness of 60 nm and shell thickness 25 µm.

thickness of 20-25  $\mu\text{m}$  before polymerization, Figure 3.3m, which is in agreement with the shell thickness of bacterial cellulose microcapsule previously reported by Song et al.<sup>25</sup>.

The dark region within the capsule wall in Figure 3.3m-r is a hollow core that can be used to carry a payload of particles or proteins, for example. The images in Figure 3.3m-r focus on the capsule shell and show the effect of polymerization time and reaction rate at this length scale of the capsules.

Increasing either reaction time or reaction rate increases the polymer coating thickness, in turn reducing the capsule pore size. For the same reaction time of 15 min, Sample 1 and Sample 3, the higher reaction rate of Sample 3 shows a larger PNIPAM coating, resulting in 2.1 times thicker fibers and 2.6 times thicker capsule walls along with smaller pore sizes Figure 3.3. As the polymerization time increases in both high and low polymerization rates, we observe that both the thickness of fibers, Figure 3.3a-f, and the wall of the microcapsule increase, Figure 3.3m-r, by a factor of 10 for maximum reaction time and the polymerization rate for Sample 5 (Table 3.1). The thickness of the PNIPAM layer on the cellulose fiber of microcapsules in this study spans a range, allowing control of properties such as the amount of water absorbed and released during temperature cycles, enabling the design of capsule changes at bulk and micron length scales.

### 3.3.2 Permeability

The permeability of PNIPAM-functionalized microcapsules in water was studied by examining the concentration of FITC-labeled 4 kDa dextran that diffused into the capsules after a 24 h incubation period, Figure 3.4<sup>6,17,40</sup>. FITC-labeled dextran fluoresces green, so higher intensities correspond to a higher concentration, while black regions of the image indicate the absence of the tracer molecule. As shown

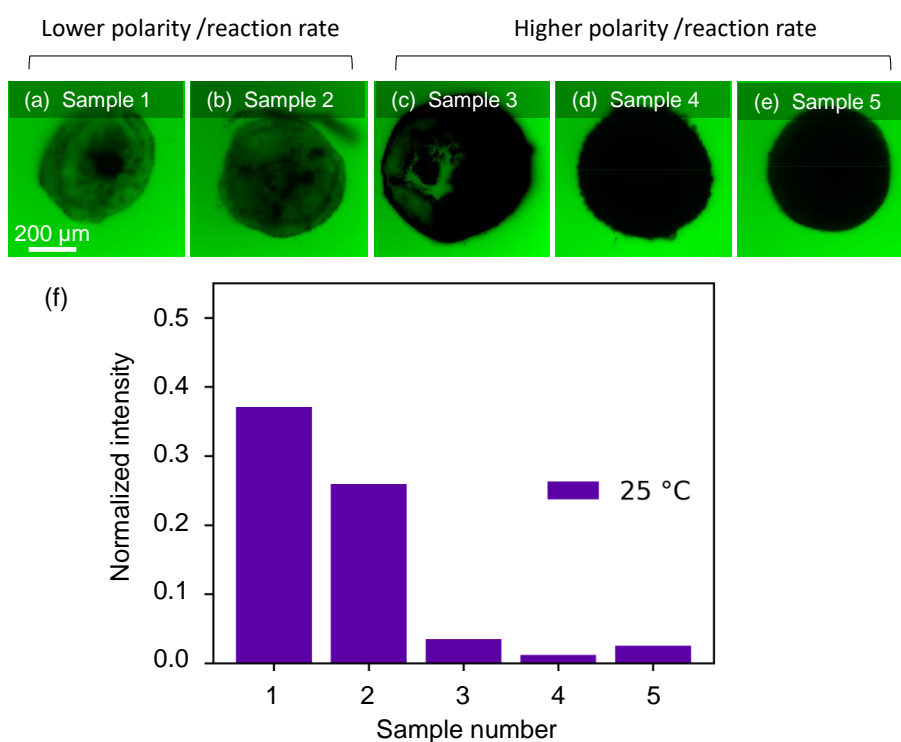


**Figure 3.4:** Effect of PNIPAM functionalization on cellulose capsule permeability at room temperature. (a-e) CLSM images of polymer-modified cellulose microcapsules incubated in 4kDa FITC-labeled dextran at 25°C show increasing polymer thickness decreases capsule permeability. Fluorescent intensity is normalized by dividing the average intensity inside the capsule to the average background intensity of the external fluid (f).

in Figure 3.4a-e, the fluorescence intensity of 4 kDa FITC-dextran with a hydrodynamic radius of  $\sim 1.8 \text{ nm}$ <sup>41</sup> is lower inside than outside for all of the microcapsules studied. As the PNIPAM amount attached was increased, the internal intensity of FITC-dextran decreased as the capsule pore size became similar to, then smaller than, the 4 kDa dextran's hydrodynamic diameter of  $\sim 1.8 \text{ nm}$ . For Samples 4 and 5 no permeation of the capsule by dextran is detectable, indicating a reduction of pore size from a starting point of  $500 \text{ nm}$ <sup>25</sup> to below the functional tracer size (Figure 3.4)a-f. As might be expected, as fiber size increases and pore size decreases, the mechanical properties of the capsules are also altered by increasing attachment of PNIPAM.

### 3.3.3 Deformation and shape memory

Because of the low solid density and small characteristic length scales of the cellulose microcapsules, capillary forces encountered during drying will have a strong influence on the size and shape of the particles. Here we study the deformation and recovery of the PNIPAM-functionalized microcapsules during drying and re-hydration. Drying collapsed the pristine cellulose capsules completely, forming a flat disk with a thickness,  $\sim 100 \text{ nm}$ , less than 1% of the initial hydrated capsule radius, Figure 3.5a. Similar behavior was observed for Samples 1 and 2 that had smaller amounts of PNIPAM attached, with the capsules collapsing to a thin disk upon drying (Figure 3.5a). For higher thickness coatings of PNIPAM in Samples 3-5, however, a remarkable difference is evident in their drying behavior. The increased PNIPAM coating allows the capsules to maintain much of their structure upon complete dehydration as a result of a presumed significant increase in elastic modulus.

Capillarity is the dominant force that drives the observed folding of the cellulose capsule structure during drying<sup>25,42</sup>. This force results in the capsule crumpling,

as the cellulose fibers dynamically reconfigure to minimize the area of the energetically unfavorable solid/air interface. As the liquid continues to evaporate, the capsule is deformed further, with the maximum capillary tension occurring when the meniscus radius is small enough to just fill the pores<sup>43</sup>.

Capillary force pulls the fibers sufficiently close together<sup>44</sup> that strong hydrogen bonds and van der Waals interactions cause the fibers to permanently stick together. Coating cellulose fibers with PNIPAM covers fibers even at lower PNIPAM levels, blocking the close, irreversible adhesion interactions. As a result, drying of PNIPAM-cellulose microcapsules is a reversible process and they can reswell upon rehydration. Previous work by Song et al.<sup>25</sup> showed that pristine cellulose microcapsules can not reswell upon rehydration, instead remaining as a thin collapsed disk. In contrast, all dehydrated PNIPAM-functionalized capsules studied here reswelled to their initial shape and size upon immersion in water. We observed that this collapse/reswelling behavior was consistent across at least five drying/rehydration cycles, indicating an additional benefit of the robust PNIPAM coating.

An additional demonstration of the flexibility of the PNIPAM cellulose capsules under stress is shown by their shape recovery after compressive deformation by a blunt capillary<sup>25</sup>. Song et al.<sup>25</sup> found that pristine cellulose capsules could only recover from less than 20% strain, with greater deformation permanently altering the shape of the capsule. Here attachment of PNIPAM to the cellulose network greatly improved the post-deformation shape-recovery of the capsules. In Figure 3.5, the PNIPAM-functionalized microcapsule from the Sample 2 batch fully recovers its initial shape after even 100% deformation. This recovery occurred quickly, generally within five seconds after removal of the applied stress, and was independent of the initial deformation rate and reproducible over at least five cycles of deformation. We hypothesize that PNIPAM alters the mechanical response of the

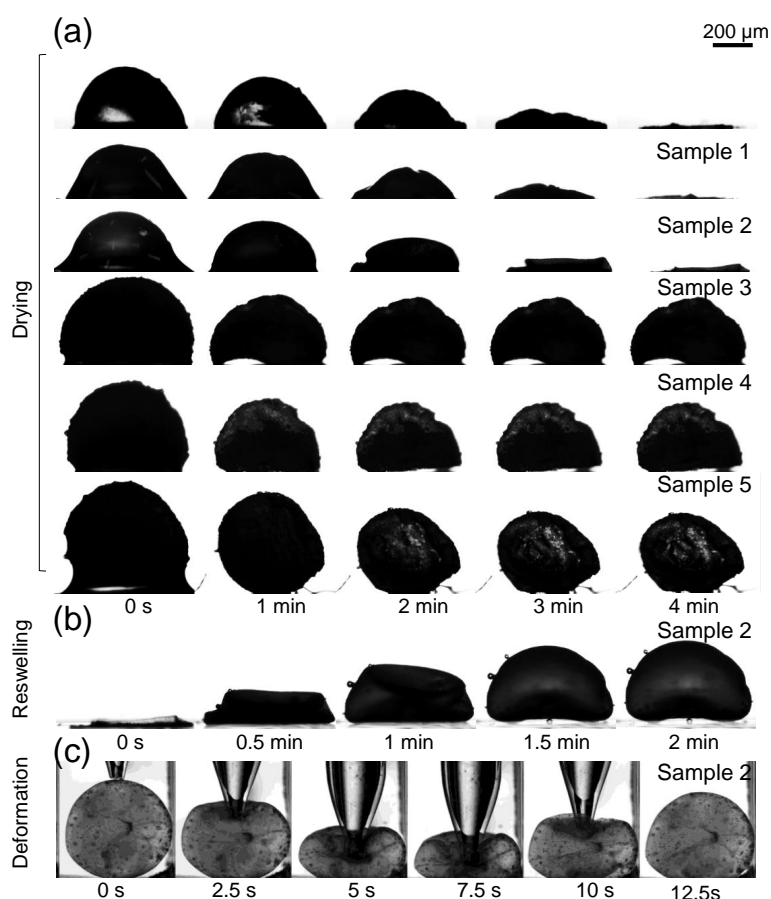


**Figure 3.5:** (a) Air drying of cellulose microcapsules before and after coating with PNIPAM. Cellulose capsules can collapse to a flat sheet during drying; however, the thickness of the final air-dried sheet increased with additional attached PNIPAM amounts. Samples 3-5 do not fully compress upon drying as their PNIPAM coating reinforces them to a greater extent. (b) All PNIPAM-cellulose capsules reswell after immersion in water, but the pristine cellulose capsule does not. (c) Functionalized capsules (Sample 2) recover after compressive deformation with a blunt-end pulled glass microcapillary.

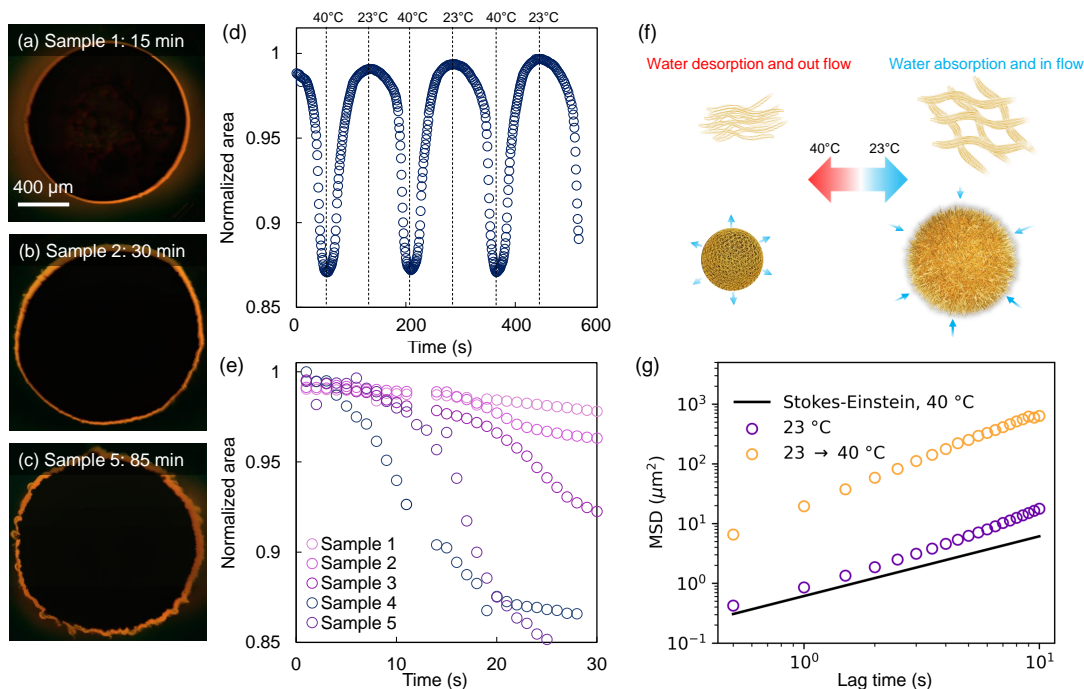


**Figure 3.6:** (a-c) Collapsed image stacks of PNIPAM-cellulose microcapsules undergoing thermoreversible swelling. The orange regions highlight the areas of greatest standard deviation of change between from initial image at room temperature and a final capsule image at 40 °C. (d) Multiple cycles of temperature-induced area changes 23;40 °C, PNIPAM modified capsule shows the same rate for each polymerization time in each cycle. (e) Increasing the amount of PNIPAM increases the volume transition magnitude and rate. (f) Schematic of the PNIPAM polymerized capsule volume transition and releasing and absorbing water. (g) Mean squared displacements of 3  $\mu\text{m}$  particles measured at 23 °C and while the temperature is changing from 23;40 °C, alongside the theoretical diffusion coefficient at 40 °C calculated using the Stokes-Einstein equation<sup>46</sup>.

capsule through two mechanisms: preventing the irreversible adsorption of cellulose fibers and mechanically reinforcing the cellulose fibers. It is worth noting that the functionalized capsules are mechanically distinct from conventional cross-linked PNIPAM. PNIPAM hydrogels have high elastic moduli (Young's Modulus of 45 kPa before the phase transition<sup>45</sup>) compared to cellulose microcapsules (Young's modulus 100 Pa<sup>25</sup>).

### 3.3.4 Changes in capsule volume with temperature

Capsules undergoing reversible volume transitions have proposed uses as payload delivery vehicles and capsules that ‘swim’ via jellyfish-like contractions<sup>47</sup>. Here we imaged a series of capsules while cycling the temperature between 23;40 °C at a constant rate of 20 °C/min to quantify the dynamics of microcapsule response. Figure 3.6a-c show the standard deviation of the Z projection of a stack of images taken during the temperature-induced volume transition of a PNIPAM-functionalized microcapsule, creating a composite image highlighting the change in capsule dimensions. The orange color in Figure 3.6a-c highlights the areas of the image that most change over time as the capsule boundary moves during swelling and contraction. From the images, we can see capsules with thicker polymer layers exhibit a larger volume transition. To better quantify the volume transition, the area of the polymerized capsule was measured over time and is plotted in Figure 3.6d-e with time. We find that the change in area of low MW samples (sample 1) is ~ 4%, while sample 4 changes by approximately ~ 13% (Figure 3.6(e-g)), corresponding to volume changes of ~ 6-19% , respectively. We also find that this volume transition is reversible over four hot-cold cycles with no apparent loss of response, Figure 3.6d.

The capsules exhibit a much smaller change in volume than comparably sized pure-PNIPAM capsules, which undergo a change in diameter of around 50%<sup>48-52</sup>. This difference can be attributed to the cellulose framework that forms the capsules maintaining the capsule structure throughout the polymer collapse. It is worth emphasizing here that the PNIPAM thermotransition should not be characterized as a hydrophilic to hydrophobic transition<sup>53</sup>, and as such the polymer coating is not drastically changing the surface energy of the cellulose. Here, by changing the temperature at a rate of 20 °C/min, we compare the volume transition magnitude

and rate for polymerized capsules with varying thickness of PNIPAM coating. Figure 3.6 (h and i) shows that increasing the PNIPAM coating thickness significantly increases the area transition rate and magnitude.

One side-effect of the volume transition is the exchange of fluid in the interior of the microcapsule with the external fluid. This expulsion is due both to the macroscopic contraction of the capsule as well as the desolvation of the PNIPAM chains undergoing their thermally driven collapse. In Figure 3.6f it can be seen that the capsule expels water as the temperature is increased past its LCST, and reabsorbs the water as the temperature is once again reduced below the LCST.

The maximum volume transition of PNIPAM-microcapsule is 15% of its area within the 20 s; the rate of capsule volume transition is tracked using ImageJ software. We measured the radial displacement of the capsule during swelling and shrinkage—this helped to predict the flow around the microcapsule. By increasing temperature to over 32 °C, PNIPAM-microcapsules contract with a radial velocity of 3  $\mu\text{m/s}$ , therefore when we used a tracer to track flow around the capsule, we expected to record tracer motion toward the capsule with similar capsule radial velocity. However, we have observed the tracer moved away from the microcapsule with the average velocity of 4  $\mu\text{m/s}$ . This is due to a release of water during the NIPAM layer shrinkage. The exchange also leads to an increase in the capsule permeability due to reducing the size of the polymer layer, which leads to water flow out from inside the capsule. Hence, the overall size of the capsule is changing, the constant amount of water released and absorbed during the shrinkage and swelling (around 48  $\mu\text{L}$  measured based on capsule volume change), and capsule pore size changes, leads to release of water from the capsule core during shrinkage. ultimately, the capsule fills with water during capsule swelling. Compared with other hydrogels, PNIPAM-microcapsule volume transition is 10 times faster; however, the maximum

strain that can be achieved here is 15%, which is 3 times less than other reported responsive microgels<sup>5,54–56</sup>.

### 3.3.5 Particle tracking during multiple cycles of temperature change

We observed that the temperature-modulated volume transition documented above (Figure 3.6) induces flow around the capsule as its fluid contents are manipulated. We characterize this phenomenon by using 3  $\mu\text{m}$  tracers to map the flow around the capsules during their shape transition. To confirm that this motion was due to the contraction of the capsules, and not a temperature-driven increase in Brownian motion, we calculate the theoretical MSD of a 3  $\mu\text{m}$  tracer at 40 °C via the Stokes-Einstein equation<sup>46,56</sup>. Figure 3.6g shows that while the 23 °C data matches the expected diffusive behavior, particle motion upon temperature cycling results in a significant increase in tracer particle motion above the predicted diffusive result.

Further studies of the fluid flow around sets of one, two, and three microcapsules undergoing thermal cycling are shown using tracer particle trajectories in Figure 3.7(a-c). Using the Z project tool in ImageJ we superimpose multiple frames into a single image to indicate the tracer particle trajectories as temperature changes. Figure 3.7(a) shows that for a single microcapsule tracers move toward and away from the PNIPAM-coated microcapsules. Tracers between two microcapsules are influenced by two sources of fluid flow, resulting in linear forward and backward motion between the two microcapsules. When we used three microcapsules, we can see the tracer particles have rotational motion between them. This can provide the chaotic flow required for fluid mixing. To quantify the tracer particle motion, we track the individual tracers and measure their average velocity. When three polymerized microcapsules were used, the tracers moved with higher average velocity, 42  $\mu\text{m}/\text{sec}$ ,

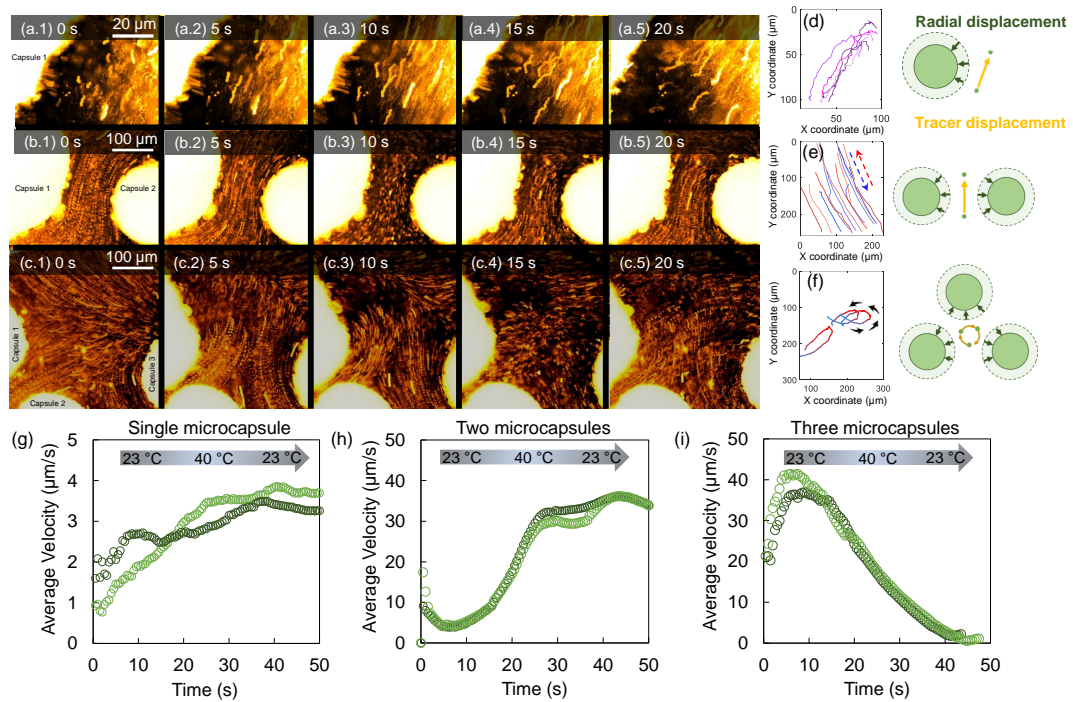


**Figure 3.7:** Tracer particles are used to quantify fluid flow fields around PNIPAM-coated capsules in multiple cycles of temperature changes between 25;40°C. Tracer trajectories around (a and d) single, (b and e) two, and (c and f) three capsules. Average velocity over time in (g-i)

while the lowest velocities are seen for a single microcapsule as a result of different levels of volumetric flow rates.

The coupling between thermally triggered release of a capsule contents and convective mixing of the materials with the external fluid is an interesting aspect of the capsules potential applications.

### 3.4 Conclusions

We have functionalized cellulose microcapsules with the thermoresponsive polymer PNIPAM to develop capsules with switchable permeability, thermo-actuated motion and improved mechanical properties. We have used two different polymerization rates and several reaction times to study the effect of PNIPAM layer

thickness on capsule behavior. The synthesized capsule is mechanically robust and can elastically recover to its initial shape after dehydration and 100% deformation. Particle tracking was employed to quantify fluid motion around the capsules during multiple cycles of temperature change, even when capsule volume change was relatively small. We suggest the use of this effect to promote both release and mixing of capsule fluid contents at enhanced rates. Despite their extremely low mass, the capsules are strong enough to provide multiple functions using simple temperature variations as a trigger.

## References

- [1] S. Roberts, V. Miao, S. Costa, J. Simon, G. Kelly, T. Shah, S. Zauscher, A. Chilkoti, *Nature Communications* **2020**, *11*, 1–10.
- [2] S. Boostani, S. M. Jafari, *Trends in Food Science & Technology* **2021**, *109*, 303–321.
- [3] K. Kempe, K. F. Noi, S. L. Ng, M. Müllner, F. Caruso, *Polymer* **2014**, *55*, 6451–6459.
- [4] A. Vian, E. Amstad, *Soft Matter* **2019**, *15*, 1290–1296.
- [5] Y. Long, C. Liu, B. Zhao, K. Song, G. Yang, C.-H. Tung, *NPG Asia Materials* **2015**, *7*, e148–e148.
- [6] T. Paulraj, A. V. Riazanova, K. Yao, R. L. Andersson, A. Müllertz, A. J. Svagan, *Biomacromolecules* **2017**, *18*, 1401–1410.
- [7] J. M. Unagolla, A. C. Jayasuriya, *European Journal of Pharmaceutical Sciences* **2018**, *114*, 199–209.
- [8] J. G. Werner, B. T. Deveney, S. Nawar, D. A. Weitz, *Advanced Functional Materials* **2018**, *28*, 1803385.

- 
- [9] S. U. Ahmad, B. Li, J. Sun, S. Arbab, Z. Dong, F. Cheng, X. Zhou, S. Mahfuz, J. Zhang, *Journal of Veterinary Pharmacology and Therapeutics* **2021**, *44*, 298–312.
- [10] T. Lu, B. Li, D. Sun, M. Hu, J. Ma, G. Sun, *Journal of Cleaner Production* **2021**, *294*, 126270.
- [11] R. Dong, B. Zhu, Y. Zhou, D. Yan, X. Zhu, *Angewandte Chemie International Edition* **2012**, *51*, 11633–11637.
- [12] T. Wang, J. Xu, X. Fan, X. Yan, D. Yao, R. Li, S. Liu, X. Li, J. Liu, *ACS Applied Materials & Interfaces* **2019**, *11*, 47619–47624.
- [13] Q. Yan, R. Zhou, C. Fu, H. Zhang, Y. Yin, J. Yuan, *Angewandte Chemie International Edition* **2011**, *50*, 4923–4927.
- [14] S. K. M. Nalluri, B. J. Ravoo, *Angewandte Chemie International Edition* **2010**, *49*, 5371–5374.
- [15] S. Zhao, P.-H. Huang, H. Zhang, J. Rich, H. Bachman, J. Ye, W. Zhang, C. Chen, Z. Xie, Z. Tian *et al.*, *Lab on a Chip* **2021**, *21*, 2453–2463.
- [16] R. A. Siegel, M. J. Rathbone in *Fundamentals and applications of controlled release drug delivery*, Springer, **2012**, pp. 19–43.
- [17] H. Kim, S.-M. Jo, F. Meng, Y. Guo, H. Thérien-Aubin, R. Golestanian, K. Landfester, E. Bodenschatz, *Advanced Functional Materials* **2020**, *30*, 2006019.
- [18] S.-H. Kim, J.-G. Park, T. M. Choi, V. N. Manoharan, D. A. Weitz, *Nature Communications* **2014**, *5*, 1–8.
- [19] W. Zhang, L. Qu, H. Pei, Z. Qin, J. Didier, Z. Wu, F. Bobe, D. E. Ingber, D. A. Weitz, *Small* **2019**, *15*, 1903087.
- [20] Y. Wang, W. Huang, Y. Wang, X. Mu, S. Ling, H. Yu, W. Chen, C. Guo, M. C. Watson, Y. Yu *et al.*, *Proceedings of the National Academy of Sciences* **2020**, *117*,

## References

---

- 14602–14608.
- [21] W. Fan, C. Shan, H. Guo, J. Sang, R. Wang, R. Zheng, K. Sui, Z. Nie, *Science Advances* **2019**, 5, eaav7174.
- [22] J. C. Nawroth, H. Lee, A. W. Feinberg, C. M. Ripplinger, M. L. McCain, A. Grosberg, J. O. Dabiri, K. K. Parker, *Nature Biotechnology* **2012**, 30, 792–797.
- [23] S. Limem, P. Calvert, *Journal of Materials Chemistry B* **2015**, 3, 4569–4576.
- [24] Z. Chen, L. Shen, X. Zhao, H. Chen, Y. Xiao, Y. Zhang, X. Yang, J. Zhang, J. Wei, N. Hao, *Applied Materials Today* **2022**, 26, 101356.
- [25] J. Song, F. Babayekhorasani, P. T. Spicer, *Biomacromolecules* **2019**, 20, 4437–4446.
- [26] A. Halperin, M. Kröger, F. M. Winnik, *Angewandte Chemie - International Edition* **2015**, 54, 15342–15367.
- [27] B. A. Humphreys, J. D. Willott, T. J. Murdoch, G. B. Webber, E. J. Wanless, *Physical Chemistry Chemical Physics* **2016**, 18, 6037–6046.
- [28] W. A. Braunecker, N. V. Tsarevsky, A. Gennaro, K. Matyjaszewski, *Macromolecules* **2009**, 42, 6348–6360.
- [29] J. L. Silverberg, A. R. Barrett, M. Das, P. B. Petersen, L. J. Bonassar, I. Cohen, *Biophysj* **2014**, 107, 1721–1730.
- [30] D. Lee, D. A. Weitz, *Advanced Materials* **2008**, 20, 3498–3503.
- [31] B. Kim, T. Y. Jeon, Y.-K. Oh, S.-H. Kim, *Langmuir* **2015**, 31, 6027–6034.
- [32] C. A. Schneider, W. S. Rasband, K. W. Eliceiri, *Nature Methods* **2012**, 9, 671–675.
- [33] u. . h. d. . z. v. . . Trackpy Contributors, title = trackpy.
- [34] T. G. Mason, J. Bibette, D. A. Weitz, *Physical Review Letters* **1995**, 75, 2051–2054.
- [35] X. Sun, E. DenHartog, X. Zhang, M. McCord, *Applied Surface Science* **2018**, 453, 182–191.

- 
- [36] E. M. Benetti, C. Kang, J. Mandal, M. Divandari, N. D. Spencer, *Macromolecules* **2017**, *50*, 5711–5718.
- [37] W. Wu, J. Li, W. Zhu, Y. Jing, H. Dai, *Fibers and Polymers* **2016**, *17*, 495–501.
- [38] J. Lindqvist, D. Nyström, E. Ostmark, P. Antoni, A. Carlmark, M. Johansson, A. Hult, E. Malmström, *Biomacromolecules* **2008**, *9*, 2139–2145.
- [39] H. Lönnberg, Q. Zhou, H. Brumer, T. T. Teeri, E. Malmström, A. Hult, *Biomacromolecules* **2006**, *7*, 2178–2185.
- [40] Y. Chen, W. Wei, Y. Zhu, J. Luo, R. Liu, X. Liu, *ACS Applied Materials & Interfaces* **2020**, *12*, 4821–4832.
- [41] M. Mobed-Miremadi, S. Djomehri, M. Keralapura, M. McNeil, *Materials* **2014**, *7*, 7670–7688.
- [42] A. R. Rebelo, A. J. Archer, X. Chen, C. Liu, G. Yang, Y. Liu, *Science and Technology of advanced MaTerialS* **2018**, *19*, 203–211.
- [43] G. W. Scherer, *Journal of the American Ceramic Society* **1990**, *73*, 3–14.
- [44] E. S. Ferreira, C. A. Rezende, E. D. Cranston, *Green Chemistry* **2021**.
- [45] Y. Jin, T. Yang, S. Ju, H. Zhang, T.-Y. Choi, A. Neogi, *Polymers* **2020**, *12*, 1462.
- [46] A. Einstein, *Annalen der physik* **1905**, *17*, 208.
- [47] K. Katija, J. O. Dabiri, *Nature* **2009**, *460*, 624–626.
- [48] W. H. Blackburn, L. A. Lyon, *Colloid and Polymer Science* **2008**, *286*, 563–569.
- [49] H. Kojima, F. Tanaka, C. Scherzinger, W. Richtering, *Journal of Polymer Science Part B: Polymer Physics* **2013**, *51*, 1100–1111.
- [50] T. Okajima, I. Harada, K. Nishio, S. Hirotsu, *The Journal of Chemical Physics* **2002**, *116*, 9068–9077.
- [51] H. Senff, W. Richtering, *The Journal of Chemical Physics* **1999**, *111*, 1705–1711.
- [52] J. Zhao, H. Su, G. E. Vansuch, Z. Liu, K. Salaita, R. B. Dyer, *ACS Nano* **2019**, *13*, 515–525.

## References

---

- [53] R. Pelton, *Journal of Colloid and Interface Science* **2010**, *348*, 673–674.
- [54] F. A. Plamper, W. Richtering, *Accounts of Chemical Research* **2017**, *50*, 131–140.
- [55] I. Sanzari, E. Buratti, R. Huang, C. G. Tusan, F. Dinelli, N. D. Evans, T. Prodromakis, M. Bertoldo, *Scientific Reports* **2020**, *10*, 1–14.
- [56] A. Banerjee, T. M. Squires, *Science Advances* **2019**, *5*, eaax1893.

## Chapter 4

# Drying cellulose microcapsules for the fabrication of particles with tunable structures

### 4.1 Introduction

Solid hollow capsules have been developed to contain, protect and release active ingredients in response to environmental stimuli for a wide range of applications in foods<sup>1</sup>, pharmaceuticals<sup>2</sup>, cosmetics<sup>3</sup>, and advanced materials<sup>4</sup>. For example, capsules can deform or switch permeability in response to stress, temperature, or osmotic pressure, allowing absorption or release of active materials<sup>5,6</sup>. Microcapsules have been synthesized with various mechanical properties, but the majority of microcapsules are made from rigid cross-linked polymers, or metals<sup>7-9</sup>. However, very rigid solid capsules' mechanical properties and porosity often restrict their flexibility in use. As a result, rigid capsules can often provide only single-use delivery due to permanent deformation and rupture when significantly stressed<sup>10</sup>. Solid metal and polymer capsules have large elastic moduli, ranging in magnitude from MPa to GPa for metal and several hundred Pa to kPa for polymers<sup>7-9</sup>.

Softer microcapsules have been developed that can be deformed and respond to external stimuli, but their low elastic modulus can limit their ability to remain stable against damage in applications until the need to trigger release of their contents<sup>11-13</sup>. A clear need is a type of capsule that is sufficiently strong against incidental damage or wear while remaining responsive to practical triggers of response and

release. An analogous example of a flexible and strong capsule with long-term stability and the ability to provide responsive release of active ingredients is the plant pollen grain. Pollen grains made largely of natural cellulose can swell, encapsulate, and perform osmotically-triggered release of their contents. We examine here the possibility of mimicking pollen grains' reversible folding and self-sealing during dehydration as a way to expand the development of controlled release capsules for various applications.

Recently, Song et al.<sup>14</sup> developed a soft and flexible microcapsule with an elastic modulus  $\sim 100$  kPa that is resistant to fluid shear stresses and large osmotic pressure differences due to its highly porous shell structure. Unlike past capsules made of solid cross-linked or crystalline shells, the microfibrillar cellulose capsule shells are made from inter-woven fibers, creating a mesh-like shell with an average pore size of 500 nm. The sparse shell structure means even millimeter- or micron-scale capsules can have extremely low solid mass, on the order of 200 ng, and possess high water-holding capacity in its core and mesh shell due to cellulose hydroxyl groups<sup>15</sup>.

The low-density structure offers a unique means to explore extreme changes in capsule volume and size by dehydration or solvent exchange. We find the bacterial cellulose structure can be used to mimic pollen self sealing during dehydration and we use surface modification of the fibers to avoid permanent deformation and sealing of the capsules by strong fiber-fiber interactions<sup>16</sup>. We study the drying and reswelling of bacterial cellulose microcapsules on different substrates to control capsules' dried shape, size, and porosity. The kinetics of drying and rehydration, as well as the forces involved in shape change during these processes, is quantified using imaging measurements of the capsules.

## 4.2 Methods and Materials

**Preparation of bacterial cellulose microcapsule:** The bacterial cellulose microcapsule preparation method follows the work of Song et al.<sup>14</sup>. First, *Acetobactor xylinum* (Nourishme Organics, Australia) was purified by gradient centrifugation and dispersed in a fermentation culture containing coconut water (Cocobella, Indonesia), 10 wt% of sugar, and 1 wt% of ammonium phosphate (AJAX chemicals, Australia). Then, a gelled oil suspension medium was prepared by mixing 2.5 g of hydrogenated castor oil (Acme Hardesty) into 100 mL of canola oil (Coles, Australia) at 90 °C for 10 min. Upon cooling, the system develops a yield stress that can suspend water droplets of bacterial culture. Cellulose microcapsules were synthesized when *Acetobactor xylinum* produced nanocellulose fibers at the liquid-liquid interface of their enclosing emulsion droplets, a bio-interfacial templating process, in the gelled oil. Within two weeks, bacterial made an entangled mesh cellulose shell with a total thickness of 20 – 50  $\mu\text{m}$  and pore size of 0.5  $\mu\text{m}$  in each droplet. Cellulose microcapsules are separated by heating the gelled oil emulsion to 90 °C for 2 h and soaking in 2 wt% NaOH (Chem-Supply Pty Ltd, Australia) at room temperature overnight to kill the bacteria. The killed bacteria and other impurities were washed away by washing the cellulose microcapsules with MQ water at least three times. When the washed bacterial cellulose microcapsules needed to be surface treated for reversible drying and rehydration, they were dispersed in different concentrations of aqueous carboxymethyl cellulose (with average Mw ~ 250,000 g/mol and degree of substitution 0.7, Sigma Aldrich, Australia) solution to obtain final polymer concentrations of 0.25, 0.5, or 1 wt%.

### 4.2.1 Sample imaging and analysis

**Scanning electron microscopy:** Scanning electron microscopy, SEM, was used to study the shape, size, and porosity of cellulose microcapsules after drying. An FEI Nova Nano SEM 450 FE-SEM with an accelerating voltage of 5.0 kV was used for all SEM imaging. Before SEM imaging, samples were snap-frozen in liquid nitrogen, dehydrated overnight in a freeze drier, and coated with a 30 nm thick platinum layer using a Leica ACE600 sputter coater.

**Microscopy:** Low-magnification optical microscopy images were acquired via stereoscope (WILD M3C, Leica, Germany) with 25× and 40× objective to enable individual capsule analysis. Motic Images Plus v2.0 software was used to capture digital images with a 1 s time interval during drying and swelling. ImageJ software was utilized to measure the microcapsule size with time<sup>17</sup>. All measurement was repeated for at least five capsules. The time-dependent drying and swelling data are fitted to a power-law function using the curve fitting tool in MATLAB<sup>18</sup>.

## 4.3 Results and discussion

The low solid density of the bacterial cellulose capsules ( $0.01 \text{ g/cm}^3$ ), flexibility, and porous mesh structure<sup>14</sup> motivated us to explore production of two- and three-dimensional cellulose particles using a drying process. Figure 4.2(a) shows an optical image of multiple cellulose microcapsules stained with Congo red in an aqueous solution with sizes ranging from 100 to 800  $\mu\text{m}$ . Here, we use a different method of drying cellulose microcapsules to investigate the drying impact on the cellulose mesh and bulk structure.

Figure 4.1 (a and b) show a time-lapse, side-view image of the unmodified cellulose capsules during air drying at room temperature on a flat glass slide (a) and

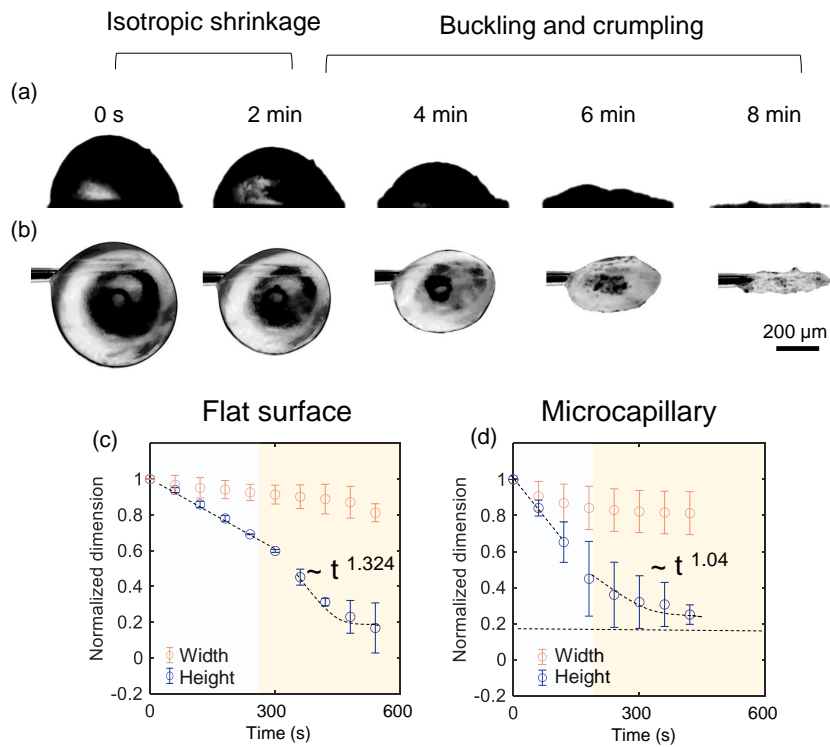


**Figure 4.1:** Time sequence of a cellulose microcapsule air drying on (a) a flat glass surface and (b) a glass capillary tip with a minimum diameter of  $100\ \mu\text{m}$ . The air-drying process leads to a dramatic change in the capsule size, depending on the capsule contact status with a substrate, with the shape of substrate determining the final shape and size of the cellulose particles. (c) A plot of change in capsule dimensions over time for ten capsules (d) a capillary tip.

pulled capillary tip with a maximum diameter of 100  $\mu\text{m}$  (b)). The right-hand image in each row shows the final size of the cellulose microcapsule after 8 min of air-drying. The drying process drives remarkable shrinkage in the microcapsule height compared with its width when dried on the flat glass substrate due to water meniscus pinning of the microcapsule to the substrate. The pinning of a droplet to a substrate has been seen and reported before in the interfacial assembly of particles in studies of the coffee-ring effect<sup>19-21</sup>. The millimeter diameter capsule shrinks to a flat disk with thickness of 200 nm,  $\sim 100\%$  strain, and a width similar to the original capsule dimension. Here the capillary forces during drying act to pull the capsule down and compress it flat onto the flat substrate as a result of the circular contact line. However, drying the capsule on a glass capillary tip leads to collapsing the capsule all around the surface of the capillary. Figures 4.2 (b and c) show optical images of dried cellulose microcapsules on a flat solid substrate and a microcapillary tip, respectively, indicating extreme volume transition after air drying. Similar to drying on a flat substrate, the water meniscus pins the cellulose microcapsule to the glass capillary, causing the capsule to shrink and buckle around the capillary. This results in a 2D deformation that can be observed, and the capillary tip becomes wrapped in the cellulose microcapsule once the capsule is completely dried.

Figure 4.1 (c) quantifies the dynamic changes of capsule height and width, normalized with their initial value. A linear decrease with a rate of  $0.1\text{ s}^{-1}$  in the capsule size is observed in the early stage of water evaporation and a nonlinear drop in the capsule height over time with a rate of  $1.3\text{ s}^{-1}$ . In contrast, a minor, less than 20% with a rate of  $1\text{ s}^{-1}$ , change in width was also observed, in agreement with the previous research on cellulose fiber drying dynamics<sup>22</sup>.

The constant and linear deformation of cellulose microcapsules is due to bulk water evaporation, reducing the cellulose microcapsule size and porosity due to

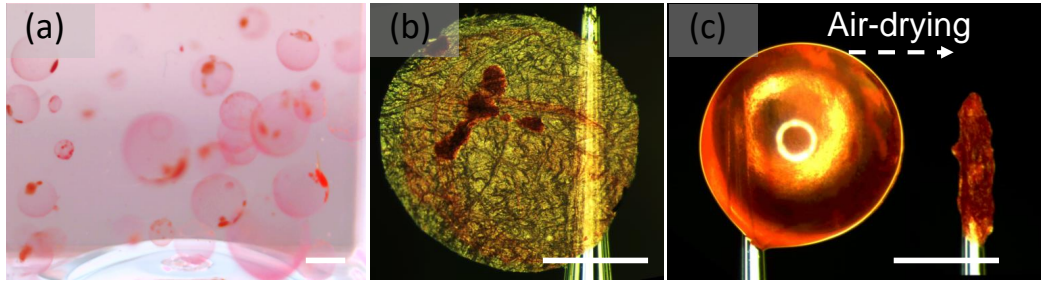


**Figure 4.2:** (a) Cellulose microcapsule dispersion in water. (b) Ultrathin cellulose disk production after drying a cellulose microcapsule on a nonadhesive flat surface. (c) Air-drying a cellulose microcapsule on a tapered cylindrical capillary leads to collapse of the capsule onto the capillary during the drying process, scale bar is 500  $\mu\text{m}$ .

capillary forces. When the cellulose fibers are close to each other or partially exposed, the second drying stage starts. In the second stage, hydrogen-bonded water evaporation takes place over the cellulose surface. Here the capillary tension reaches its maximum value, and vapor diffusion is the main driving force for continued water evaporation<sup>22</sup>.

A high level of capsule deformation and strain occurs due to a high stress based on the capsule density and geometry. For instance, pollen with an average diameter of 40  $\mu\text{m}$ , wall thickness of 1.4  $\mu\text{m}$ , and elastic modulus of 1.3 GPa only deforms with a strain of  $\sim 40\%$  during the dehydration process<sup>23,24</sup>. Polymer-based microcapsules with diameter and shell thickness of 60  $\mu\text{m}$  and 400 nm, respectively can withstand  $\sim 3$  MPa stress and deform less than 50% under stress, indicating the capsule geometry and mechanical properties inhibit capsule deformation and shape transition<sup>25</sup>. Here, the microcapsule shell has a low solid density mesh structure made from cellulose nanofibers, allowing the capsule to shrink and deform from  $\sim 25$   $\mu\text{m}$  to less than 100 nm during the drying process. Hence, this provides an extremely high strain (over 99.9%) compared with previously reported microcapsules<sup>6,26–28</sup>.

The capsules here have been estimated to have a low compressive elastic modulus on the order of 100 Pa<sup>14</sup>.

During drying, the capillary pressure of the water meniscus is the dominant driving force for microcapsule deformation, pulling cellulose fibers tightly together and compressing the microcapsule structure. Liquid evaporation occurs in two stages. The evaporation starts with bulk water removal, and the rate depends on the microcapsule size (or liquid volume as the capsule is filled with water). As evaporation occurs, the capillary force induces water flow through the porous structure and compresses it. The pore size is reduced till fibers are extremely close to one other, allowing van der Waals forces to strongly bind the fibers together<sup>29,30</sup>. The maximum capillary force ( $P_C$ ) on the capsule during drying occurs when the meniscus radius is small enough to fit into the pores. Assuming liquid in cylindrical pores, we can estimate:<sup>31</sup>

$$P_C = \frac{\gamma_{lv} \cos \theta S \rho_b}{1 - \frac{\rho_b}{\rho_l}} \quad (4.1)$$

where  $\rho_b$ ,  $\rho_l$ ,  $\gamma_{lv}$ ,  $\theta$ , and  $S$  are the bulk density of the porous film, the density of the solid fibers, liquid-vapor surface tension, liquid-fiber contact angle, and the specific surface area of the fiber network. From literature that  $\rho_b$  and  $\rho_l$  are 0.01 and 1.5 g/cm<sup>3</sup>, respectively for the cellulose mesh and an individual cellulose nanofiber (with diameter of 40 nm)<sup>14,32,33</sup>, and  $\gamma$  is 72 mN/m for water at 25 °C<sup>34</sup>. Bacterial cellulose specific surface area (surface area of capsule/ mass of capsule) is calculated for 500 μm capsule with porosity of 0.6 and the weight of 0.2 μg<sup>35</sup> as 16.7 m<sup>2</sup>/g. Therefore, the maximum capillary pressure during drying is estimated to be 7.7 kPa, enabling extreme deformation of the cellulose microcapsule

Capsule deformation and bending occurs at multiple length scales. The above treatment deals with deformation on the length scale of the capsule. At the nanoscale,

individual fibers bend and deform as water moves through the cellulose mesh structure, sealing capsule pores in the early stage of drying, depending on the fiber bending stiffness. The bending stiffness of an individual cellulose fiber can be calculated by the following equation<sup>36,37</sup>:

$$\kappa = \frac{Eh^3}{12(1-\nu^2)} \quad (4.2)$$

Where  $\kappa$ ,  $E$ , and  $\nu$  are a bending stiffness, the Young's modulus and Poisson's ratio of the material, respectively. For the bacterial cellulose fiber with diameter of (40 nm), a Poisson ratio of 0.54<sup>38</sup> and a cellulose fiber elastic modulus of  $\sim 17$  GPa<sup>39</sup>, the bending stiffness is 60 Pa,  $\sim 128$  times less than capillary pressure during drying.

Water removal and heat dissipation during cellulose fiber drying cause pore closure and a decrease in surface area, leading to fiber network shrinkage and increased inter-cellulose hydrogen bonding<sup>40</sup>. This buckles the microcapsule from several hundreds of microns in diameter to less than 50 (volume change by a factor of 1000). Similarly, reswelling of the dried cellulose nanostructures releases the stored elastic energy as the fiber bundles reform a sparse cellulose fibrous network<sup>41-43</sup>.

Sealed soft microcapsule can withstand moderate amounts of strain without permanent deformation or material yielding<sup>14</sup>. Further increase in the stress can bend, buckle, and permanently deform the microcapsule. Here, in order to determine the capsule deformation in the second stage of drying, we used the theoretical prediction of the critical buckling pressure for cellulose capsule with radius and shell thickness of 250 and 25  $\mu\text{m}$  during air drying process:

$$P_c = \frac{2E}{\sqrt{3(1-\nu)^2}} \left(\frac{R}{h}\right)^{-2} \quad (4.3)$$

where  $E$  and  $\nu$  are the Young's modulus of cellulose microcapsule and Poisson's ratio of the material, respectively. The critical buckling pressure is calculated as  $P_c = 1.4 \text{ Pa}$ , so capsule buckling begins when a higher pressure is applied to the capsule.

In the case of thin shell capsule, bending deformation is energetically favourable as stretching requires higher amount of energy. Capsule bending can be in plane or out-of-plane deformation or both, the Foppl von Karman number  $\gamma_{Foppl}$  (the ratio of bending to stretching energy) can be used to characterize the order of magnitude of the ratio between in plane and out-of-plane deformation energies, as the key parameter to understand the elastic shell deformation<sup>44</sup>. High value of the Foppl von Karman number indicates large bending of shell and its low value represents high stretching deformation, however, stretching is more energetically costly<sup>45</sup>.

$$\gamma_{Foppl} = 12(1 - \nu^2) \left( \frac{R}{h} \right)^{-2} \quad (4.4)$$

The  $\gamma_{Foppl}$  of our cellulose capsule with the above mentioned radius, shell thickness, and Poisson ratio is calculated as 850, indicating more in-plane deformation versus out-of-plane deformation<sup>46,47</sup>.

Water evaporation causes the fibers to bend, and the pore size reduces till the capsule is sealed and deformed. Self-sealing of this type also occurs when the pollen grains compress and fold during drying to protect and carry plant DNA. Distinct from the above results for substrate-influenced drying of the cellulose capsules, pollen grains typically dry via isotropic shrinkage during dehydration<sup>23</sup>. We want to evaluate the effect of similar drying-induced isotropic shrinkage on the capsules synthesized here, so pinning to the substrate by a water meniscus must be avoided. Spray-drying is a common method of synthesizing dry particles via isotropic drying of droplets<sup>48,49</sup>, as droplets are sprayed and exposed to hot air, but study of individ-

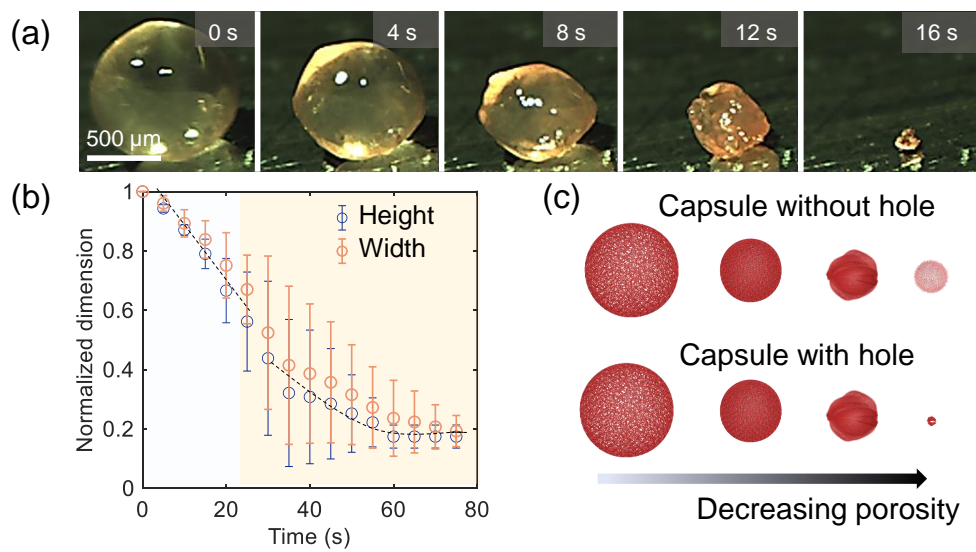


**Figure 4.3:** Isotropic compression of cellulose microcapsule using Leidenfrost phenomenon. (a) The microcapsules were shrunk 1000 times of their volume at 180 C. The drying and shrinkage kinetics of five microcapsules are shown in (b), where the capsule dwindle in all dimensions to make 1000 times smaller cellulose particles. (c) Schematic of the possible fate of the cellulose microcapsule after drying by Leidenfrost phenomenon, where cellulose capsule has a hole in the structure the capsule shrink to several micron-scale in size, otherwise sealing the pores lead capsule explosion.

ual droplet drying is difficult under these conditions. Previous work showed that the Leidenfrost phenomenon<sup>50,51</sup> is a viable means of studying the dynamics of single droplet drying<sup>48,52-54</sup> so we use that method here.

Here microcapsules are dried on a layer of water vapor using a heated surface to avoid pinning. A droplet of aqueous cellulose microcapsule dispersion is placed on a preheated hot plate with a temperature of 180 °C. Time-lapse imaging was performed using two frames per second interval during the drying process.

Figure 4.3 (a) shows a time-lapse of the isotropic shrinkage of a single cellulose microcapsule at 180 °C. From direct side-view imaging, we can see millimeter size capsule shrinks by orders of magnitude, finishing as a 100 μm diameter particle in the final frame. The dynamics of capsule contraction were measured for five capsules and plotted in Figure 4.3 (b). The error bar shows the variations in capsule size during the different experiments. Two different behaviors are seen, isotropic shrinkage to a stable capsule and shrinkage followed by overpressure/explosion, in agreement with reported research<sup>48,52-54</sup>. As we can see from Figure 4.3 (a), the microcapsule shrinks till all water evaporates, producing a wrinkled and crumpled particle. In some cases, the cellulose microcapsule explodes, often when the size of microcapsule was more than 1 mm. Such behavior has been seen and reported before<sup>50-52</sup>, producing an audible cracking sound.

Similar to a capsule drying on a solid substrate, we can also see a linear and constant rate of volume transition at the beginning of drying. In this regime a shrinkage rate of 0.02/s is seen due to bulk water evaporation. As this occurs, water migrates from the capsule's core to the surface and the shrinkage is relatively isotropic<sup>22,55</sup> leading to the capsule self-sealing.

In the second drying period, a nonlinear shrinkage is observed with a rate of 0.5/s, when the capsule reaches a critical moisture level and evaporation is limited

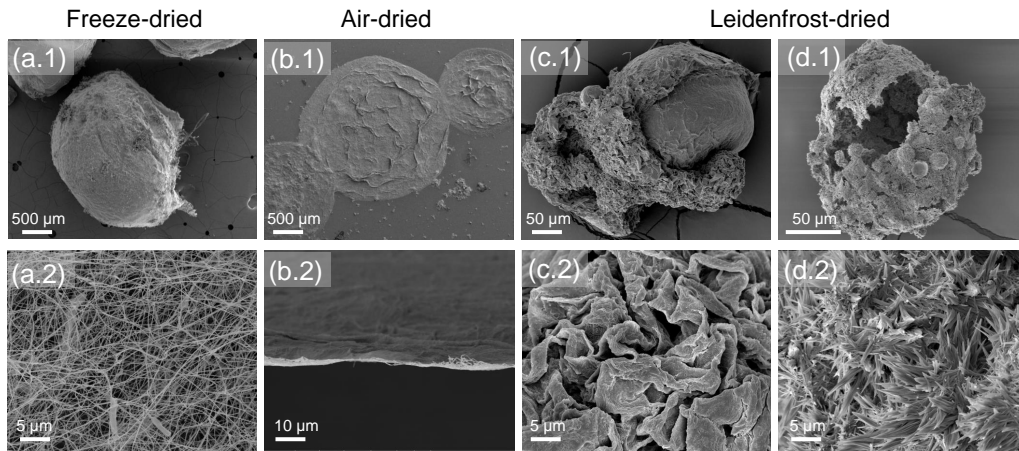


**Figure 4.4:** Scanning electron microscopy (SEM) of cellulose microcapsules after (a) freeze-drying, (b) air-drying, and (c) two types of drying phenomena observed using Leidenfrost processing.

by water movement to the surface via diffusion. These processes lead to the capsule permanently buckling and bending<sup>22,55,56</sup>. This result is in agreement with previous research on cellulose drying and spray drying<sup>22,55,56</sup>. As shown in Figure 4.3c, if a capsule initially has a hole that can be used to relieve pressure during shrinkage the stable production of a small capsule is possible with this method. If pressure can not be relieved via leakage, the capsule will overpressurize and explode to relieve the pressure.

Figure 4.4 shows SEM images of cellulose microcapsules after dehydration using freeze-drying, air-drying on the solid substrate, and the Leidenfrost effect. Freeze-drying is used to dehydrate the capsule while maintaining its structure. The capsule dispersion is instantly frozen in liquid nitrogen and freeze-dried. A millimeter-scale cellulose microcapsule after freeze-drying is shown in Figure 4.4 (a.1 and a.2), with a close-up view indicating the cellulose mesh structure of the capsule. Contrasting this view with that of an air-dried capsule we see the extremely low mass and elastic modulus of millimeter-scale capsules results in severe permanent deformation during air-drying on a solid substrate. The drying forces convert the millimeter size

capsule to a 200 nm thin disk, over a million times smaller than its original size, Figure 4.4 (b.1 and b.2). The SEM view shows the conversion of the open mesh in Figure 4.4a.2 to a flat mat with strongly consolidated fibers, Figure 4.4b.2 This level of shrinkage during drying has also been seen for bulk bacterial cellulose pellicle mesh<sup>48</sup>.

After Leidenfrost drying, the capsule exhibits two different structures. When a capsule is able to continuously shrink, it reduces in size by several orders of magnitude and the form is set by the adaptation of the shell to the stresses it experiences. Figure 4.4 (c.1 and c.2) shows an example of a wrinkled and folded structure of a cellulose microcapsule after drying and crumpled and buckled structures are visible at large and small scales. Buckled structures are also produced by spray drying processes<sup>52,53</sup>.

When the capsule seals during drying, overpressure events can occur and SEM imaging of those capsules shows a large hole in the capsule wall and more rigid alignment of the cellulose fibers, possibly producing greater rigidity that led to the explosion, Figure 4.4 (d.1 and d.2). Boiling water trapped inside the capsule and changing from liquid to vapor caused a pressure increase inside the capsule. For water at 180 °C the steam pressure is 0.8 MPa, 8000 times more than the cellulose microcapsule modulus. This can cause a capsule explosion when the steam is trapped inside the capsule. The explosion usually originates at the bottom of the droplet containing the capsule, where some part of the droplet can sometimes briefly contact the hot plate<sup>51,53</sup>.

In all the above instances, drying of the capsules is an irreversible process because of strong fiber-fiber interactions at small distances. We can, however, dry these capsules in a way that allows them to rehydrate and regain their initial form by mitigating the strong fiber interactions. Several chemical and physical cellulose

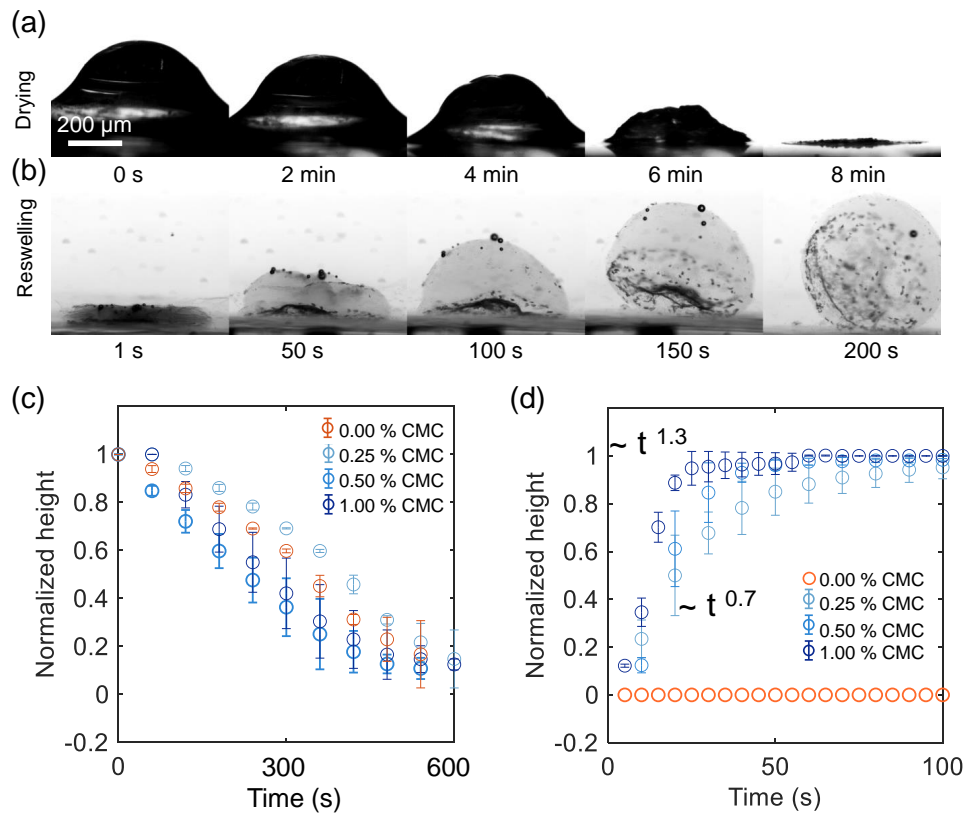


**Figure 4.5:** (a) Cellulose microcapsule-CMC drying process on the glass slide. (b) Swelling on the dried cellulose microcapsule-CMC in water. (c) Kinetics of Cellulose microcapsule-CMC air dehydration at room temperature, and (d) Swelling kinetics of Cellulose microcapsule-CMC in water at room temperature, the microcapsule height is normalized by the microcapsule initial height.

fiber modifications method have been reported to prevent cellulose fiber aggregation, but here we apply the anionic polymer carboxymethyl cellulose (CMC). Three concentrations of CMC are used. Figure 4.5 (a and b) show the time sequence of a cellulose microcapsule, previously contacted with 1 wt% aqueous CMC solution, drying and reversibly re-swelling. The dynamics of the cellulose-CMC capsule drying, Figure 4.5 (c), indicates a linear process with a rate of  $0.15\text{ s}^{-1}$  and a latter nonlinear process with a rate of  $1.7\text{ s}^{-1}$ . The capsule shrinkage rate decreased with increasing CMC concentration, probably as a result of the enhancement of CMC viscosity at higher CMC concentrations. Soft and deformable microcapsules were developed recently using thermally responsive polymers, and they reported up to 90% shape recovery after stretching in high temperature ( $80\text{ }^{\circ}\text{C}$ )<sup>57</sup> and this work is certainly competitive on the same order of response and mass utilization.

## 4.4 Conclusions

In this study, 2D and 3D cellulose particles have been produced using different drying process. The drying permanently deforms the cellulose microcapsule, and here we controlled the drying condition to make desired particles from the microcapsule with millimeter-scale initial size. The capsules' relatively low elastic modulus and mesh structure enables large changes in volume transition during air-drying. The Leidenfrost method of drying particles is used to miniaturize the millimeter scale capsule without a substrate effect by drying the capsule on a vapor layer. Using polymer additives can prevent fibers from irreversibly drying, providing the cellulose microcapsules with strong mechanical response.

---

## References

- [1] L. C. Corrêa-Filho, M. Moldão-Martins, V. D. Alves, *Applied Sciences* **2019**, *9*, 571.
- [2] J. Pessi, H. A. Santos, I. Miroshnyk, D. A. Weitz, S. Mirza *et al.*, *International Journal of Pharmaceutics* **2014**, *472*, 82–87.
- [3] H. Zhao, X. Fei, L. Cao, B. Zhang, X. Liu, *Materials* **2019**, *12*, 393.
- [4] L. Souza, A. Al-Tabbaa, *Construction and Building Materials* **2018**, *184*, 713–722.
- [5] Y. Long, C. Liu, B. Zhao, K. Song, G. Yang, C.-H. Tung, *NPG Asia Materials* **2015**, *7*, e148–e148.
- [6] W. Zhang, A. Abbaspourrad, D. Chen, E. Campbell, H. Zhao, Y. Li, Q. Li, D. A. Weitz, *Advanced Functional Materials* **2017**, *27*, 1700975.
- [7] D. Sun, H. Zhang, X. Zhang, J. Yang, *ACS Applied Materials & Interfaces* **2019**, *11*, 9621–9628.
- [8] D. Sun, Z. Yan, L. Mingzhang, W. Ziming, C. Suping, Y. Jinglei, *Applied Surface Science* **2021**, *546*, 149114.
- [9] M. W. Patchan, L. M. Baird, Y.-R. Rhim, E. D. LaBarre, A. J. Maisano, R. M. Deacon, Z. Xia, J. J. Benkoski, *ACS Applied Materials & Interfaces* **2012**, *4*, 2406–2412.
- [10] B. C. Leopércio, M. Michelon, M. S. Carvalho, *Scientific Reports* **2021**, *11*, 1–12.
- [11] H. I. Benza, W. L. Munyendo, *Int J Pharm Sci Rev Res* **2011**, *10*, 20–4.
- [12] A. Fery, F. Dubreuil, H. Möhwald, *New Journal of Physics* **2004**, *6*, 18.
- [13] J. Cui, M. Björnmalm, K. Liang, C. Xu, J. P. Best, X. Zhang, F. Caruso, *Advanced Materials* **2014**, *26*, 7295–7299.

## References

---

- [14] J. Song, F. Babayekhorasani, P. T. Spicer, *Biomacromolecules* **2019**, *20*, 4437–4446.
- [15] D. E. Ciolacu, *Journal: Polymers and Polymeric Composites: A Reference Series Cellulose-Based Superabsorbent Hydrogels* **2018**, 1–32.
- [16] L. Salmén, J. S. Stevanic, *Cellulose* **2018**, *25*, 6333–6344.
- [17] C. A. Schneider, W. S. Rasband, K. W. Eliceiri, *Nature Methods* **2012**, *9*, 671–675.
- [18] I. The MathWorks, Curve Fitting Toolbox, Natick, Massachusetts, United State, **2020**.
- [19] K. N. Al-Milaji, H. Zhao, *The Journal of Physical Chemistry C* **2019**, *123*, 12029–12041.
- [20] Y. Li, Q. Yang, M. Li, Y. Song, *Scientific Reports* **2016**, *6*, 1–8.
- [21] M. Talantikite, N. Leray, S. Durand, C. Moreau, B. Cathala, *Journal of Colloid and Interface Science* **2021**, *587*, 727–735.
- [22] Y. Peng, D. J. Gardner, Y. Han, *Cellulose* **2012**, *19*, 91–102.
- [23] E. Katifori, S. Alben, E. Cerda, D. R. Nelson, J. Dumais, *Proceedings of the National Academy of Sciences* **2010**, *107*, 7635–7639.
- [24] Z. Qu, J. C. Meredith, *Journal of The Royal Society Interface* **2018**, *15*, 20180533.
- [25] A. Vian, E. Amstad, *Soft Matter* **2019**, *15*, 1290–1296.
- [26] D. Yan, M. Pezzulla, P. M. Reis, *Journal of the Mechanics and Physics of Solids* **2020**, *138*, 103923.
- [27] A. Walter, H. Rehage, H. Leonhard, *Colloids and Surfaces A: Physicochemical and Engineering Aspects* **2001**, *183*, 123–132.
- [28] S.-H. Kim, J.-G. Park, T. M. Choi, V. N. Manoharan, D. A. Weitz, *Nature Communications* **2014**, *5*, 1–8.
- [29] C. C. N. Martins, M. C. Dias, M. C. Mendonça, A. F. S. Durães, L. E. Silva, J. R. Félix, R. A. P. Damásio, G. H. D. Tonoli, *Cellulose* **2021**, *28*, 11519–11531.

- 
- [30] S. Sinquefeld, P. N. Ciesielski, K. Li, D. J. Gardner, S. Ozcan, *ACS Sustainable Chemistry & Engineering* **2020**, *8*, 9601–9615.
- [31] G. W. Scherer, *Journal of the American Ceramic Society* **1990**, *73*, 3–14.
- [32] N. Pircher, S. Veigel, N. Aigner, J.-M. Nedelec, T. Rosenau, F. Liebner, *Carbohydrate Polymers* **2014**, *111*, 505–513.
- [33] R. Dubey, Y.-R. Toh, A.-I. Yeh, *Scientific Reports* **2018**, *8*, 1–11.
- [34] C. Gianino, *Physics Education* **2006**, *41*, 440.
- [35] M. Hosseini, F. Babayekhorasani, Z. Guo, K. Liang, V. Chen, P. T. Spicer, *Journal of Colloid and Interface Science* **2022**, *628*, 435–445.
- [36] L. D. Landau, E. M. Lifšic, E. M. Lifshitz, A. M. Kosevich, L. P. Pitaevskii, *Theory of elasticity: volume 7, Vol. 7*, Elsevier, **1986**.
- [37] C. Py, P. Reverdy, L. Doppler, J. Bico, B. Roman, C. N. Baroud, *Physical Review Letters* **2007**, *98*, 156103.
- [38] K. Nakamura, M. Wada, S. Kuga, T. Okano, *Journal of Polymer Science Part B: Polymer Physics* **2004**, *42*, 1206–1211.
- [39] G. Guhados, W. Wan, J. L. Hutter, *Langmuir* **2005**, *21*, 6642–6646.
- [40] G. A. Smook, *Handbook of pulp & paper terminology: a guide to industrial and technological usage*, **1990**.
- [41] K. Kekäläinen, H. Liimatainen, M. Illikainen, T. C. Maloney, J. Niinimäki, *Cellulose* **2014**, *21*, 1163–1174.
- [42] M. Beaumont, J. König, M. Opietnik, A. Potthast, T. Rosenau, *Cellulose* **2017**, *24*, 1199–1209.
- [43] G. Laivins, A. Scallan, *Products of Papermaking* **1993**, *2*, 1235.
- [44] H.-H. Boltz, J. Kierfeld, *Physical Review E* **2015**, *92*, 033003.
- [45] S. Knoche, J. Kierfeld, *Physical Review E* **2011**, *84*, 046608.

## References

---

- [46] C. Lei, Q. Li, L. Yang, F. Deng, J. Li, Z. Ye, Y. Wang, Z. Zhang, *Soft Matter* **2019**, *15*, 6504–6517.
- [47] S. Knoche, J. Kierfeld, *The European Physical Journal E* **2014**, *37*, 1–21.
- [48] R. de Souza Lima, M.-I. Ré, P. Arlabosse, *Powder Technology* **2020**, *359*, 161–171.
- [49] A. B. D. Nandiyanto, K. Okuyama, *Advanced Powder Technology* **2011**, *22*, 1–19.
- [50] D. Quéré, *Annual Review of Fluid Mechanics* **2013**, *45*, 197–215.
- [51] S. Lyu, V. Mathai, Y. Wang, B. Sobac, P. Colinet, D. Lohse, C. Sun, *Science Advances* **2019**, *5*, eaav8081.
- [52] Y. Sugiyama, R. J. Larsen, J.-W. Kim, D. A. Weitz, *Langmuir* **2006**, *22*, 6024–6030.
- [53] N. Tsapis, E. R. Dufresne, S. S. Sinha, C. S. Riera, J. W. Hutchinson, L. Mahadevan, D. A. Weitz, *Physical Review Letters* **2005**, *94*, 018302.
- [54] A. Yarin, G. Brenn, O. Kastner, C. Tropea, *Physics of Fluids* **2002**, *14*, 2289–2298.
- [55] N. Alhadj, N. J. O'Reilly, H. Cathcart, *Powder Technology* **2021**, *384*, 313–331.
- [56] E. Lintingre, F. Lequeux, L. Talini, N. Tsapis, *Soft Matter* **2016**, *12*, 7435–7444.
- [57] F. Zhang, T. Zhao, D. Ruiz-Molina, Y. Liu, C. Roscini, J. Leng, S. K. Smoukov, *ACS Applied Materials & Interfaces* **2020**, *12*, 47059–47064.

## Chapter 5

### Conclusions and future work

Microcapsules perform a critical function in a number of sectors including drug delivery, environmental remediation, cosmetics, and advanced materials. Recent efforts focus on development of responsive microcapsules to provide enhanced uptake and release. This thesis focused on three distinct approaches to developing multifunctional microcapsules with active deformation and response.

Functional microcapsules are often made from rigid materials with plastic deformation behavior, reducing their ability to exhibit active deformation and response. Here, we used emulsion-templated bacterial cellulose microcapsules as the basis of functional capsules with new properties including significant flexibility, extremely low mass and bulk density (millimeter size capsule has nano-scale mass), biodegradability, high surface area, and porosity. Here we modified the fibrous structure of bacterial cellulose microcapsules using three methods to develop functional and active forms.

The first modification was inspired by microorganisms that can move and deform themselves and squeeze through confined spaces. Bacterial cellulose capsules were coated with metal-organic framework, MOF, particles that contain catalase enzyme to utilize chemical fuel for motion. Coating the individual cellulose fibers with MOF particles also influenced the capsule porosity, changing the pore size from 500 nm to less than 4 nm. We have used two different MOFs, hydrophilic ZIF90 and hydrophobic ZIFL, to achieve two mechanisms of propulsion via enzyme-mediated

production of oxygen gas in aqueous hydrogen peroxide. Oxygen bubbles are expelled from hydrophilic swimmers and cause movement in multiple directions, while hydrophobic swimmers remain attached to growing bubbles and experience vertical, buoyancy-driven motion. As a result, hydrophilic and hydrophobic swimmers move with average velocities of 40 and 4 mm/s, respectively. The aerogel structure of the synthesized motors enables highly efficient motion with less inertia compared to similar active particles made from high-density rigid solids. The flexible, low-density mesh structure of the synthesized motors makes them mechanically responsive, enabling the swimmers to move through significant constrictions, keeping them viable even in confined spaces and environments where solid swimmer particles could not progress.

The second development was multifunctional microcapsules functionalized with the thermal responsive polymer PNIPAM to achieve switchable permeability and thermal-actuated motion. The modification enables responsive size and cargo release as well as subsequent mixing of the local environment. Varying the polymerization rates and reaction time controls the thickness of PNIPAM coating, also varying the microcapsule permeability and elasticity. The PNIPAM-modified capsule is more mechanically robust than the cellulose-only form and can recover its initial shape after dehydration and deformation. Temperature changes trigger mechanical response of the PNIPAM-modified capsule, shrinking it when the temperature is raised to over 32°C and swelling it to its initial shape and size by cooling down to below 32°C. As a result, internal liquid can be expelled and absorbed by the synthesized capsule due to PNIPAM volume transitions. Particle tracking was used to visualize and quantify water absorbing and releasing from the modified capsule, indicating fluid flow around the capsule and mixing the released liquid cargo during multiple cycles of temperature change. By visualizing the flow between two and

---

three modified capsules, we found eddy-like flow around the capsule at multiple cycles of temperature change, indicating the capsules' post-processing benefits after releasing any encapsulated content.

In addition to the chemical modifications of cellulose microcapsules, shape-changing during extreme drying has been investigated after the physical modifications of cellulose fibers. Here, milli- or micro size cellulose microcapsules deformed to nano-scale thin two-dimensional disks during drying, resulting in permanent deformation of the pristine cellulose capsule by capillary pressure and van der Waals interactions. The final shape of dry cellulose particles can be changed to three-dimensional particles using a Leidenfrost drying method. During the drying process, cellulose microcapsules experience orders of magnitude change in volume. We found that the dried cellulose microcapsules can re-swell and recover to their initial millimeter-scale size after soaking the pristine cellulose microcapsules in carboxymethyl cellulose solution, allowing complete reversibility of the drying-swelling transition within less than 10 seconds.

Regarding the unique mesh structure and functionality of cellulose microcapsules, there are considerable recommendations for future research in this area. In this study, we employed three methods of modifying cellulose fibers to create a multifunctional microcapsule, indicating the potential for further and selective modifications of bacterial cellulose microcapsules for more specific applications. For example, developing light-responsive or magnetic-responsive microcapsules or creating patchy capsules with asymmetric deformation and response. While we have developed multifunctional microcapsules in this research, the application of these capsules in different research fields needs to be investigated, especially as a microplastic collector from the ocean.



## Appendix A

### Appendix

#### A.1 Supplementary information for chapter 2

##### X-ray diffraction:

Powder X-ray diffraction (PXRD) patterns of MOF-coated and enzyme-loaded cellulose microcapsules were collected using an Empyrean Thin-Film XRD Xpert Materials Research diffractometer (MRD). Structural studies of the crystalline MOFs formed on the capsules showed identical diffraction patterns for both ZIFL and ZIF90. Figure A1 shows characteristic diffraction peaks of ZIF90 at  $2\theta = 10$  to  $30^\circ$ , which confirms successful preparation<sup>1</sup>. In addition, no significant difference was observed between the crystal structure and crystallinity of enzyme-loaded and native MOFs crystals, suggesting that the ZIFL crystal structure was well maintained in enzyme-loaded particles, Figure A1b. For the ZIFL/CAT *in situ* composite, the distinct peaks identified are at positions  $2\theta$  of  $7.3^\circ$ ,  $10.3^\circ$ ,  $12.7^\circ$ , and  $18.02^\circ$  corresponding to 110, 200, 211, and 222 orientations, respectively<sup>2,3</sup>. These are in good agreement with simulated ZIFL patterns<sup>4</sup>.

Figure A2 shows measured motor trajectories in different concentrations of aqueous hydrogen peroxide. Each trajectory is colored with its velocity and orientation.

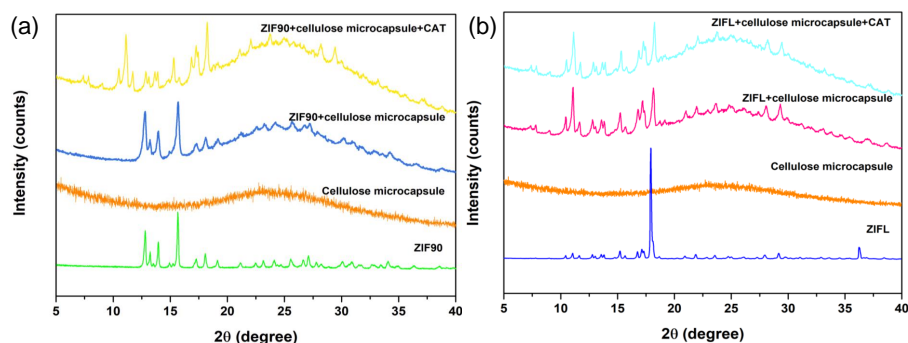


**Figure A1:** XRD pattern of the (a) hydrophilic (ZIF90) and (b) hydrophobic (ZIFL) MOF coated cellulose motors containing catalase (CAT).

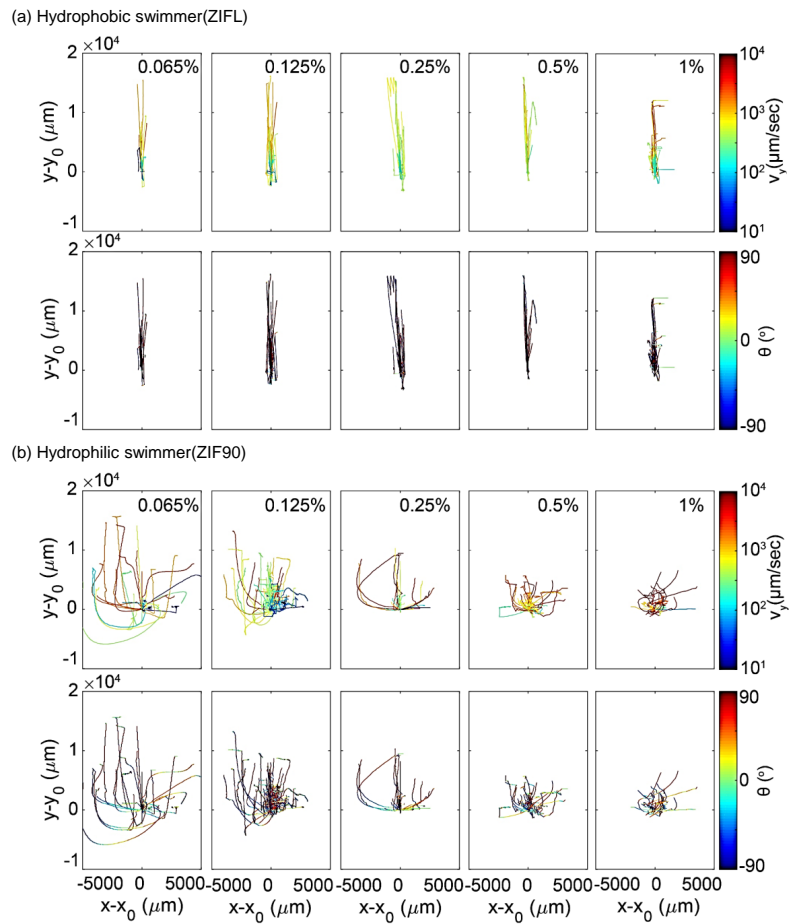


**Figure A2:** The figure shows the tracking of more than 10 hydrophobic (a) and hydrophilic (b) motors in different concentrations of hydrogen peroxide indicates. The average velocity of both hydrophilic and hydrophobic motors is calculated and has been plotted.

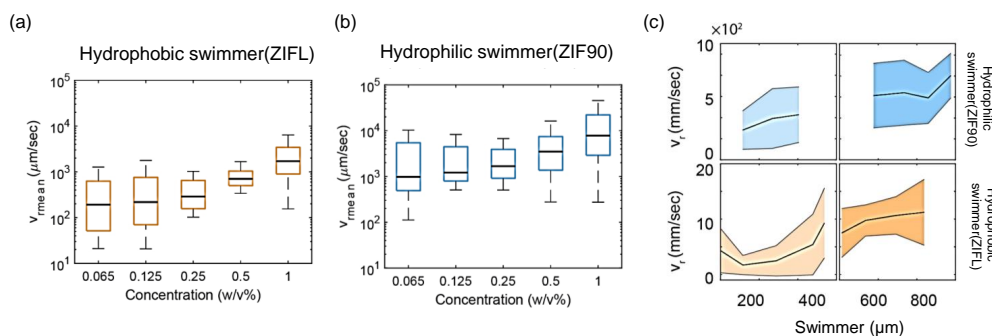


**Figure A3:** The figure shows the average velocity of more than 10 hydrophobic (a) and hydrophilic (b) motors in different concentrations of hydrogen peroxide. (c) The average velocity of the motors as a function of their size.

The trajectories of hydrophobic motors exhibit a more vertical  $90^\circ$  motion with an average velocity of 4 mm/s, Figure A2a. However, the hydrophilic motor trajectories exhibit more complex motion with an orientation ranging from  $0^\circ$  to  $90^\circ$  and an average velocity of 40 mm/s, Figure A2b. Increasing the concentration of hydrogen peroxide increases the velocity of motors due to higher oxygen bubble production.

Figure A3 shows the average velocity of hydrophilic and hydrophobic motors in different concentrations of hydrogen peroxide. Increasing the hydrogen peroxide enhances the oxygen bubble production, consequently increasing the average velocity of both hydrophilic and hydrophobic motors. Figure A3c shows the average velocity of the motors versus their size, indicating that increasing the motor size enhances the average velocity of motors in both hydrophilic and hydrophobic swimmers due to a higher amount of attached enzyme causing more oxygen bubble production. The color bar indicates the variation of average velocity for each motor size.

Figure A4 shows the elastic modulus measurements of the hydrophilic and hydrophobic motors while passing through the pulled capillary. In this method, stress is applied in multiple steps, and the hydrostatic and radial pressure from the glass wall deforms the motors<sup>5</sup>. Motor deformation during linear and nonlinear deformation was captured and quantified using image analysis. This experiment has been repeated for at least 5 motors. The hydrophilic motors exhibit more deformation under stress than the hydrophobic ones. Estimates of the elastic modulus values of hydrophilic and hydrophobic motors were obtained from the slope of a

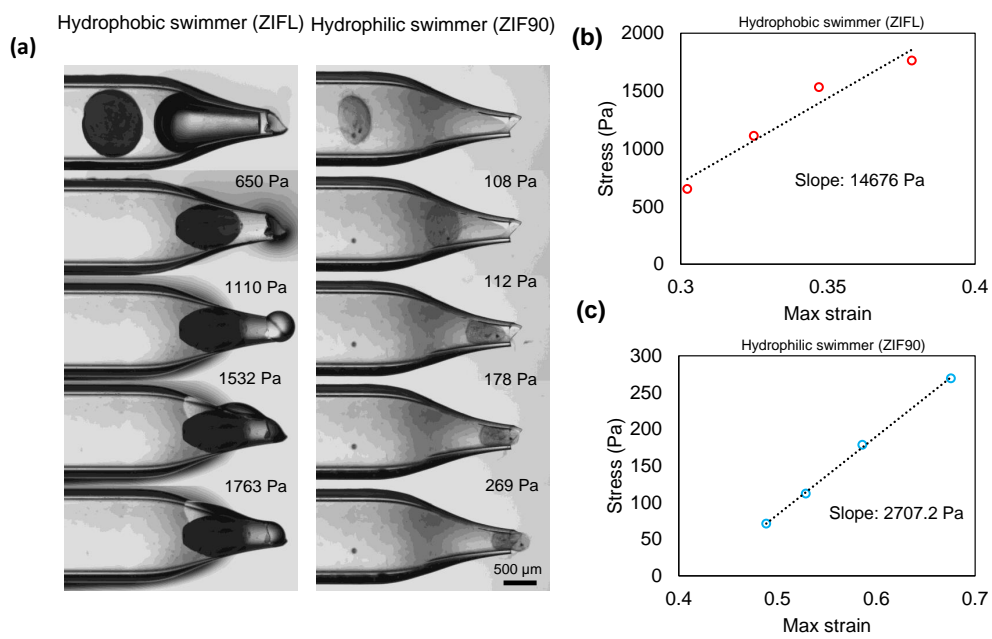


**Figure A4:** Hydrophilic and hydrophobic motors were deformed while passing through a tapered capillary. (a and b) A montage of images shows the motor deformation when passing the constriction. (c and d) The stress and strain of motors using the pressure-induced deformation when forced through a tapered glass capillary.

stress versus strain plot. There is a large variation of elastic modulus due to the variety of cellulose microcapsules<sup>5</sup> for both hydrophilic and hydrophobic motors, so these values are only a weak estimate of the magnitude of the moduli.

## References

- [1] W. Li, S. Chen, Y. Yang, Y. Song, C. Ma, X. Qiao, C. Hong, *Microchimica Acta* **2021**, *188*, 1–9.
- [2] M. Mohammad, A. Razmjou, K. Liang, M. Asadnia, V. Chen, *ACS Applied Materials & Interfaces* **2018**, *11*, 1807–1820.
- [3] H. Yuan, Y. Wu, X. Pan, L. Gao, G. Xiao, *Catalysis Letters* **2020**, *150*, 3561–3571.
- [4] Z. Guo, T. Wang, A. Rawal, J. Hou, Z. Cao, H. Zhang, J. Xu, Z. Gu, V. Chen, K. Liang, *Materials Today* **2019**, *28*, 10–16.
- [5] J. Song, F. Babayekhorasani, P. T. Spicer, *Biomacromolecules* **2019**, *20*, 4437–4446.